NOTICE

The quality of this microform is heavily dependent upon the quality of the original thesis submitted for microfilming. Every effort has been made to ensure the highest quality of reproduction possible.

If pages are missing, contact the university which granted the degree.

Some pages may have indistinct print especially if the original pages were typed with a poor typewriter ribbon or if the university sent us an inferior photocopy.

Reproduction in full or in part of this microform is governed by the Canadian Copyright Act, R.S.C. 1970, c. C-30, and subsequent amendments.

AVIS

La qualité de cette microforme dépend grandement de la qualité de la thèse soumise au microfilmage. Nous avons tout fait pour assurer une qualité supérieure de reproduction.

S'il manque des pages, veuillez communiquer avec l'université qui a conféré le grade.

La qualité d'impression de certaines pages peut laisser à désirer, surtout si les pages originales ont été dactylographiées à l'aide d'un ruban usé ou si l'université nous a fait parvenir une photocopie de qualité inférieure.

La reproduction, même partielle, de cette microforme est soumise à la Loi canadienne sur le droit d'auteur, SRC 1970, c. C-30, et ses amendements subséquents.

Canada

Computer Modeling of Electromagnetic Interference, Radiation, and Cross-Talk in Electronic Systems

Mohammed Saleh Hussein Tharf

Dissertation Submitted to the
School of Graduate Studies and Research
in partial fulfillment of the requirements for the degree of
DOCTOR OF PHILOSOPHY

Ottawa-Carleton Institute for Electrical Engineering
Department of Electrical Engineering
Faculty of Engineering
University of Ottawa

July 7, 1993

ISBN 0-315-89716-3

UNIVERSITÉ D'OTTAWA
UNIVERSITY OF OTTAWA

I hereby declare that I am the sole author of this document. I authorize the University of Ottawa to lend this document to other institutions for the purpose of scholarly research.

Mohammed S. Tharf

I further authorize the University of Ottawa to reproduce this document by photocopying or by any other means, in total or in part, at the request of other institutions or individuals for the purpose of scholarly research.

Mohammed S. Tharf

Acknowledgements

The author would like to express his sincere gratitude to Professor George Costache (Chairman, Department of Electrical Engineering, University of Ottawa), academic supervisor, for his continuous understanding and cooperation during the period of study and preparation of the thesis manuscript. The manuscript was carefully reviewed by the examiners to whom the author owes considerable debt, namely, Professor David Gibbons (Assistant Dean, Faculty of Engineering, University of Ottawa), Dr. Satish Kashyap (Division of Electronics, Department of National Defense), Professor Tapan K. Sarkar (Department of Electrical Engineering, Syracuse University, United States of America), and Professor Michel Nakhla (Department of Electronics, Carleton University). Further, the author is grateful to many of his colleagues for the invaluable discussions during the Ph.D. program.

Acknowledgement is made of the financial aid of both Jordan University of Science & Technology and Canadian International Development Agency.

Last but not the least, the author would like to mention his parents, sisters, and brothers for their encouragement and care throughout all the stages of his study. Also the persons whom he had in mind at all times, his beautiful daughter Hajirah, and his lovely sons Yazan and Nizar.

Abstract

A recently proposed edge-based finite element method (FEM) solution, for eigenvalue problems, is customized for deterministic bounded applications. The solution is then combined with asymptotic expansions of the fields scattered from an inhomogeneous object due to plane wave illumination. Moreover, the combination is modified to solve for radiation problems. The validity and accuracy of the formulations are demonstrated by comparison to other published data. Variety of applications are considered including the computation of the un-intentional radiation and crosstalk interference levels on printed circuit boards, penetration into shielding enclosures, and radar cross-section. The solution described is two-dimensional and the system matrix obtained is sparse (or banded) and symmetric. Further, the solution can be obtained directly without the need for matrix inversion.

In addition, a three-dimensional hybrid numerical method is proposed. The method combines the edge-based FEM with the analytical solutions of arbitrary-large cavity with aperture. This hybrid method has the advantages of producing sparse matrix and substantially reducing the number of unknowns. Thus computer storage and processing time demands are reduced. The hybrid results are in agreement with the edge-based FEM solutions. Measurements also were performed and the results match well with the hybrid solution. The applications considered involve one of the problems that concern the EMI/C society, namely, the crosstalk on dielectric boards.

Since the principal contribution of this dissertation is the development of hybrid numerical methods, one chapter is devoted to review the hybrid numerical methods.

Contributions

This thesis contains the contributions listed below

- Combining, recently developed two-dimensional, edge-based finite element method with an asymptotic solution. Specifically, the edge elements method is used inside a truncating boundary that terminates the finite elements mesh. The solution of the infinite space exterior to the truncating boundary is expressed in terms of asymptotic expansions with unknown amplitudes. The edge element method solution and the asymptotic expansions are combined through the continuity conditions across the truncating boundary. This combination is intended to model the interference due to an electromagnetic wave incident on an electronic device. The following applications are considered:

  1. Infinite plane dielectric slab
  2. Rectangular shielding enclosure with a long slot
  3. Homogeneous dielectric cylinder
  4. Inhomogeneous dielectric cylinder
  5. Circular cylindrical shell
  6. Semi-circular cylindrical shell

  The combination is successfully applied at the resonance frequencies. Further, to demonstrate the validity of the formulation, the numerical computed results are compared to published data, and the agreement is fairly good.

- The combination described is then modified to solve for radiation problems. The modified formulation is used to compute the un-intentional electromagnetic radiation and crosstalk interference for different printed circuit boards configurations.

- In addition, the two-dimensional edge-based finite element method originally proposed for eigenvalue problems, is customized to deterministic bounded problems. The crosstalk levels in packed printed circuit boards are computed. The computations are compared to analytical solutions when the tracks have very-small cross-sectional dimensions compared to the circuit package which is the practical situation. The two solutions are almost indistinguishable.

- Three-dimensional hybrid numerical method is proposed. The method is useful for structures containing arbitrary-large housing with aperture. A potential domain of application of this method is packed printed circuit boards and very large scale integrated circuits. The circuit package is represented by a metal shield most of it is empty except for the inhomogeneous filling (the substrate together with the lands and sources). Only the inhomogeneity need to be discretized if the hybrid method is used. The remaining empty part is represented by modal expansions with unknown amplitudes. This significantly reduces the number of unknowns. The matrix produced is sparse and there is no need for any matrix inversion. The hybrid solutions are compared to other published data, the pure edge-based finite element method, and analytical solutions. An experiment was made. The comparisons between the hybrid and other solutions and the experimental results demonstrate the usefulness and validity of the method.

Glossary

2D	Two Dimensional
3D	Three Dimensional
*	Indicates complex conjugate
$\hat{}$	Denotes unit vector
$\vec{}$	Indicates vector quantity
ϵ_r	Relative permittivity
μ_r	Relative permeability
σ	conductivity ($\mho$/m)
ω	Angular frequency (rad/s)
ABC	Absorbing Boundary Condition
CPU	Central Processing Unit

$\vec{E}$	Electric field vector
EFIE	Electric Field Integral Equation
EM	Electro-Magnetic
EMI/C	Electro-Magnetic Interference/Compatibility
FDM	Finite-Difference Method
FEM	Finite-Element Method
GMT	Generalized Multipole Technique
GTD	Geometrical Theory of Diffraction
$\vec{H}$	Magnetic field vector
HNM	Hybrid Numerical-Method
j	$\sqrt{-1}$
k	Wave number (m^{-1})
Lands	Conductors on printed circuit boards
MFIE	Magnetic Field Integral Equation
MoM	Method of Moments

PCB	Printed Circuit Board
RCS	Radar Cross-Section
TE	Transverse Electric
TL	Transmission Line
TM	Transverse Magnetic
VLSI	Very Large Scale Integrated circuit

Contents

List of Figures

Chapter 1

Introduction

1.1 Motivation

Modern systems, such as communication, financial, and military systems, are increasingly depending on electronic controls. These electronic systems are sensitive to electromagnetic (EM) interference because of their low operating levels. Such being the case, EMC (EM Compatibility) engineers are concerned with the protection of these equipment. For efficient and cost-effective protection, there is a need to characterize the interference and evaluate the coupling levels. Computer modeling is important in predicting coupling levels and designing the proper equipment.

The external EM interference with electronic equipment is an open boundary problem that cannot be efficiently solved by any of the pure numerical methods such as the method of moments (MoM), the finite element method (FEM), and the finite difference method (FDM). The reason is that each numerical method is basically designed to solve a particular class of problems; the FEM for bounded inhomogeneous domains, and the MoM for isotropic homogeneous unbounded regions. Also, despite that the intra-system interference may be modeled as a bounded problem for shielded structures, the number of equations needing solution increases dramatically for the three-dimensional (3D) case. The cost for that is degradation in the accuracy of the results and demand-

ing more computer storage which might exceed the capacity of the available computers. To overcome these limitations, a numerical method can be combined with another complementary numerical method, analytical solutions, or asymptotic expansions. Thus, a hybrid numerical method (HNM) involves the combination of different computational techniques applied to different parts of the problem.

The main concern of this thesis is the development of numerical methods for practical applications. This involves extending the realm of application of the existing method, and strengthening the method by the introduction of analytical solutions. Specifically, the finite element method (FEM) is chosen as a platform for its robustness in solving inhomogeneous problems with complex geometries.

An alternative to the classical node-based FEM is the edge-based FEM. The latter relaxes the constraint of inter-element continuity which provides a natural fit for the underlying variational principle. Many papers reported that the edge-based FEM solution is free of the undesired spurious modes. In addition, it can model sharp points and edges without any need for special singular trial functions. Based on these facts, the edge-based FEM is considered in this thesis.

As hybrid numerical methods are developed in the thesis, it starts with an overview of the existing hybrid numerical methods in electromagnetics. An extensive bibliography is included for further investigation.

1.2 State of the Art of Edge-Based Finite-Element Methods

The construction of finite-element methods based on vector-valued edge-elements, called hybrid elements, was suggested by Raviart and Thomas [1] for two-dimensional fluid flow. Characteristic of these elements is that the degrees of freedom are associated with each side of the element. Subsequently, Nedelec [2] provided the extension of

these elements to three-dimensions. Bossavit and Verite [3]-[4] used the edge element on tetrahedron proposed by Nedelec [2] to solve eddy current problems in terms of the magnetic field. Hano [5] employed a two-dimensional rectangular edge element for solving inhomogeneous waveguiding problems.

The hexahedral edge element was proposed by Welij [6]. Also, Mur and Hoop [7] utilized a tetrahedral edge element with two degrees of freedom for each edge. Barton and Cendes [8] employed the 3D edge elements on tetrahedron to solve magnetostatic field problems in terms of the vector potential. In 1988, Bossavit [9] found that Whitney forms (refer to Chapter 5) are good choice for linear edge-element on a tetrahedron.

A higher order hexahedral edge element was proposed by Crowley [10]. Recently, Lee [11] has proposed a tetrahedron with twenty degrees of freedom. More recently, Webb and Forghani [12] have described a hierarchal set of high-order tetrahedral elements. Wang and Ida [13] have presented a systematic method of construction of curvilinear and higher-order tetrahedral and hexahedral edge-elements.

1.3 Organization of the Thesis

In Chapter 2, the various hybrid numerical methods in EM are classified, according to the computational techniques combined. Each hybrid method is then described, analyzed, and evaluated. Next, a two dimensional numerical solution to the external interference problem is proposed in Chapter 3. This solution combines the edge-based FEM applied to the inhomogeneous object with asymptotic expansions describing the scattered EM fields in the surrounding medium. Since radiation is an inverse scattering problem, this solution is modified and applied to the problems of crosstalk and unintentional radiation from printed circuit boards in Chapter 4. Chapter 5 presents a three dimensional hybrid numerical method for inhomogeneous applications involving arbitrary-large housing. This hybrid method combines the edge-based FEM with analytical solutions of a cavity with aperture.

Chapter 2

Overview of Hybrid Numerical Methods in Electromagnetism

In order to improve a numerical method, it can be combined with an analytical solution, an asymptotic expansion, or another numerical method. Also, ideas from other computational techniques can be adapted and introduced into a numerical method to overcome certain limitations. The numerical method after these modifications is called hybrid numerical method. In general, a hybrid numerical method (HNM) involves the combination of different computational techniques applied to different parts of the problem. From this definition, it is clear that large number of combinations are possible. Further, each combination can be formulated in different ways, i.e., different approaches to the same combination. Each approach has advantages and limitations. However, to the author's knowledge, no attempt was made to classify these hybrid methods. An attempt is made here to classify the various HNM according to the combination used. Also a bibliography is appended including the key papers associated with each hybrid combination, in addition to other papers for further investigation.

The HNM available in electromagnetics are classified according to the combination used. In addition, each combination is analysed and evaluated. Furthermore, the domain of application of each hybrid method is identified. This is expected to help in choosing the proper method for a given application.

The various HNM are classified as follows:-

1. Numerical method combined with asymptotic expansion:- MoM with GTD (geometrical theory of diffraction), and MoM with Quasi-static techniques.

2. Numerical method combined with analytical solution:- MoM with Green's function.

3. Combinations of different numerical methods:- MoM with finite method (FEM or FDM), The finite element-boundary integral method, FEM with GMT (generalized multipole technique).

4. Combining different formulations:- EFIE (electric field integral equation) with MFIE (magnetic field integral equation) formulations of the MoM, and MoM with Volume polarization currents.

In this Chapter, Section 2.1 introduces two combinations: MoM with GTD, and MoM with Quasi-static techniques. In Section 2.2, the incorporation of an analytical solution into a numerical technique is illustrated. Also, the combination of two numerical methods is introduced in Section 2.3. Next, Section 2.4 illustrates the combination of different formulations into a numerical method. Finally, the Chapter concludes with Section 2.5.

2.1 Numerical Method Combined with Asymptotic Expansion

2.1.1 MoM Combined with GTD

The MoM is applicable to structures not large in terms of wavelength. For this reason, it is described as a low-frequency technique. On the other hand, the GTD is a high-frequency asymptotic expansion technique, which can be applied to arbitrarily large

structures. Based on these facts, the combination of these two methods makes it possible to solve problems that could not be treated by any one of them alone.

Two approaches to this combination can be distinguished:

- "The electric field approach" based on modifying the MoM impedance matrix by the diffracted electric field obtained via GTD [14]-[19].
- "The current (or magnetic field) approach" based on incorporating current solutions, obtained from GTD, into the MoM integral [20]-[27].

The electric field approach: The general problem of a radiating element placed on or near a large body is considered. The approach is to modify the impedance matrix of the MoM to account for the existence of the large body. Specifically, the scattered electric field, due to the current on the antenna, may be decomposed into two parts. The first can be accounted for via MoM (e.g. wire antenna in free space where the scattered field can be modelled by the EFIE) . The other, modifies the impedance matrix obtained, and can be computed via GTD (e.g. diffraction from edges). Thus, the assumption is made that the original problem can be modelled by two simpler subproblems (one can be formulated by MoM, and another can be handled by GTD), and superposition is used to augment GTD solution to MoM solution.

The MoM formulation for part of the problem yields the following system of equations [14]:

$$[Z_{mn}][I_n] = [V_m],\ m = 1, 2, ..., N; n = 1, 2, ..., N$$

$[Z_{mn}]$, $[I_n]$ and $[V_m]$ are the generalized impedance, current and voltage matrices, respectively. The elements of $[Z_{mn}]$ and $[V_m]$ are given by:

$$Z_{mn} = \langle W_m, L(J_n) \rangle,\ V_m = \langle W_m, E^i \rangle$$

$\langle\rangle$:the inner product notation, W_m:weighting function, L:linear operator, J_n:the n^{th} basis function, and E^i: the incident field. $L(J_n)$ is interpreted as the electric field from

J_n with I_n equal unity. Using superposition, the contribution of the remainder of the problem (diffracted fields that can be computed by GTD) to the electric field at the observation point m due to the source J_n leads to the new impedance matrix element

$$Z_{mn}^{new} = Z_{mn} + Z_{mn}^{g}$$

where, Z_{mn}^{g} is the GTD contribution to the impedance matrix.

Example: A monopole of length L, mounted on a square ground plane of side length d, is shown in Fig. 2.1. It is required to determine the current distribution on the monopole.

This problem may be divided into two subproblems. The first is a monopole on an infinite ground plane; to account for the reflected rays from the plate. The second is the diffraction from the edges and vertices of the plate. Incidentally, the image theory can be applied to the first subproblem which yields a dipole of length $2L$. The dipole in free space can be easily formulated by the MoM. In the second subproblem, the diffraction can be computed by GTD; there are only four stationary points denoted by $Q1$, $Q2$, $Q3$ and $Q4$ in Fig. 2.1. Z_{mn}^{g}, in this example, represents the tangential component of the total (from the four stationary points) diffracted electric field evaluated at the center of segment m, due to the incident rays from the current element at segment n on the monopole.

Evaluation: This approach is useful for problems consisting of a radiating element on or near a large conducting body with known diffraction coefficients. However, in GTD, the diffraction coefficients are available only for a few canonical problems.

The current approach: Here, the GTD diffraction coefficients need not to be known. The idea is to divide the structure concerned into two regions: a MoM region and a GTD region. Two cases will be considered: Case 1 uses current samples with known forms and unknown coefficients in the GTD region. Case 2 is addressed to scattering from bodies of revolution (BOR), and incorporates the known Fock current solutions [20] and [21] , in the GTD region, into the MoM procedure; the known current terms

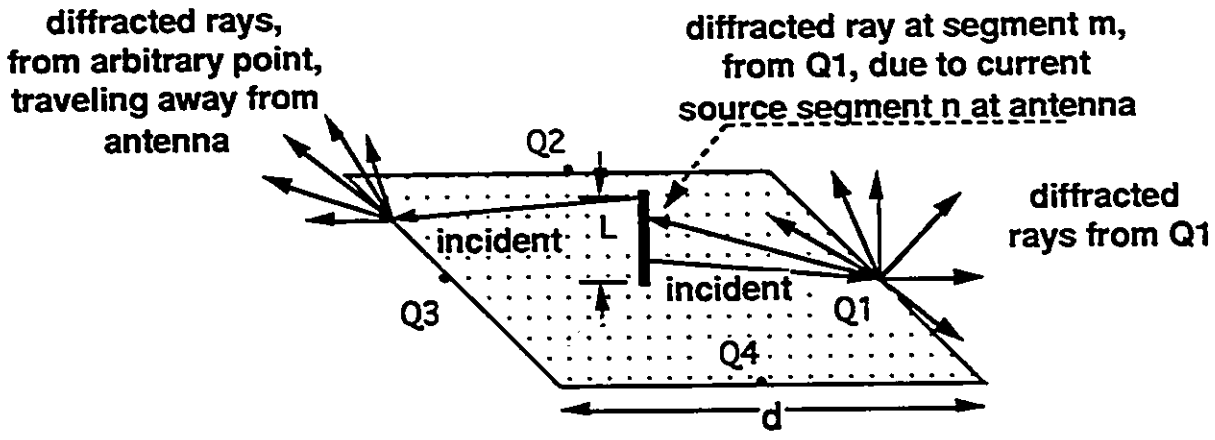

Figure 2.1: A monopole on a finite ground plane

are augmented to the excitation terms.

CASE 1: The combination is accomplished by using MoM current samples with a known form and unknown diffraction coefficients, in the regions away from the diffraction edges; normally few samples are sufficient. These regions are called the GTD regions. Otherwise, conventional MoM current samples are used.

The following example illustrates the use of this technique. The same idea can be applied to other problems.

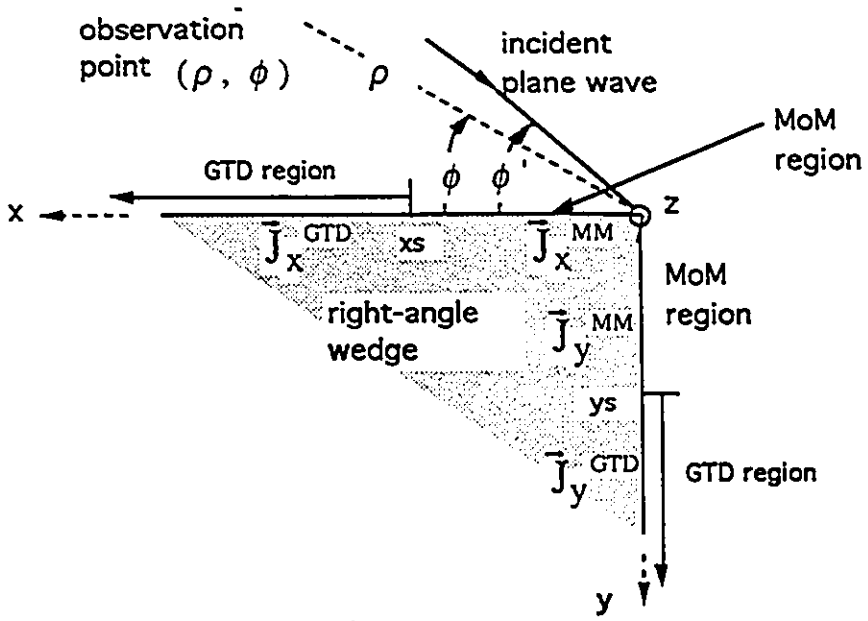

Figure 2.2: A plane wave incident on a right-angle wedge

Example: The canonical problem of diffraction from a perfectly conducting wedge,

in Fig. 2.2, will be analysed using the present approach. A transverse electric (TE) plane wave is incident at an angle of ϕ'; the magnetic field has only z-component. (ρ, ϕ, z) are the cylindrical coordinates. The primed and unprimed variables refer to the source (the incident wave in this example) and the observation coordinates, respectively.

The diffracted field in the GTD region can be written as, [22] and [23]

$$\vec{H}^d = \hat{z} D(\phi, \phi') \frac{e^{-jk_0\rho}}{\sqrt{\rho}} \tag{2.1}$$

provided that the observation point is not close to a shadow boundary defined by $\phi \pm \phi' = 180^0$. D is the unknown diffraction coefficient, k_0 is the free space wave number, and $j = \sqrt{-1}$. Note that D is independent of the range ρ.

The current density on the surface of a perfect conductor is related to the total magnetic field by

$$\vec{J} = \hat{n} \times \hat{z} H \tag{2.2}$$

The total field is the superposition of the incident, reflected and diffracted components

$$\vec{H} = \vec{H}^i + \vec{H}^r + \vec{H}^d \tag{2.3}$$

Substituting (2.1) and (2.3) into (2.2) yields the current density in GTD region, namely

$$\vec{J}^{GTD} = \hat{n} \times \hat{z}(H^i + H^r + D(\phi, \phi') \frac{e^{-jk_0\rho}}{\sqrt{\rho}}), \ for \rho > \lambda_0/4 \tag{2.4}$$

in which λ_0 is the wavelength, and the only unknown being D. To solve for the unknown coefficient D of the wedge, consider the magnetic field integral equation (MFIE) for the TE case

$$J + [\hat{z} \cdot \nabla \times \int_S \vec{J} G_0(\vec{\rho}, \vec{\rho}') \, dS'] = -H^i \tag{2.5}$$

where the integration is on the surface of the wedge S, and G_0 is the two dimensional (2D) free-space Green's function defined by

$$G_0(\vec{\rho}, \vec{\rho}') = \frac{H_0^{(2)}(k_0|\vec{\rho} - \vec{\rho}'|)}{4j} \tag{2.6}$$

where $H_0^{(2)}$ is the Hankel function of the second kind and zero order.

The total surface current can be defined as,

$$J = \begin{cases} J_y^{GTD}, & ys \le y \le \infty, x = 0 \\ J_y^{MM}, & 0 \le y \le ys, x = 0 \\ J_x^{MM}, & 0 \le x \le xs, y = 0 \\ J_x^{GTD}, & xs \le x \le \infty, y = 0 \end{cases} \tag{2.7}$$

J^{MM} is the current in the MoM region around the edge, which can be expanded using conventional basis functions (e.g. pulse functions) with unknown amplitudes.

Substitution of (2.7) into (2.5) and using (2.4) and (2.6) yields an integral equation with the unknowns being the diffraction coefficients D in the GTD regions, and the currents amplitudes in the MoM regions. Sampling both J^{MM} and J^{GTD} by the MoM testing functions leads to a linear system of equations that can be solved for the unknown diffraction coefficients and currents amplitudes.

Conclusion: The approach can be used for problems involving scatterer consisting of perfectly conducting large surfaces (planar, or smooth and convex) and small regions with unknown diffraction coefficients (e.g. vertix, or aperture). It is to be observed that problems consisting of arbitrarily shaped conducting body, or involving inhomogeneities (e.g. penetration through an aperture into a nonhomogeneous medium) are not within the domain of application of this method.

CASE 2: The basic problem considered is the scattering from large perfectly conducting BOR having small irregularities. Galerkin technique, based on the EFIE formulation, is applied to the irregular region. The current distributions on the remaining smooth convex region are obtained from Fock theory [20] and [21]. These known Fock currents are substituted into the EFIE and then sampled by the testing functions of Galerkin technique to form an equivalent forcing term i.e. appear in the voltage matrix.

Fig. 2.3 shows a conducting BOR illuminated by a plane wave. The tangential

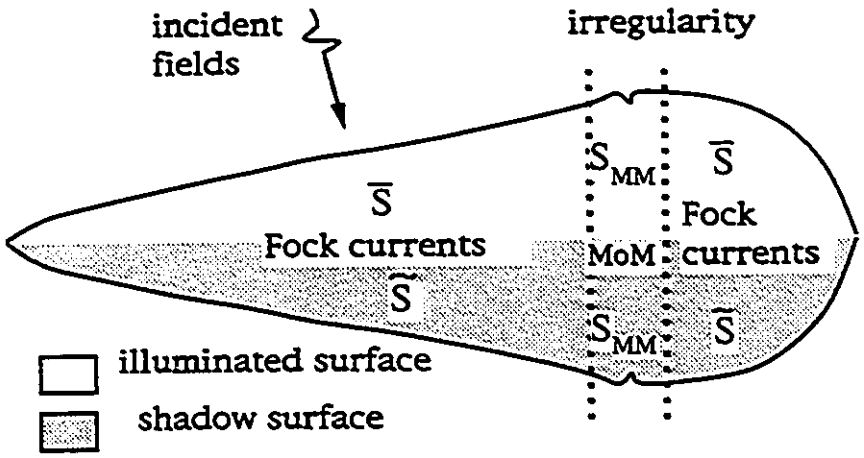

Figure 2.3: Body of revolution scatterer

electric field vanishes on the surface

$$-\hat{n} \times \vec{E}^i = \hat{n} \times \vec{E}^s = -L\vec{J} \tag{2.8}$$

$\vec{E}^s$ is the scattered electric field, $\hat{n}$ is the outward unit vector normal to the surface S, and,

$$L\vec{J} = j\omega\mu \int_S [\vec{J} + \frac{1}{k^2}\nabla\nabla' \cdot \vec{J}] G_0(\vec{r}, \vec{r'}) dS' \tag{2.9}$$

ω is the radian frequency, μ is the permeability of the ambient medium, ∇ and ∇' are the surface gradients on the body with respect to the unprimed and primed variables respectively, and the three dimensional (3D) Green's function in free space is defined by:

$$G_0(\vec{r}, \vec{r'}) = \frac{e^{-jk_0R}}{4\pi R}, \ \vec{R} = \vec{r} - \vec{r'} \tag{2.10}$$

in which r is the spherical coordinate.

The smooth surface region where the current distribution is available in terms of the Fock functions is divided into an illuminated region $\tilde{S}$ and a shadow region $\bar{S}$.

The remaining region is denoted by S_{MM}. For convenience, S_{MM} can include both illuminated and shadow regions. Eqn. (2.8) becomes,

$$L_{S_{MM}}\vec{J} = \hat{n} \times \vec{E}^i - L_{\bar{S}}\vec{J} - L_{\tilde{S}}\vec{J} \tag{2.11}$$

where, the right-hand side is known; the incident field and the Fock currents on $\bar{S}$ and $\tilde{S}$.

Applying the Galerkin technique to equation(2.11) (expansion and testing functions are similar), yields an algebraic system of equations,

$$[Z_n][I_n] = [V_n] - [\bar{V}_n] - [\tilde{V}_n]$$

where, $[Z_n]$ is the generalized impedance matrix containing the interactions of the MoM region S_{MM}. $[V_n]$, $[\bar{V}_n]$ and $[\tilde{V}_n]$ represent the generalized voltage matrices corresponding to the incident field, the illuminated and shadow surface Fock currents, respectively. $[I_n]$ consists of the unknown MoM current coefficients.

Evaluation: The number of unknowns needing a numerical solution are reduced; the MoM representation does not span the whole surface but restricted to the irregular regions of the surface. However, the applicability of the formulation is limited to smooth convex BOR with small irregularities.

2.1.2 MoM Combined with Quasi-Static Techniques

The quasi-static equations may be viewed as the asymptotic low frequency expansion of the full-wave equations [28].

The basic geometry considered is thin-wire antenna with an electrically very small subregion(s) [28]-[30], depicted in Fig. 2.4(a). The quasi-static equations are applied in the very small subregion(s), called the quasi-static subregions, and the full-wave equations otherwise. Coupling of both sets of equations is accomplished via the continuity equation. The resulting equations are solved by the MoM with point matching.

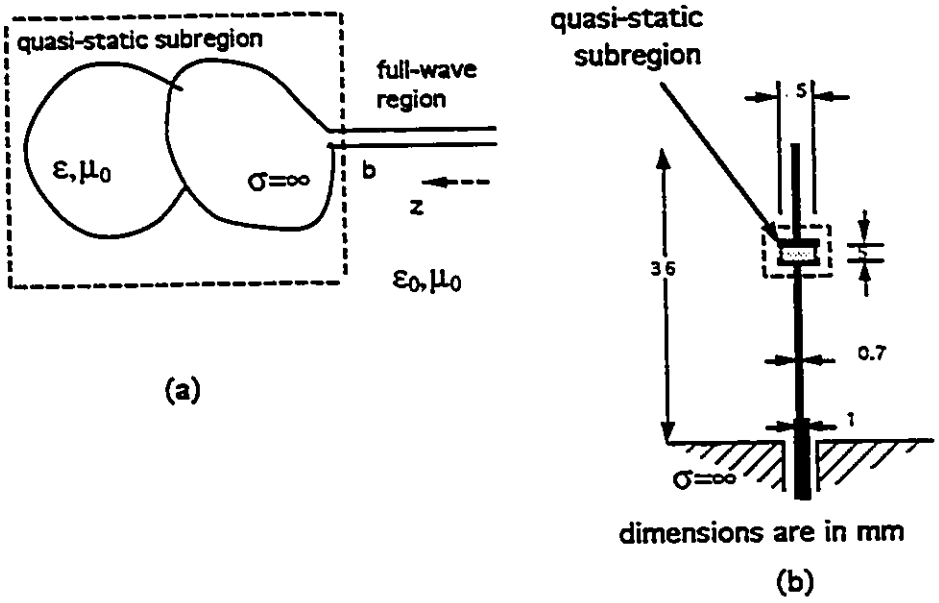

Figure 2.4: Wire antenna with a quasi-static sub-region

The assumption made in the quasi-static subregions is that $k_i D << 1$, where k_i is the wavenumber in the i^{th} dielectric region, and D is the overall dimension of the quasistatic subregion. Also in order to neglect the magnetic induction effects (the nature of the quasi-static subregion is assumed to be capacitive) [29],

$$|k_i^2 R \vec{J}_s| << |\nabla \cdot \vec{J}_s| \tag{2.12}$$

R is within the quasi-static subregions, and $\vec{J}_s$ is the electric current density on the conductors.

The quasi-static subregions: The charge density ρ_s (at the interface between two dielectrics i and j characterized by the relative permittivities ϵ_{ri} and ϵ_{rj}) is identified by

$$\frac{\epsilon_{ri} + \epsilon_{rj}}{2\epsilon_0} \rho_s(\vec{r}) = -(\epsilon_{ri} - \epsilon_{rj}) \hat{n}_i \cdot \vec{E}^i(\vec{r}) - (\epsilon_{ri} - \epsilon_{rj}) \hat{n}_i \cdot \frac{1}{4\pi\epsilon_0} \int_{S_q} \rho_s(\vec{r'}) \frac{\vec{R}}{R^3} \, ds' \tag{2.13}$$

$\vec{r}$ is on the interface between two dielectric regions i and j, ϵ_0 is the free space permittivity, $\hat{n}_i$ is the inward normal unit vector to subregion i,and S_q represents all the dielectric/dielectric and conductor/dielectric interfaces. Also, $\vec{E}^i$ is the incident field from the full wave region evaluated at the interface ij in the quasi-static subregions, and given by

$$\vec{E}^i(\vec{r}) = -\int_{S_f} [j\omega\mu_0 (\hat{n}_i' \times \vec{H}_i) G_i - (\hat{n}_i' \cdot \vec{E}_i) \nabla' G_i] \, ds' \tag{2.14}$$

$\vec{r}$ is on the ij interface in the quasi-static subregions, the primed coordinates are the source coordinates in the full-wave region and the integration is over the full-wave region conductor surface S_f, see figure 2.4 . Also G_i is the Green's function.

The potential V_k on each conductor k satisfies,

$$V_k = \phi^i(\vec{r}) + \frac{1}{4\pi\epsilon_0} \int_{S_q} \rho_s(\vec{r'}) \frac{1}{R} \, ds' \tag{2.15}$$

ϕ^i is the incident potential derived from the incident field $\vec{E}^i$, and ρ_s is the surface charge density. Since V_k is an unknown on each conductor, another equation is needed.

This equation is the conservation of free charge on each conductor,

$$\int_{S^f} \rho_s(\vec{r})\ ds + \epsilon_{ri} \int_S \rho_s(\vec{r})\ ds = q \tag{2.16}$$

S^f represents all parts of the conductor k that are in the full-wave region, S all the conductor/dielectric interfaces in the quasi-static subregions, and q is a known total charge on the conductor (usually assumed to be zero).

The full-wave region: The thin-wire can be analysed by the usual thin-wire integral equation, augmented by the field due to the equivalent charges in the quasi-static subregions. Assuming the wire is along the $z-$axis, and placed in free space

$$-\vec{E}_s(z)\cdot\Delta\vec{z} = \frac{-j\Delta\vec{z}}{\omega\epsilon_0}[k_0^2\int_{wire} G_0 I(z')\ dz' + \hat{z}\frac{\partial}{\partial z}\int_{wire} G_0 \frac{\partial}{\partial z'} I(z')\ dz'] + \vec{E}^q(\rho_s, z)\cdot\Delta\vec{z} \tag{2.17}$$

where $\vec{E}_s(z)$ is the source field which is nonzero only on the source location, $\Delta\vec{z}$ is a vector along the $z-$axis, and $I(z)$ is the unknown current along the wire. Also, $\vec{E}^q(\rho_s, z)$ is the field due to the equivalent charges in the quasi-static subregions evaluated on the wire in the full-wave region,

$$\vec{E}^q(\rho_s, z) = -j\omega\mu_0 \int_{S_q} \vec{J}_s(\vec{r'}) G_0(\vec{r}, \vec{r'})\ ds' - \frac{1}{\epsilon_0}\nabla \int_{S_q} \rho_s(\vec{r'}) G_0(\vec{r}, \vec{r'})\ ds' \tag{2.18}$$

The surface current density $\vec{J}_s(\vec{r'})$ can be expressed in terms of $\rho_s(\vec{r'})$ by integrating the continuity equation

$$\nabla\cdot\vec{J}_s = -j\omega\rho_s \tag{2.19}$$

with the assumption that the current vanishes at the intersection between the conductor end and the axis of symmetry within the quasi-static subregion.

Coupling of the two solutions: The only unknown in the full-wave region is the current distribution $I(z')$ in (2.17). Therefore, it would be useful to rewrite (2.16) in terms of the current in the full-wave region. The first term in (2.16) multiplied by $-j\omega$ becomes,

$$I_b = -j\omega \int_0^b \rho_l(z)\ dz \tag{2.20}$$

where b is the interface between the full-wave and quasi-static region, ρ_t is the charge density along the wire extending between $z = 0$ and $z = b$, and $I(0) = 0$. Thus applying an integral form of the continuity equation to each quasi-static subregion ensures sufficient equations to solve for the unknowns.

Example: A capacitor-loaded quarter-wave monopole on a ground plane is shown in Fig. 2.4(b). The capacitor plates are cylindrical with an enclosed dielectric of permittivity ϵ. The capacitor represents the quasi-static subregion. The region exterior to the dashed boundary is the full-wave region.

Limitations: This method cannot solve a continuously inhomogeneous dielectric in the quasi-static subregions. Further, each conductor and dielectric in the quasi-static subregions is assumed to contain the axis of symmetry, in order to be able to apply the boundary condition viz. vanishing of the electric current at the intersection of the conductor end and the axis of symmetry. Therefore, arbitrarily shaped 3-dimensional geometries cannot be handled by this approach.

Advantages: This method is superior to the methods modelling the quasi-static region by a lumped load, since these methods compute the lumped load value separately without taking into account the coupling with the full-wave region. Also, this method is simpler, yet gives accurate results, than the methods using full-wave analysis in the small regions since the kernels of the quasi-static integrals are simpler than the corresponding kernels of the full-wave integrals. Further, full-wave analysis tends to be unstable when applied to electrically small complicated structures.

2.2 Numerical Method Combined with Analytical Solution

MoM Combined with Green's Function

This hybrid method combines the Green's function of a particular geometry with MoM [31]-[35]. The desired field quantity is expressed in terms of a superposition integral of the Green's function of the problem geometry weighted by the excitation distribution. After that, the MoM procedure is applied to this integral.

In the following, the hybrid is illustrated by means of an example.

Example: A monopole protruding from a conducting sphere is shown in Fig.2.5, [31]. The tangential electric field vanishes along the perfectly conducting wire(s):

$$\vec{r} \cdot \vec{E}^i + \vec{r} \cdot \vec{E}^s = 0 \tag{2.21}$$

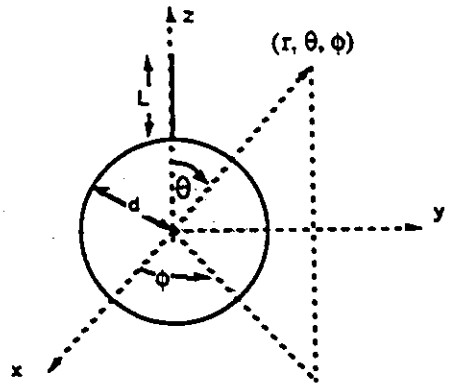

Figure 2.5: A monopole mounted on a conducting sphere

Expressing the scattered electric field in Eq.(2.21) in terms of the Green's function $\Gamma_{rr}(r, r')$,described in [31] ,of a point current element in the presence of a conducting

sphere, yields:

$$\vec{r} \cdot \vec{E}^i = -\int_{wire(s)} I(r')\Gamma_{rr}(r, r')dr' \tag{2.22}$$

where $I(r')$ is the current on the wire. This equation is then solved numerically for the current distribution by the MoM.

*Evaluation:*Reduces the number of unknowns needing solution, since the integration is only over the sources. Also, it could be used for arbitrarily large spheres, in the example, where the MoM solution is prohibited by the requirements on computer resources. However,the Green's function need to be derived for each different problem geometry. Further, if the problem concerned involves inhomogeneities and/or complex geometries, then the derivation of the Green's function is very difficult if not impossible. Therefore, this combination is recommended for simple geometries where the Green's function is known.

2.3 Combinations of Different Numerical Methods

The problem domain is divided into two regions. The first region is bounded and contains all media inhomogeneities and anisotropies whereas the second region is unbounded, but homogeneous and isotropic. The idea is to use an integral equation method (MoM) in the homogeneous unbounded region and a differential equation method (e.g. finite method) in the inhomogeneous region. Thus, these hybrid combinations assume that the inhomogeneities are confined to a bounded region [36]-[69] . Coupling of the two solutions is accomplished by virtue of the continuity conditions at the interface. These combinations have the advantage that arbitrarily shaped bodies can be handled. Furthermore, only the inhomogeneous medium is discretized. However, in all cases a full and dense matrix (since an integral equation method always produces a full and dense matrix) has to be inverted. Further, in the FEM-boundary integral method, the solution of the bounded region has to be obtained for each basis

function interpreted as Dirichlet boundary condition.

Different combinations are described and evaluated in what follows,

2.3.1 MoM Combined with Finite Methods

The problem addressed by this method is the scattering snd penetration of an inhomogeneous body due to an external source. This HNM is based on using equivalent surface currents as sources for the scattered field in the unbounded medium, and as boundary conditions for the bounded region. A finite method is used in the inhomogeneous region, and an integral equation solution in the surrounding medium. The two solutions are combined by the continuity conditions [36]-[62].

Two cases may be distinguished in this method, namely

- Case *I*: The external source is a plane wave [36]-[59].
- Case *II*: The external source is a radiating element close to the scatterer [60]-[62].

These two cases are introduced in the following

Case *I*: Plane Wave Incidence

The problem consists of an inhomogeneous body irradiated by an incident wave, Fig. 2.6(a). It is required to determine the field everywhere. The hybrid approach is based on the field equivalence principle [47, Ch. 3], whereby the field in the unbounded isotropic homogeneous region is uniquely specified by an equivalent surface currents, Fig.2.6(b), and the field in the inhomogeneous body is uniquely specified by the tangential magnetic field on the surface of the body, Fig.2.6(c). The unbounded region is solved by the MoM whereas the inhomogeneous region is solved by the FEM. The two solutions are coupled via the continuity conditions on the surface of the body.

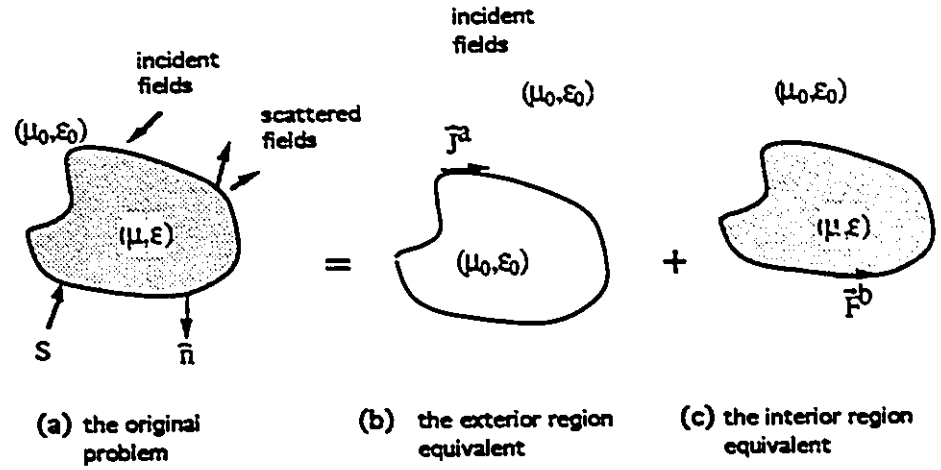

Figure 2.6: A nonhomogeneous scatterer and the equivalent problem

Formulation: The tangential components of the electric and magnetic fields are continuous across the boundary surface S.

$$\hat{n} \times \vec{E}^i + \hat{n} \times \vec{E}^s(\vec{J}^a) = \hat{n} \times \vec{E}^b(\vec{F}^b), \quad \hat{n} \times \vec{H}^i + \hat{n} \times \vec{H}^s(\vec{J}^a) = \vec{F}^b \tag{2.23}$$

$\hat{n}$ is the unit vector normal to S, $\vec{J}^a$ is the equivalent electric current on S for the unbounded region, $\vec{E}^s$ and $\vec{H}^s$ are the scattered fields in the unbounded region, $\vec{F}^b$ is the tangential magnetic field on S and serves as a boundary condition for the solution in the inhomogeneous body, and $\vec{E}^b$ is the electric field on S associated with the solution in the body.

Both $\vec{J}^a$ and $\vec{F}^b$ are equivalent surface electric currents. Alternatively, equivalent magnetic currents, or a combination of magnetic and electric currents can be used. A careful choice for a paticular problem simplifies the formulation.

Eqns. (2.23) contain four unknowns viz. $\vec{E}^s$, $\vec{H}^s$, $\vec{E}^b$ and $\vec{F}^b$; $\vec{E}^s$ and $\vec{H}^s$ can be expressed in terms of $\vec{J}^a$ via a free-space integral equation, reducing the unknowns to three. Obviousley, one more equation is needed. This equation can be obtained from the FEM solution in the body.

The integral equation in free space [48] and [49],

$$\vec{E}^s(\vec{J}^a) = -jw\mu_0 \int_S \vec{J}^a G_0(\vec{r},\vec{r}')\, ds' + \frac{\nabla}{jw\epsilon_0} \int_S \nabla'_S \cdot \vec{J}^a G_0(\vec{r},\vec{r}')\, ds',\ \vec{H}^s(\vec{J}^a) = \frac{\nabla \times \vec{E}^s(\vec{J}^a)}{-jw\mu_0} \tag{2.24}$$

Applying the FEM to the body with $\vec{F}^b$ as a boundary condition yields

$$[A][\vec{E}^b] = [\vec{F}^b] \tag{2.25}$$

where, $[A]$ is a sparse and banded matrix, $[\vec{E}^b]$ is the unknown electric field in the body (both on S and interior to S). $\vec{E}^b$ on S as a function of $\vec{J}^a$ can be extracted from the FEM solution and substituted into the MoM procedure applied to Eqns. (2.23)-(2.24).

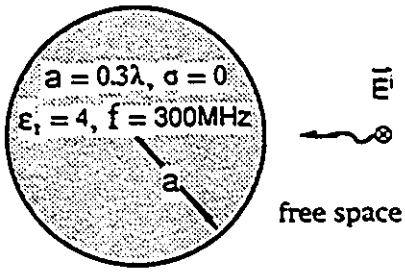

Figure 2.7: A cross section of a circular cylinder scatterer

Example: To validate the present technique, the echo width of a homogeneous dielectric cylinder under TM plane wave incidence, Fig. 2.7, was computed and compared with the exact eigenfunction solution. The maximum relative error was 4%, [49]. The number of finite elements in the radial and angular directions was 12 and 32, respectively. Also 30 terms was summed in the Fourier series of the exact solution.

Advantages: The FEM matrix needing solution, Eqn.(2.25), is sparse and banded. In addition, the MoM matrix is full but small (it's order is N; the number of nodes on the boundary surface S). The method facilitates the use of the standard MoM techniques.

Limitations: For resonant structures, the equivalent surface currents representation, presented in this method, is not valid.

Case *II*: Source is Close to Scatterer

An EM source radiating an inhomogeneous body is shown in Fig. 2.8. The boundary conditions on the source boundary are known. It is required to determine the field in the body.

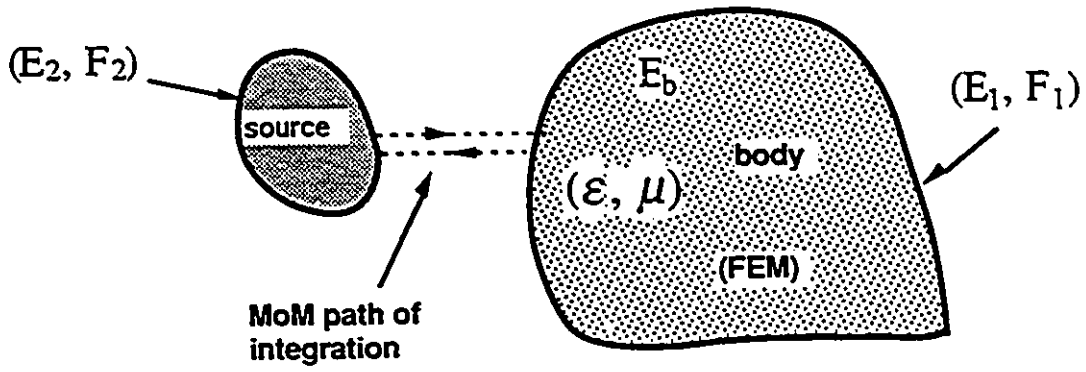

Figure 2.8: An electromagnetic source radiating a nonhomogeneous body

Consider the FEM formulation described in [60]. The FEM applied to the body yields

$$[A]\begin{bmatrix} E_b \\ E_1 \end{bmatrix} = [B][F_1] \tag{2.26}$$

$[E_b]$ and $[E_1]$ are associated with the electric field inside and on the surface of the body, respectively, $[F_1]$ involves the equivalent electric currents on the surface of the body, also $[A]$ and $[B]$ involve the shape functions of the body.

The MoM applied to the ambient medium yields

$$[C]\begin{bmatrix} F_1 \\ F_2 \end{bmatrix} = [D]\begin{bmatrix} E_1 \\ E_2 \end{bmatrix} \tag{2.27}$$

in which, $[C]$ and $[D]$ are matrices with known entries, $[F_2]$ and $[E_2]$ involve the magnetic and electric fields, respectively, on the surface of the source.

From (2.27)

$$\begin{bmatrix} F_1 \\ F_2 \end{bmatrix} = [C]^{-1}[D]\begin{bmatrix} E_1 \\ E_2 \end{bmatrix} = \begin{bmatrix} Z_{11} & Z_{12} \\ Z_{21} & Z_{22} \end{bmatrix}\begin{bmatrix} E_1 \\ E_2 \end{bmatrix} \tag{2.28}$$

Using the first row in this equation to eliminate $[F_1]$ in (2.26),

$$[A]\begin{bmatrix} E_b \\ E_1 \end{bmatrix} - [B][Z_{11}][E_1] = [B][Z_{12}][E_2] \tag{2.29}$$

where $[E_2]$ is known. This is a system of $N \times N$ equations with N unknowns. N being the total number of nodes on and inside the body.

The hybrid method was used to predict the fields inside the patients due to the hyperthermic EM sources,[61] and [62].

Evaluation: The matrix to be solved is not sparse. It is well known that sparsity is one of the most desirable featurs of the FEM. However, if equation (2.26) was used to eliminate $[E_1]$ from (2.27), the FEM would be sparse and the MoM matrix is full but small.

The method is useful for evaluating the electromagnetic fields induced in the patients by EM sources in the course of hypothermic therapy.

2.3.2 Finite Element-Boundary Integral Method

The FEM is combined with the extended boundary condition method (EBCM) to solve the problem of scattering from an inhomogeneous body as depicted in Fig. 2.9. The equivalent currents, appearing in the surface integral of the EBCM, are expanded into a set of basis functions numerically calculated by the FEM. After that, the surface integrals are solved according to the EBCM procedure.

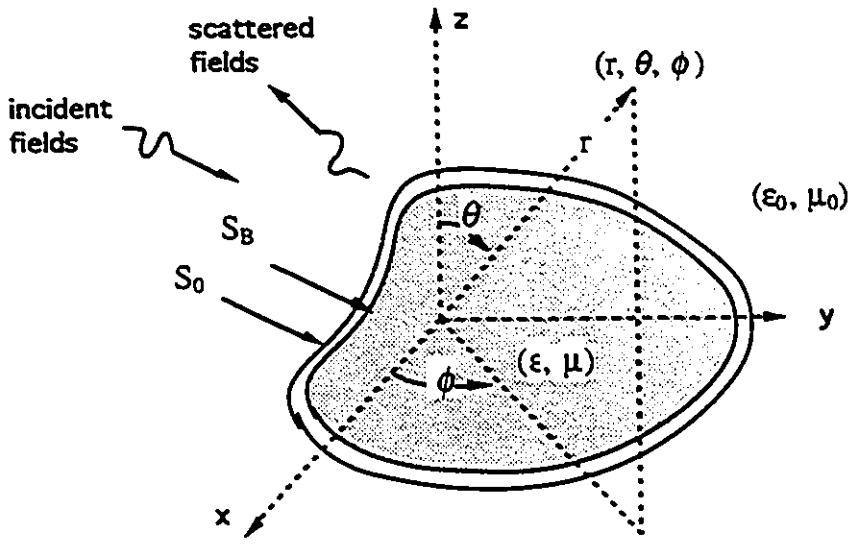

Figure 2.9: Inhomogeneous scatterer

Formulation: Referring to Fig. 2.9, S_B is a surface enclosing the body and S_0 is enclosing S_B, [63]. Here, S_B is chosen to be the body surface and S_0 conforming with S_B to minimize the numerical effort. Also, $\hat{n} \times \bar{H}$ and $\bar{E} \times \hat{n}$ are the equivalent currents on S_B.

Using the spherical vector harmonics $\bar{M}$ and $\bar{N}$ described in [64], the incident and

scattered fields in free space are expanded as follows [63]

$$\vec{E}^i = \sum_v D_v[a_v \vec{M}_v^1(k_0\vec{r}) + b_v \vec{N}_v^1(k_0\vec{r})],\ \vec{E}^s = \sum_v D_v[f_v \vec{M}_v^4(k_0\vec{r}) + g_v \vec{N}_v^4(k_0\vec{r})] \quad (2.30)$$

where, a_v and b_v are known coefficients, while f_v and g_v are unknowns. D_v is a normalization constant, and v is an index combining the spherical indices.

The EBCM formulation gives the following four surface integrals [63]

$$\oint_{k_0^2 S_B} [\vec{N}_v^4 \cdot (\hat{n} \times \vec{E}) - j\vec{M}_v^4 \cdot (\hat{n} \times \eta_0 \vec{H})] d(k_0^2 S) = -j\pi a_v \quad (2.31)$$

$$\oint_{k_0^2 S_B} [\vec{M}_v^4 \cdot (\hat{n} \times \vec{E}) - j\vec{N}_v^4 \cdot (\hat{n} \times \eta_0 \vec{H})] d(k_0^2 S) = j\pi b_v \quad (2.32)$$

$$j\pi f_v = \oint_{k_0^2 S_B} [\vec{N}_v^1 \cdot (\hat{n} \times \vec{E}) - j\vec{M}_v^1 \cdot (\hat{n} \times \eta_0 \vec{H})] d(k_0^2 S) \quad (2.33)$$

$$j\pi g_v = \oint_{k_0^2 S_B} [\vec{M}_v^1 \cdot (\hat{n} \times \vec{E}) - j\vec{N}_v^1 \cdot (\hat{n} \times \eta_0 \vec{H})] d(k_0^2 S) \quad (2.34)$$

The general approach to the solution of the scattering problem is as follows,

1. Discretize the region enclosed by S_0 into finite elements.

2. Choose a set of basis surface currents on S_0. This set, termed the "initial set" is arbitrary as far as it is complete, and can be either full-domain or sub-sectional basis functions.

3. Obtain a FEM solution for each initial basis function interpreted as a Dirichlet boundary condition on S_0. The obtained tangential magnetic and electric fields on the body surface S_B are termed "the informed set". The informed set contains information about the inhomogeneity and the shape of the body.

4. Expand the unknown equivalent surface currents $\hat{n} \times \vec{H}$ and $\vec{E} \times \hat{n}$ in Eqns(2.31)-(2.34) in terms of the informed set. Then apply the EBCM procedure to obtain the unknown coefficients of the scattered field.

To verify the method, it was applied to homogeneous bodies of revolution and the solution was compared to the pure EBCM solution. The two solutions were in good agreement, [63].

Evaluation: The EBCM matrix needing inversion is full and dense, but small (it's order is the number of unknowns on the surface S_B). Further, FEM solution has to be obtained for each initial basis function applied as a Dirichlet boundary condition. However, the FEM matrix to be solved is sparse which enables the use of efficient and fast algorithms. Also, the body region only need to be discretized: thus the numerical effort is reduced compared to the previously developed unimoment method [65]-[67] whereby the finite element mesh is used inside a circumscribing sphere. On the other hand, the spherical expansions as used in the finite element-boundary integral method have difficulties to converge for elongated bodies (i.e. length to diameter ratio exceeding 10). To overcome this limitation, the so called "F^3" (field feedback formulation) was proposed [52] in which the MoM is used for the exterior region. Specifically, in the F^3 formulation the equivalent surface currents on S_B (both magnetic and electric currents computed from the tangential fields on S_B) in terms of the tangential fields on S_0 are extracted from the FEM solution, and then inserted back into the MoM integrals. Thus F^3 is essentially similar to the MoM/finite method described at the beginning of this Section.

It was not shown in the finite element-boundary integral method how to find the fields penetrated into the body. Here, we suggest the following algorithm to do that:

- Find the scattered field by the hybrid method.
- Evaluate the total field on the scatterer's surface. The tangential components of the fields on the scatterer's surface are the boundary conditions necessary for the FEM.
- Solve the bounded problem by the FEM.

2.3.3 FEM Combined with Generalized Multipole Technique

The generalized multipole technique (GMT) [68] is a numerical method suitable for isotropic, linear, and homogeneous subdomains that can be infinite in extent. In this method, the EM fields in each subdomain are approximated by expansions in terms of multipoles; the multipole is an expansion in terms of a set of basis functions with unknown coefficients. The basis functions are analytical solutions of the governing Helmholtz equation in the subdomain concerned. These analytical solutions are obtained by the method of separation of variables in the spherical coordinates for the 3D case, and in the cylindrical coordinates for the 2D case. Different multipoles have different origins chosen outside the subdomain of interest to avoid the singularity at the center of the multipole. The continuity conditions at the boundaries are satisfied numerically by using the generalized point matching technique (GPM), where an overdetermined system of equations is obtained. This system is usually solved by the method of least squares. Thus GMT uses more matching points than unknowns. Incidentally, one might think of this method as Galerkin technique with prescribed basis functions.

For problems involving continuously inhomogeneous subdomains, GMT is not the proper solution, but FEM is one of the strongest candidates for such subdomains. In this hybrid, the FEM is applied to the inhomogeneous region, giving [69]:

$$[A_I][U_I] + [A_B][U_B] = [\psi] \tag{2.35}$$

$[U_I]$ and $[U_B]$ are the unknown nodal vectors inside and on the boundary of the inhomogeneity, respectively. $[A_I]$ and $[A_B]$ are known matrices, and $[\psi]$ is a known excitation vector.

The GMT applied to the exterior region gives the following system of equations:

$$[U_B^{GMT}] = [P][D] \tag{2.36}$$

in which, $[U_B^{GMT}]$ is the GMT solution at the boundary, $[P]$ is a known matrix, and

$[D]$ includes the unknown coefficients.

From the continuity conditions, $[U_B]$ is identical to $[U_B^{GMT}]$. Replacing $[U_B]$ in (2.35) by $[U_B^{GMT}]$ in (2.36) yields,

$$[A_I][U_I] + [A_B][P][D] = [\psi] \tag{2.37}$$

A corresponding functional can now be established, and then minimized to determine the unknowns. This functional covers the whole space, and the integration in the homogeneous unbounded domain is converted to a surface integral on the boundary by using Green's theorem.

Limitations: The method was oriented only toward electrical machines applications, and the matrix to be solved was not sparse. Further, the boundary integrations used are time consuming. Also the accuracy of the solution depends on the choice of the origins of the multipoles (several rules of thumb are given in [68]). In addition, GMT cannot deal simply with sharp points and edges.

2.4 Combining Different Formulations

The hybrid combinations presented in this section can be thought of as extensions to a numerical method. The first combines the EFIE for thin wires with the MFIE for a conducting body. The second can be thought of as importing ideas from other methods viz. importing the concept of finite volume elements into the MoM.

MoM/EFIE-MFIE:

The EFIE is suitable for thin wires whereas the MFIE is suitable for voluminous conducting body. Consequently, the EFIE is applied to the wires attached to a conducting body, and the MFIE is applied to the conducting body itself. The mutual coupling between the wires and the body is taken into account through the source terms in the integral equations. The resulting equations are solved using the MoM.

Example: Fig. 2.10 shows an arbitrarily shaped conducting body C with straight wire antennas A and passive booms B. The MFIE on the surface of a perfectly conducting body S is [70],

$$-\frac{1}{2}\bar{J}(\vec{r}) + \hat{n} \times \int_S^* \bar{J}(\vec{r'}) \times \nabla' G_0 \, dS' = -\hat{n} \times \bar{H}^i(\vec{r}) \tag{2.38}$$

in which $\hat{n}$ is an outward normal to the surface S, and the star indicates that the integral is evaluated on the body surface except the point $\vec{r}$. The EFIE for a perfectly conducting thin wire is [70] ,

$$\frac{1}{jw\epsilon} \int_L (\frac{\partial^2 G_0}{\partial l^2} + k^2 G_0) I(l') \, dl' = -\hat{l}.\bar{E}^i \tag{2.39}$$

where, the integration is along the wire L, and I is the current on the wire.

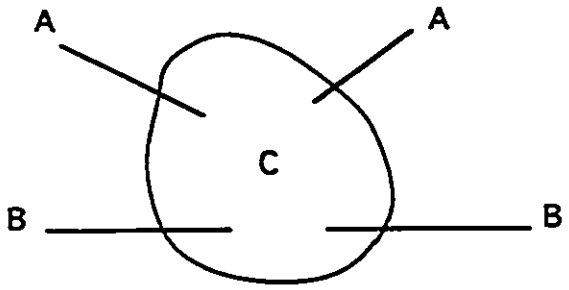

Figure 2.10: Wire antennas A, and passive booms B attached to a conducting body

The coupling between the body and the wire(s) is considered by evaluating the magnetic field induced on the body surface due to the wire(s) current,

$$\hat{n} \times \bar{H} = \hat{n} \times \int_L I(l') \hat{l} \times \nabla' G_0 \, dl' \tag{2.40}$$

and, the electric field along the wire(s) due to the current on the body surface,

$$\hat{l} \cdot \bar{E} = \frac{1}{jw\epsilon} \hat{l} \cdot \int_S \nabla \times (\nabla \times \bar{J} G_0) \, dS \tag{2.41}$$

Applying the MoM to the Eqns.(2.38)-(2.41) generates a linear system of equations that can be solved for the current distributions using standard techniques.

Evaluation : As compared to the hybrid MoM/Green's function method described in section 2.2, only the free space Green's function is needed. Therefore, this method can be applied to arbitrarily shaped body to which wires are connected. On the other hand, this combination cannot be applied to large body in terms of the wavelength due to the large number of unknowns needing solution.

MoM/Volume polarization currents:

A dielectric/magnetic inhomogeneity is replaced by equivalent volume polarization currents whereas the wire is replaced by equivalent surface currents. Then, the reaction integral formulation [71], together with the boundary condition on the wire and the proper conditions in the inhomogeneity, are used to obtain a set of coupled equations. These equations are solved for the unknown current distributions by the MoM.

Example: In Fig. 2.11(a), a wire and an inhomogeneity together with an excitation are shown. The inhomogeneity is charcterized by the permittivity ϵ and permeability μ.

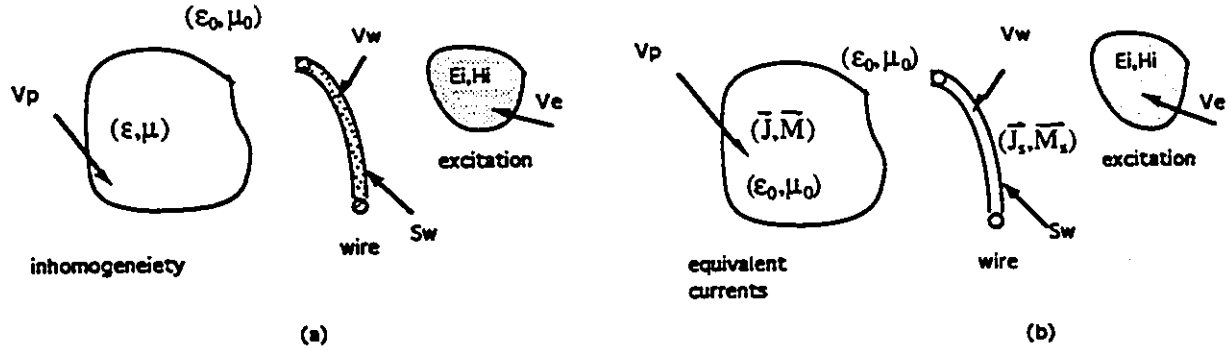

Figure 2.11: Wire antenna with an inhomogeneity and the equivalent problem

The wire has a surface impedance Z_s and is replaced, see Fig. 2.11(b), by the unknown equivalent surface currents [72]:

$$\vec{J}_s = \hat{n} \times \vec{H}, \quad \vec{M}_s = \vec{E} \times \hat{n} \tag{2.42}$$

here, $\hat{n}$ is the outward normal at the wire surface S_w. These currents are related by the surface impedance Z_s.

The inhomogeneity is replaced by the equivalent polarization currents:

$$\vec{J} = jw(\epsilon - \epsilon_0)\vec{E}, \quad \vec{M} = jw(\mu - \mu_0)\vec{H} \tag{2.43}$$

in the ambient medium -free space in this case- as depicted in Fig. 2.11(b). $\vec{E}$ and $\vec{H}$ are the total electric and magnetic fields in the inhomogeneity,

$$\vec{E} = \vec{E}^s(I(l)) + \vec{E}^J(\vec{J}) + \vec{E}^H(\vec{M}) + \vec{E}^i = \frac{\vec{J}}{jw(\epsilon - \epsilon_0)} \tag{2.44}$$

$$\vec{H} = \vec{H}^s(I(l)) + \vec{H}^J(\vec{J}) + \vec{H}^H(\vec{M}) + \vec{H}^i = \frac{\vec{M}}{jw(\mu - \mu_0)} \tag{2.45}$$

where, $\vec{E}^s$ and $\vec{H}^s$ are the fields radiated by the current distribution on the wire. $\vec{E}^J$ and $\vec{H}^J$ are the fields radiated by the electric polarization current. $\vec{E}^H$ and $\vec{H}^H$ are the fields radiated by the magnetic polarization current.

The reaction integral equation (RIE) is used to fix the boundary conditions at the surface of the wire. Therefore, a test source $(\vec{J}_m, \vec{M}_m)$, radiating fields $(\vec{E}^m, \vec{H}^m)$, is placed in the wire volume V_w. The RIE obtained is [72],

$$-\int_0^L I(l)(E_l^m - Z_s H_\phi^m)dl - \int_{V_p}(\vec{J}\cdot\vec{E}^m - \vec{M}\cdot\vec{H}^m)dv = \int_{V_e}(\vec{J}^i\cdot\vec{E}^m - \vec{M}^i\cdot\vec{H}^m)dv \tag{2.46}$$

where, L is the wire length, $I(l)$ is the total current along the thin wire, $\vec{J}^i$ and $\vec{M}^i$ are the known sources, and

$$E_l^m = \frac{1}{2\pi}\int_0^{2\pi}(\hat{l}\cdot\vec{E}^m)\,d\phi, \; H_\phi^m = \frac{1}{2\pi}\int_0^{2\pi}(\hat{\phi}\cdot\vec{H}^m)\,d\phi, \; \hat{\phi} = \hat{l}\times\hat{n} \tag{2.47}$$

Eqns.(2.44)-(2.46) are three coupled equations with three unknown currents viz. $I(l)$, $\vec{J}$ and $\vec{M}$. These equations can be transformed to a linear system of equations, using standard moments method techniques i.e. expansion and weighting.

Evaluation: This approach can handle wire antennas in the presence of arbitrarily shaped dielectric/magnetic inhomogeneity. The size of the overall structure is limited

by the increasing number of unknowns needing solution. Also, the system matrix corresponding to the formulation in this approach is dense, and has a relatively large order being the number of unknowns on the surface of the wire plus the unknowns in the inhomogeneity.

2.5 CONCLUSIONS

There is considerable amount of papers associated with HNM that are distributed in different Journals (e.g. IEEE Transactions on: Antennas and Propagation, Microwave Theory and Techniques, and Magnetics, IEE Proceedings, and the Journal of Wave Motion). Furthermore, several papers deal with the same combination under different titles. In order to simplify matters, an overview of the various HNM available in electromagnetics is presented in this Chapter. An attempt is made to classify the HNM according to the combination used. The classification scheme is

1. Numerical method combined with asymptotic expansion:- MoM with GTD, and MoM with Quasi-static techniques.
2. Numerical method with analytical solution:- MoM with Green's function.
3. Hybrid methods combining different numerical methods:- MoM combined with finite methods, The finite element-boundary integral method, FEM with GMT.
4. Combining different formulations:- EFIE with MFIE formulations of the MoM, and MoM with Volume polarization currents.

An attempt is also made to evaluate the approaches to the hybrid combinations. Also, the domain of application of each hybrid is identified. This might help to choose the proper method for a given problem.

Chapter 3

A Model of External Electromagnetic Interference with Electronic Equipment

The two-dimensional approximation of the interference phenomenon is considered in this Chapter whereby the equipment is assumed to be infinitely long, and thus only the cross section is analysed. This approximation is valid for long equipment with uniform cross section provided that the observation point is not near the ends or a field null. From this assumption, a two-dimensional numerical model of the electromagnetic wave interference with electronic equipment is realized. This model is useful in predicting both the fields that penetrate into the electronic equipment, and the scattered fields.

The model described in this Chapter combines the edge based-finite element method with the asymptotic expansion of the scattered fields. This combination is used to formulate a system of linear equations for the solution of the fields. Using the edge elments, the model has the expected advantage of not producing spurios solutions. Further, the matrix obtained is sparse (or banded) and symmetric. This allows the use of efficient algorithms for sparse and symmetric, or banded and symmetric matrices which significantly reduce the computer storage requirement.

This Chapter is organized as follows: in Section 3.1, the rationale of choosing

the edge elements is outlined. Section 3.2 describes the interference problem and the truncating boundary. The functional of the problem and the treatment of the exterior unbounded domain are presented in Sections 3.3 and 3.4, respectively. Next, using the continuity of the tangential fields to combine the edge element solution with the scattered field solution of the surrounding medium is presented in Section 3.5. After that, the discretization and numerical results are described in Sections 3.6 and 3.7, respectively. Finally, the Chapter concludes with Section 3.8.

3.1 Choice of Edge Elements

As contrasted to conventional finite elements, edge elements associate the degrees of freedom with the circulation of the vector field along the elements edges allowing for discontinuous normal components of the fields at material interfaces [73]. Thus the edge elements have the expected advantage of not producing spurious modes [73]. Further, edge elements can model sharp points and edges without any need for special singular trial functions [74]. For these reasons, the edge elements (specifically, the edge elements proposed in [75]) solution is used in this paper.

3.2 The Interference Problem

The victim is electronic equipment characterized by permittivity ϵ, conductivity σ, and permeability μ, and the source of interference is a plane wave $(\vec{E}^i, \vec{H}^i)$ as shown in Fig. 3.1.

The wave interacts with the outer structure of equipment and consequently the fields $(\vec{E}, \vec{H})$ leak through apertures, holes, and slots that exist in the outermost layer of the structure (e.g. shielding enclosure). Long and narrow slots can be approximated by infinitely long slots [76]. Therefore, only the two dimensional (2D) case is considered here. However, the extension to three dimensional structures is straightforward.

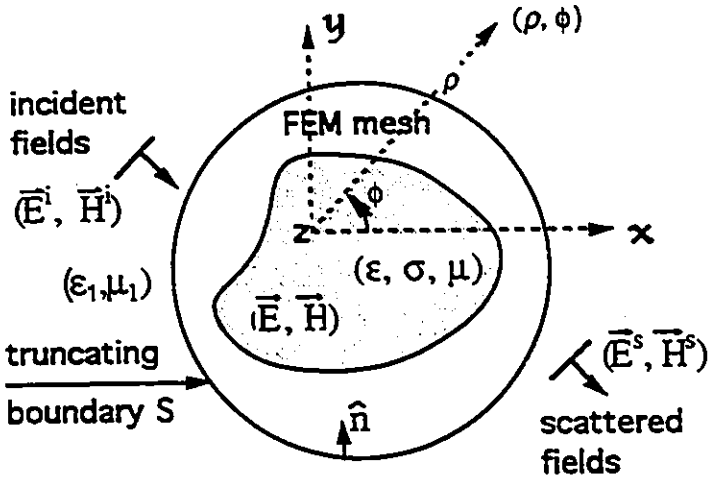

Figure 3.1: Interference problem geometry

In order to compute the penetrated fields, and the scattered fields $(\vec{E}^s, \vec{H}^s)$, the discretization domain is truncated by an artificial boundary S, refer to Fig. 3.1. Thus the problem domain is divided into two regions: the bounded domain, i.e. enclosed by S, and the exterior domain, i.e. external to S. After that, the edge elements are applied to the bounded domain whereas the scattered field in the exterior domain is described by its asymptotic expansion. The two solutions are combined through the continuity conditions on S.

3.3 The Bounded Domain

The fields in this region are governed by the vectorial wave equation expressed as:

$$\nabla \times \frac{\nabla \times \vec{E}}{\mu_r} = k_0^2 \epsilon_c \vec{E}, \qquad \epsilon_c = \epsilon_r - j\frac{\sigma}{\omega \epsilon_0} \tag{3.1}$$

in which, k_0 is the free space wave number, μ_r the relative permeability, ϵ_r the relative permittivity, ω the radian frequency, and σ the conductivity.

Equivalentally, the fields are the solution of the variational equation:

$$\delta F(\vec{E}^*) = 0 \tag{3.2}$$

where, $*$ denotes the complex conjugate, and $\vec{E}^*$ is chosen as the variational parameter in order that the final system of equations will be in terms of $\vec{E}$. The functional F corresponding to the wave equation (3.1) is derived below.

The functional of bounded problems is well known. However, this functional is expressed in terms of only the quantity $\vec{E}$ as in [77], or in terms of both $\vec{E}$ and $\vec{E}^*$ as in [75]. Further, the functional for unbounded problems is given in [37], [53], and [54]. This functional is expressed in terms of $\vec{E}$ only. In this Section, a functional in terms of both $\vec{E}$ and $\vec{E}^*$ for unbounded problems is derived. The advantage of this form is that, using $\vec{E}^*$ as the variational parameter, the quantity $\vec{E}$ can be considered an independent variable, and thus the derivation of the final equations for both FEM and

the boundary condition on S are simplified. In addition, it is found that the functional, derived here, is identical to the energy balance equation obtained via Galerkin method [78].

The derivation is intended for 3D problems, and it is as well valid for 2D problems. For 3D, the domain integral is over the problem volume, and the boundary integral is over the enclosing surface. In the 2D case, the domain integral is over the cross section, and the boundary integral is along the enclosing contour.

The procedure to derive the functional for unbounded problems is: starting from the functional of bounded problems given in [75], the variation is evaluated. The variation for bounded problems is zero since the field is known in advance on the boundary surface. However, the variation of the same functional for unbounded problems does not vanish. Therefore, an additional term is derived and augmented to the functional. This extra term accounts for the unbounded medium outside the boundary surface.

The functional for bounded problems is given by [75]:

$$F^d(\vec{E}^*) = \int_\Omega [\frac{(\nabla \times \vec{E}) \cdot (\nabla \times \vec{E}^*)}{\mu_r} - k_0^2 \epsilon_c \vec{E} \cdot \vec{E}^*] d\Omega \tag{3.3}$$

where Ω is the bounded region.

In order to find the variation of F^d, a differential $\vec{u^*}$ is introduced into the variational parameter $\vec{E}^*$:

$$\vec{E}^{*'} = \vec{E}^* + \vec{u^*} \tag{3.4}$$

The variation of F^d is defined as:

$$\delta F^d = F^d(\vec{E}^{*'}) - F^d(\vec{E}^*) \tag{3.5}$$

Substitution of (3.3) into (3.5) and using (3.4) yields

$$\delta F^d = \int_\Omega [\frac{(\nabla \times \vec{E}) \cdot (\nabla \times \vec{u^*})}{\mu_r} - k_0^2 \epsilon_c \vec{E} \cdot \vec{u^*}] \, d\Omega \tag{3.6}$$

Using the vector identity $\nabla \cdot (\vec{A} \times \vec{B}) = \vec{B} \cdot (\nabla \times \vec{A}) - \vec{A} \cdot (\nabla \times \vec{B})$, equation (3.6) may be written as

$$\delta F^d = \int_\Omega [\{\nabla \times \frac{(\nabla \times \vec{E})}{\mu_r} - k_0^2 \epsilon_c \vec{E}\} \cdot \vec{u^*} - \nabla \cdot (\frac{(\nabla \times \vec{E})}{\mu_r} \times \vec{u^*})] d\Omega \qquad (3.7)$$

The first integrand vanishes by virtue of the vector wave equation (3.1), and the variation reduces to

$$\delta F^d = - \int_\Omega \nabla \cdot (\frac{(\nabla \times \vec{E})}{\mu_r} \times \vec{u^*}) d\Omega \qquad (3.8)$$

Applying the divergence theorem, this equation becomes

$$\delta F^d = - \int_S (\frac{(\nabla \times \vec{E})}{\mu_r} \times \vec{u^*}) \cdot \hat{n}\, dS \qquad (3.9)$$

where, $\hat{n}$ is the unit outward normal vector to the surface S.

Using Maxwell's curl equation, (3.9) may be written as

$$\delta F^d = -j\omega\mu_0 \int_S (\vec{u^*} \times \vec{H}) \cdot \hat{n} dS \qquad (3.10)$$

For bounded problems, the electric field is known in advance on the boundary S, and consequently $\vec{u^*}$ vanishes since the electric field is not a variational parameter on the boundary. As a result the variation, see equation (3.10), vanishes. This is not the case for unbounded problems since the electric field is not known on part or all the boundary, and hence $\vec{u^*}$ is not zero. From that, it is obvious that an extra term must be added to the functional of equation (3.3). This term corresponds to the variation:

$$\delta F^b = j\omega\mu_0 \int_S (\vec{u^*} \times \vec{H}) \cdot \hat{n}\, dS \qquad (3.11)$$

By inspection, this variation corresponds to the following boundary integral denoted here by F^b

$$F^b(\vec{E^*}) = j\omega\mu_0 \int_S \vec{E^*} \times \vec{H} \cdot \hat{n}\, dS \qquad (3.12)$$

From this result, the functional for unbounded problems is the sum of the integrals of equations (3.3) and (3.12):

$$F(\vec{E^*}) = \int_\Omega [\frac{(\nabla \times \vec{E}) \cdot (\nabla \times \vec{E^*})}{\mu_r} - k_0^2 \epsilon_c \vec{E} \cdot \vec{E^*}] d\Omega + j\omega\mu_0 \int_S \vec{E^*} \times \vec{H} \cdot \hat{n}\, dS \qquad (3.13)$$

It is worth noting that the functional (represents the peak power, and in order to represent the average power it must be multiplied by a constant factor of $\frac{1}{2}$) for unbounded problems , derived here, is identical to the energy balance equation obtained via Galerkin method [78], with the divergence term set to zero since the edge based-finite element method is used here wherein the condition on the normal component is automatically satisfied. This agreement is a consequence of the equivalence between Galerkin technique and the variational principle. In contrast to that, the functional given by [37], [53], and [54] differs from the energy balance equation derived in [78].

The domain integral (over the domain Ω) in (3.13) is identical to the functional given in [75]. Therefore, the solution for the bounded domain is extracted from [75]. On the other hand, the boundary integral (over the truncating boundary S) in (3.13) involves both electric and magnetic fields. Thus, another equation is needed in order to eliminate the magnetic field. This equation may be obtained from the solution of the unbounded domain.

3.4 The Exterior Domain

The scattered electric field in this region is described by the asymptotic expansion:

$$\vec{E}^s = \frac{e^{-jk_1\rho}}{\sqrt{\rho}} \Sigma_{m=0}^{\infty} \frac{\bar{E}_m(\phi)}{\rho^m} \tag{3.14}$$

where, (ρ, ϕ, z) are the cylindrical coordinates, and k_1 is the wave number of the unbounded region. The transverse electric (TE) illumination is considered since it is more important than the transverse magnetic (TM) excitation [76]. However, the analysis of the TM case is similar.

The scattered magnetic field is found, below, by expressing the curl of the scattered electric field in terms of the scattered magnetic field via Maxwell's equation, and in terms of the scattered electric field upon using the asymptotic expansion. These two quantities, representing the curl, are then equated.

It is obvious that the scattered fields obey Maxwell's equations. From Maxwell's curl equation, the $z-$component is

$$\hat{z}\cdot(\nabla\times\vec{E}^s)=-j\omega\mu_1(\hat{z}\cdot\vec{H}^s) \tag{3.15}$$

Expressing the curl in cylindrical coordinates leads to

$$\hat{z}\cdot(\nabla\times\vec{E}^s)=\frac{1}{\rho}\frac{\partial}{\partial\rho}(\rho\hat{\phi}\cdot\vec{E}^s)-\frac{1}{\rho}\frac{\partial}{\partial\phi}(\hat{\rho}\cdot\vec{E}^s) \tag{3.16}$$

The azimuthal component $\hat{\phi}\cdot\vec{E}^s$ and the radial component $\hat{\rho}\cdot\vec{E}^s$ may be obtained from the asymptotic expansion (3.14), namely

$$\hat{\phi}\cdot\vec{E}^s=\frac{e^{-jk_1\rho}}{\sqrt{\rho}}\Sigma_{m=0}^{\infty}\frac{\hat{\phi}\cdot\vec{E}_m(\phi)}{\rho^m},\ \hat{\rho}\cdot\vec{E}^s=\frac{e^{-jk_1\rho}}{\sqrt{\rho}}\Sigma_{m=0}^{\infty}\frac{\hat{\rho}\cdot\vec{E}_m(\phi)}{\rho^m} \tag{3.17}$$

Substituting (3.17) into (3.16) yields

$$\hat{z}\cdot(\nabla\times\vec{E}^s)=\frac{e^{-jk_1\rho}}{\sqrt{\rho}}\left[\frac{1}{\rho}\Sigma_{m=0}^{\infty}\frac{(\frac{1}{2}-jk_1\rho)\{\hat{\phi}\cdot\vec{E}_m\}-\frac{\partial}{\partial\phi}\{\hat{\rho}\cdot\vec{E}_m\}}{\rho^m}-\frac{1}{\rho^2}\Sigma_{m=0}^{\infty}\frac{(m+1)\{\hat{\phi}\cdot\vec{E}_{m+1}\}}{\rho^m}\right] \tag{3.18}$$

The second sum is a higher order quantity, and upon the first order approximation this equation gives

$$\hat{z}\cdot(\nabla\times\vec{E}^s)=\frac{e^{-jk_1\rho}}{\sqrt{\rho}}\left[\Sigma_{m=0}^{\infty}\frac{(\frac{1}{2\rho}-jk_1)\{\hat{\phi}\cdot\vec{E}_m(\phi)\}-\frac{1}{\rho}\frac{\partial}{\partial\phi}\{\hat{\rho}\cdot\vec{E}_m(\phi)\}}{\rho^m}\right] \tag{3.19}$$

Considering the smooth nature of the scattered fields [79], the second term is discarded, and one obtains

$$\hat{z}\cdot(\nabla\times\vec{E}^s)=\frac{e^{-jk_1\rho}}{\sqrt{\rho}}\left[\frac{1}{\rho}\Sigma_{m=0}^{\infty}\frac{(\frac{1}{2}-jk_1\rho)\{\hat{\phi}\cdot\vec{E}_m(\phi)\}}{\rho^m}\right] \tag{3.20}$$

Comparing with (3.14), this equation leads to

$$\hat{z}\cdot(\nabla\times\vec{E}^s)=(\frac{1}{2\rho}-jk_1)(\hat{\phi}\cdot\vec{E}^s) \tag{3.21}$$

Substitution of (3.21) into (3.15) gives the desired relation, namely

$$\vec{H}^s\cdot\hat{z}=\frac{\vec{E}^s\cdot\hat{\phi}}{Z_1},\qquad Z_1=\frac{2j\eta_1k_1\rho}{2jk_1\rho-1} \tag{3.22}$$

in which η indicates the intrinsic impedance, and the subscript 1 refers to the unbounded medium.

3.5 The Continuity Conditions

The solutions in the bounded and exterior domains are combined by enforcing the continuity of the fields on S. In other words, the field components in the boundary integral of equation (3.13) can be replaced by those obtained from the solution of the exterior domain. Further, the total field in the boundary integral F^b can be decomposed into the incident and scattered components as follows:

$$F^b = j\omega\mu_0 \int_S (\bar{E}^* \times \bar{H}) \cdot \hat{n}\, dS = j\omega\mu_0 \int_S [(\bar{E}^{s^*} + \bar{E}^{i^*}) \times (\bar{H}^s + \bar{H}^i)] \cdot \hat{n}\, dS \qquad (3.23)$$

where $\hat{n}$ is now the outward unit normal to S with respect to the exterior region (sine these fields are in the exterior region), or the inward unit normal with respect to Ω as depicted in Fig. 3.1.

Expanding the integrand and using (3.22) yields the following equation:

$$F^b = j\omega\mu_0 \int_S [\frac{E_t^{s^*} E_t^s}{Z_1} + s\frac{E_t^{s^*} E^i}{\eta_1} + \bar{E}^{i^*} \times (\bar{H}^s + \bar{H}^i) \cdot \hat{n}] dS \qquad (3.24)$$

where, E_t^s is the tangential component to S of the scattered field, η_1 is the intrinsic impedance of the surrounding medium, and $s = sgn(\hat{n} \times \bar{E}^i \cdot \hat{z})$.

It is one of the nice features of using edge elements that only the tangential component of the field need to be considered, since the condition of the normal component is automatically satisfied.

At this stage, the unknown of the boundary integral is the scattered tangential field whereas the unknown of the domain integral (both on S and interior to S) is the total field. Therefore, it is necessary to express the field on S, of the domain integral, in terms of the incident and scattered components. This issue is outlined in Section 3.6. Finally, after edge elements discretization, the unknowns are the scattered tangential field on S and the total tangential field interior to S. This makes this method useful for EMC applications, since both the scattered field (affecting other equipment) and the penetrated field (affecting the victim equipment) can be computed directly.

3.6 Edge Elements Discretization

Since TE excitation is considered (i.e., the electric field vector has no axial component), only three side nodes of the edge element described in [75] are needed. For easy reference, a brief description of the edge element used in this paper to divide the bounded domain is given:

Consider the triangular element shown in Fig. 3.2. The edges are denoted by the numbers 1, 2, and 3. Also, the tangential components of the electric field vector evaluated at the centers of the edges are denoted by E_{t1}, E_{t2}, and E_{t3}, as depicted in Fig. 4.2.

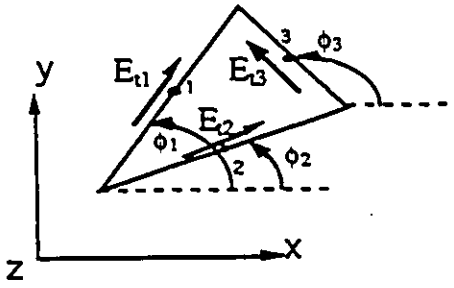

Figure 3.2: Triangular edge element

From simple geometrical considerations, each tangential component can be expressed as follows :

$$E_{ti} = E_{xi}\cos\phi_i + E_{yi}\sin\phi_i, \quad 0 \leq \phi_i < \pi \tag{3.25}$$

where, E_{xi}, and E_{yi} are the $x-$component, and $y-$component of the electric field evaluated at the center of edge i (i=1,2, or 3), and ϕ_i is the azimuthal angle of edge i measured from the positive $x-$axis. Further, the x and y components, within each

element, are expressed by a linear interpolating function of y and x, respectively [75]:

$$E_x = a + cy, \quad E_y = b - cx \tag{3.26}$$

where a, b, and c are constants.

Combining (3.25) and (3.26), E_x and E_y within each triangular element f are written in terms of the tangential components:

$$E_x = [U]^T [E_t]_f, \quad E_y = [V]^T [E_t]_f \tag{3.27}$$

where, the superscript T denotes matrix transpose,

$$[U] = \begin{bmatrix} a_1 + c_1 y \\ a_2 + c_2 y \\ a_3 + c_3 y \end{bmatrix}, \quad [V] = \begin{bmatrix} b_1 - c_1 x \\ b_2 - c_2 x \\ b_3 - c_3 x \end{bmatrix}, \quad [E_t]_f = [E_{t1}\ E_{t2}\ E_{t3}]^T,$$

and a_i, b_i, and c_i ($i = 1,2,$ or 3) are given by [75]:

$$\begin{aligned} a_i &= [(\, y_k \cos\phi_k - x_k \sin\phi_k) \sin\phi_j - (y_j \cos\phi_j - x_j \sin\phi_j) \sin\phi_k]/\Delta \\ b_i &= [(\, y_j \cos\phi_j - x_j \sin\phi_j) \cos\phi_k - (y_k \cos\phi_k - x_k \sin\phi_k) \cos\phi_j]/\Delta \\ c_i &= (\cos\phi_j \sin\phi_k - \cos\phi_k \sin\phi_j)/\Delta \end{aligned}$$

where

$$\Delta = \sum_{i=1}^{3} (y_i \cos\phi_i - x_i \sin\phi_i)\,(\cos\phi_j \sin\phi_k - \cos\phi_k \sin\phi_j),$$

and the subscripts i, j, k progress modulo 3 around the triangle edges.

The edge elements discretization is used to realize the linear system of equations

$$[A][E_t] = [B] \tag{3.28}$$

in which, $[A]$ is a square matrix that involves the shape functions of the triangular edge elements, $[E_t]$ is the global vector containing the edge variables (the tangential components of the field along the triangles edges), and $[B]$ is the excitation vector.

As a consequence of discretizing the bounded domain , the boundary S is represented by straight edges. In addition, the scattered tangential field in (3.24) is expanded in terms of pulse functions:

$$E_t^s = \sum_{e=1}^{M} E_{t,e}^s P_e \tag{3.29}$$

where, P_e is a pulse function (unity at edge e and zero elsewhere), and M is the total number of edges representing S.

Substituting (3.29) into (3.24), and applying the variational principle (3.2) yields:

$$\frac{\partial F^b}{\partial E_{t,e}^s} = j\omega\mu_0[\frac{E_{t,e}^s}{Z_1} + s\frac{E_e^i}{\eta_1}]L_e \tag{3.30}$$

where, L_e is the length of edge e. The term $\frac{j\omega\mu_0}{Z_1}L_e$ is augmented to the main diagonal of the system matrix of equation (3.28), and the term $j\omega\mu_0[s\frac{E_e^i}{\eta_1}]L_e$ is augmented to the excitation vector of (3.28). Further, the field on S, of the domain integral, is expressed in terms of the incident and scattered components, and then the excitation term is augmented to the excitation vector. To illustrate the idea, consider a triangle with an edge residing on the truncating boundary S, say edge i, as depicted in Fig. 3.3.

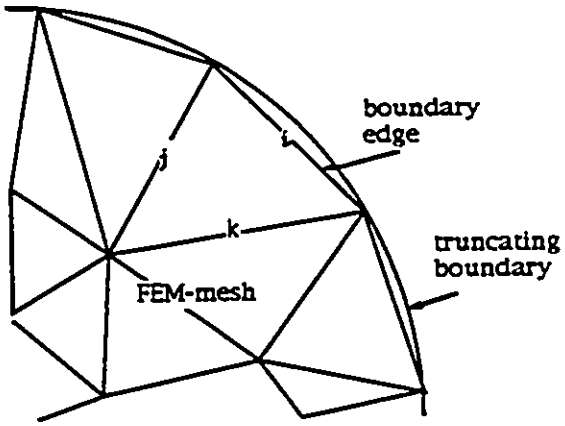

Figure 3.3: A boundary edge

The element matrix for this triangle contributes the following quantities, corresponding to edge i

$$A_{ii}E_{t,i},\ A_{ji}E_{t,i},\ A_{k,i}E_{t,i}$$

where A_{ii}, A_{ji}, and A_{ki} are system matrix entries, and $E_{t,i}$ is the tangential component of the field at the center of edge i. The tangential field $E_{t,i}$ can be expressed as the sum of the incident and scattered components

$$E_{t,i} = E^s_{t,i} + E^i_{t,i}$$

where the superscripts s, and i refer to the scattered and incident field components, respectively. Thus each boundary edge contributes an extra three terms to the excitation vector

$$\begin{aligned} line\ i \rightarrow &\quad -A_{ii}E^i_{t,i} \\ line\ j \rightarrow &\quad -A_{ji}E^i_{t,i} \\ line\ k \rightarrow &\quad -A_{ki}E^i_{t,i} \end{aligned}$$

The resulting system of equations, after augmenting both the system matrix and the excitation vector of (3.28), is solved for the edge variables from which the field components can be computed via the interpolating functions.

3.7 Numerical Results

The transition between the near field region and the far field region is at $\frac{\lambda}{2\pi}$ from the source point [80]. Since the sources for the scattered fields are the equivalent currents on the surface of equipment structure, then the transition region is at $\frac{\lambda}{2\pi}$ from the surface of equipment. As a matter of fact, it is found for all the results, that $\frac{\lambda}{3}$ from the structure surface is sufficient to obtain stable and reliable results. Aiso, coarse mesh can be used in the less exposed parts of the structure, and in the air outside the structure [81]. Lastly, since the matrix obtained is sparse and symmetric, efficient iterative methods can be used. These aspects are expected to reduce computer storage requirement, and enable the method to handle relatively large structures compared to the wave length.

The solution is applied to the following problems in order to demonstrate its validity and effectiveness. The surrounding medium in all cases is free space.

A. One-Dimensional Example:

Infinite Plane Shield

Consider the infinite plane shield shown in Fig. 3.4 (see the insert) where the incident electric field is unity at $x = 0$. Since the scattered field is a plane wave, the truncating boundary is placed right on the surface of the shield, and $Z1$ in (3.22) is replaced by η_0. Using 22 elements, the computed field compares very well with the analytical solution as can be seen in Fig. 3.4.

B. Two-Dimensional Example:

A Square Metal Shield with an Aperture

The shielding enclosure depicted in Fig. 3.5 (see the insert) is a victim of plane wave illumination with phase center at $x = -11cm$. The metal is assumed to be perfectly conducting because the shielding effectiveness is primarily determined by the leakage through apertures and holes and not by the diffusion through the shield material [80].

A square truncating boundary, conforming with the shielding enclosure, is used to reduce the number of unknowns, and $Z1$ is again replaced by η_0 in (3.22). Further, the problem domain is discretized into a uniform mesh with $1cm$ step. Shown in Fig. 3.6 is E_y vs. the $x-$coordinate inside the shield for different excitation frequencies. Note that the field amplitude at the center of the shield is highest at the resonant frequency ($f = 1.5GHz$). Also, it is well known that the field is enhanced near apertures [82]. This is indeed what these computations show.

C. Two-Dimensional Example:

Scattering Cross Section of Dielectric Cylinders

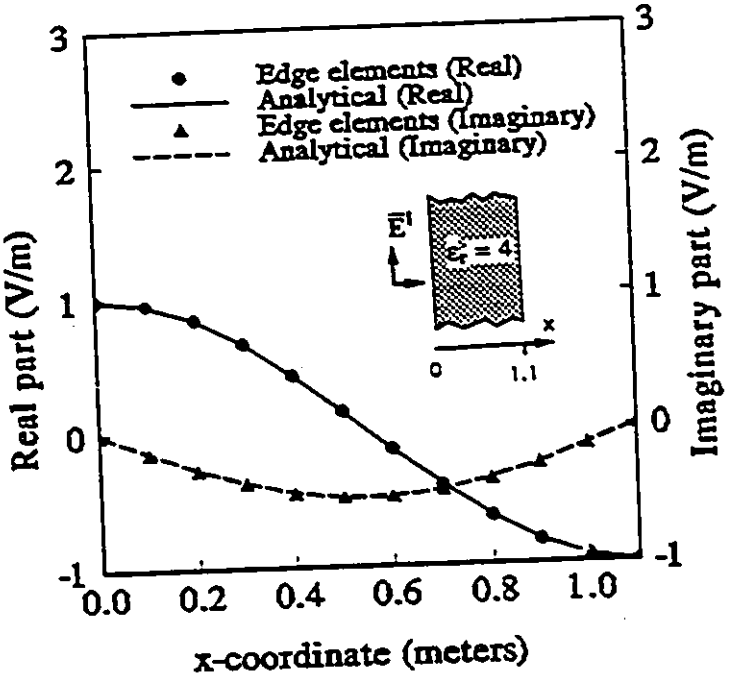

Figure 3.4: Electric field (V/m) inside the infinite plane shield at frequency of 68.2 MHz.

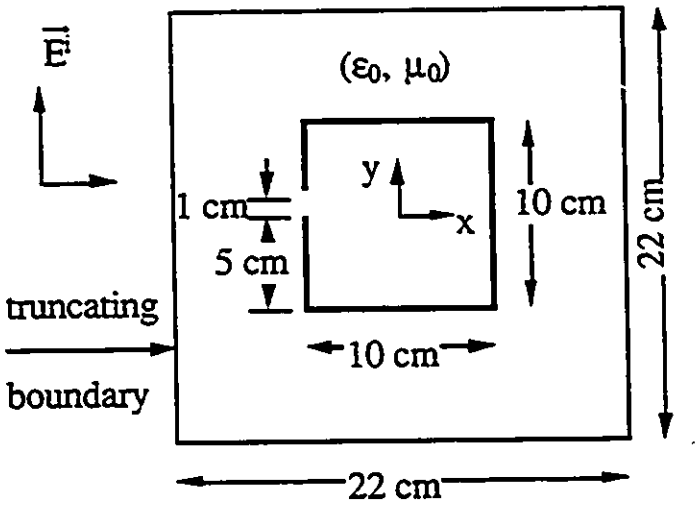

Figure 3.5: Metal shield with an aperture

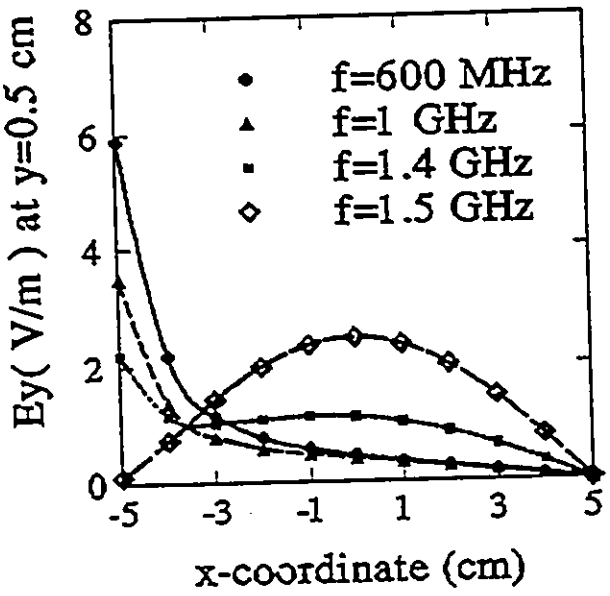

Figure 3.6: Ey (V/m) inside the shielding enclosure (Fig. 3.5) along a line passing through aperture centre.

The bistatic scattering cross section (RCS) of $2D$ structures is defined as:

$$RCS = \lim_{\rho \to \infty} 2\pi\rho \frac{|\vec{E}^s|^2}{|\vec{E}^i|^2} \tag{3.31}$$

in which, $\lim_{\rho \to \infty}$ refers to the far field region. However, as explained at the beginning of this section, a distance of $\frac{\lambda}{3}$ from the surface of the structure is adequate for the field to be considered in the far region.

In the following, the RCS of four different dielectric cylinders are computed and compared to published data. The excitation is a plane wave with a frequency of $300MHz$ and phase center at the coordinates origin. Further, the problem domain in each case is discretized into circular concentric layers of elements. Because of symmetry, only half the structure is considered. The computations are performed on a Dec Station 3100 ($16Mb$ RAM).

1. Homogeneous Circular Cylinder:

Consider the off-centered cylinder depicted in Fig. 3.7(a) (see the insert). The dielectric region is discretized into five uniform layers of elements, and the free space region, between the cylinder surface and the truncating boundary (placed at 0.32λ from cylinder surface), into four uniform layers. The matrix obtained is 0.49% full, the number of unknowns 495, and CPU time $118s$. In Fig. 3.7(a), the present solution (solid circles) is compared to the MoM/FEM (Method of Moments/FEM [49]) solution (continuous line). The comparison reveals good agreement between the two solutions.

2. Layered Circular Cylinder:

The geometry of the cylinder is shown in Fig. 3.7(b) (see the insert). The cylinder is discretized into a non-uniform mesh where the innermost layer is divided into only three elements ($0.42\lambda_\epsilon$ resolution), and each of the other layers into one layer of elements. Also, the free space region is divided into four layers of thicknesses, starting from the cylinder surface: $0.05\lambda_0$, $0.075\lambda_0$, $0.1\lambda_0$, $0.095\lambda_0$, respectively. The matrix obtained is 0.823% full, the number of unknowns 292, and CPU time $43s$. As a matter of

Figure 3.7: Computed bistatic scattering cross section (RCS) of dielectric cylinders (cases (a), (b), (c), and (d)) as compared to MoM/FEM, and Richmond's solution at f = 300 MHz

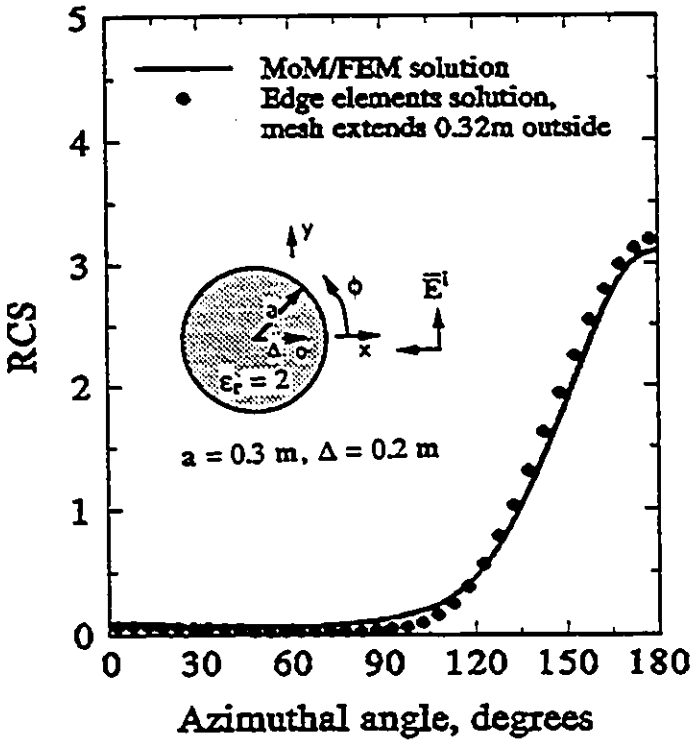

Figure 3.7: (a) homogeneous circular cylinder

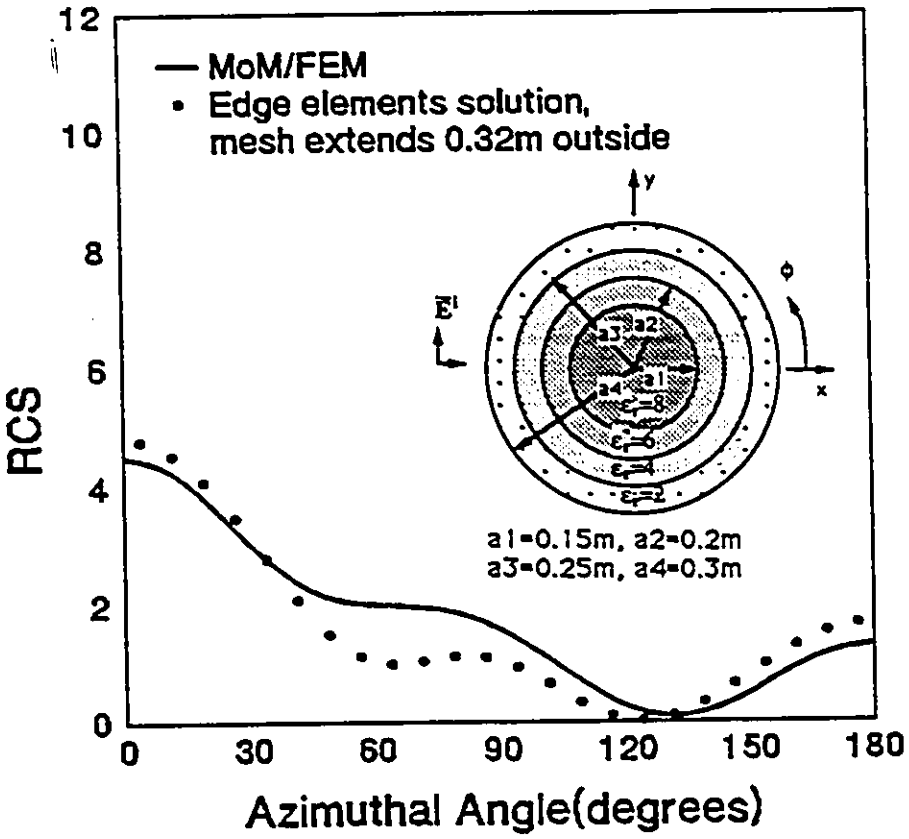

Figure 3.7: (b) layered circular cylinder

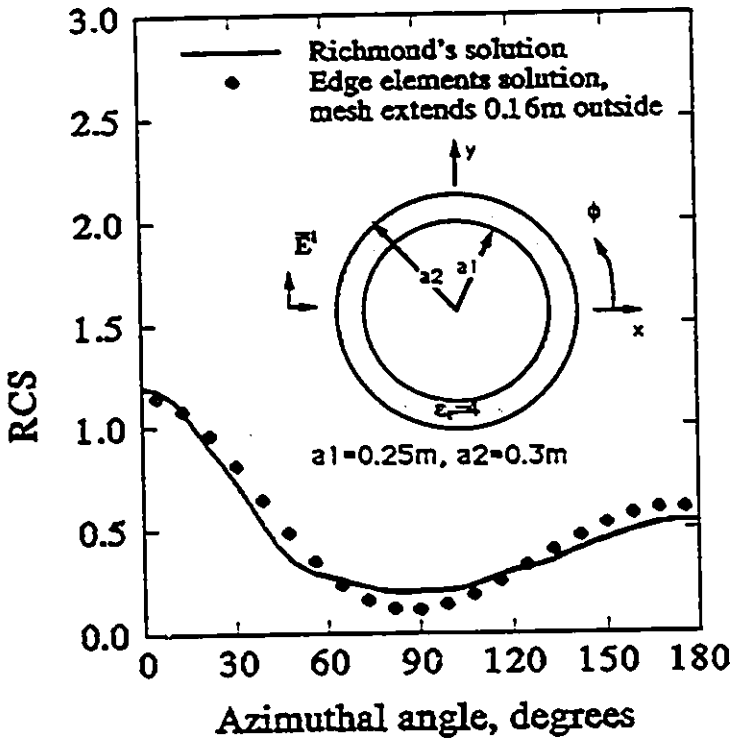

Figure 3.7: (c) homogeneous circular shell

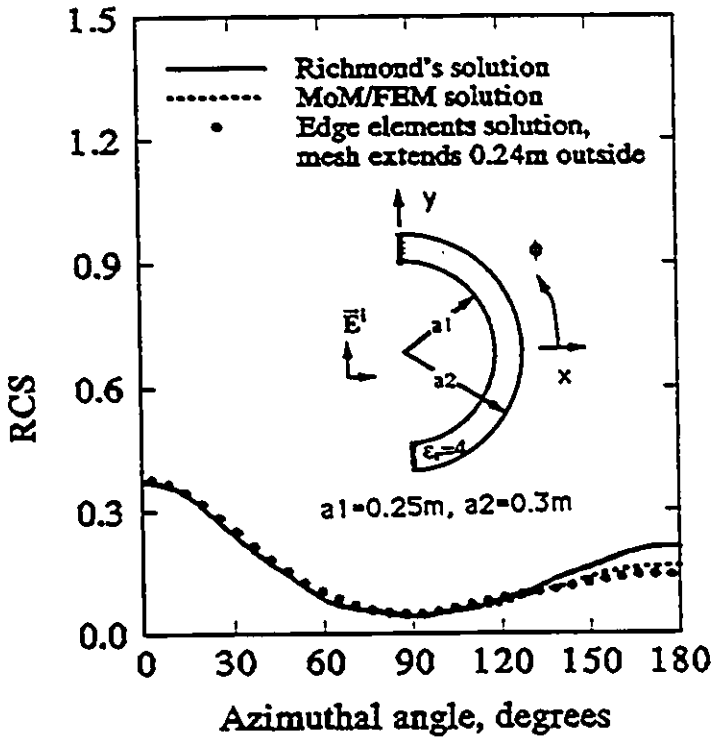

Figure 3.7: (d) homogeneous semi-circular shell

fact, a uniform fine mesh was employed, and it gives almost the same solution as the non-uniform mesh. Thus, a coarse mesh in the less exposed parts of the structure reduces the storage requirement and CPU time, and yet does not degrade the quality of the solution in the region of interest. The agreement between this solution and the MoM/FEM solution [49] is acceptible, as shown in Fig. 3.7(b). It is worth noting that the MoM/FEM solution is in terms of the axial magnetic field for the TE excitation while the present solution is in terms of the transverse electric field for the TE case.

3. Homogeneous Circular Shell:

The cylindrical shell is shown in Fig. 3.7(c) (see the insert). The free space inside the shell is discretized into four uniform layers of elements, the dielectric into one layer, and the free space outside the shell into two uniform layers. The matrix is 1.067% full, the number of unknowns 224, and CPU time 16*s*. This solution compares well with Richmond's solution [83] as can be seen in Fig. 3.7(c).

4. Homogeneous Semi-Circular Shell:

The discretization scheme for this case is similar to that used for the circular shell. The resulting matrix is 0.617% full, the number of unknowns 392, and CPU time 65*s*. This solution compares very well with the MoM/FEM solution [49], and has acceptible agreement with Richmond's solution [83], as shown in Fig. 3.7(d).

3.8 CONCLUSIONS

A numerical solution to the electromagnetic interference problem is presented. The source of interference is a plane wave. The solution utilizes the edge elements which are usually free from the adverse effects of spurious modes. Also, sharp points and edges can be modeled without the need for special singular trial functions. The solution preserves the sparsity and symmetry of the finite element matrix, and thus efficient iterative algorithms can be used. Numerical results are presented that show the validity of the method.

Chapter 4

Edge-Elements Characterization of Radiation and Cross-Talk on Printed Circuit Boards

The edge based finite element method (edge elements) is used to obtain a numerical solution for the radiated emissions and cross talk voltages on printed circuit boards (PCB). Both shielded and open PCB, over a wide frequency range, are analyzed and compared.

The method of analysis is two dimensional, and has the expected advantages of edge elements, namely, not producing spurious solutions, and modeling sharp points and edges without any need for special singular trial functions. Further, the matrix obtained is sparse and symmetric, and the solution can be obtained directly; no need for matrix inversion.

4.1 Introduction

THE actual circuit package can be modelled by a metal shielding enclosure. This shield minimizes the possible external electromagnetic interference. Incidentally, the shield may enhance the intra-system interference. This happens if one of the input

signal harmonics corresponds to a natural frequency of the circuit package (note that high speed digital signals can be represented by the fundamental frequency and its significant harmonics). In such situation the induced voltages on the board tracks are greatly enhanced causing the circuit to malfunction (these unwanted induced voltages are denoted by cross talk). This phenomenon is demonstrated in this Chapter by numerically computing the cross talk levels, over a wide frequency range, for shielded and open circuits. It is found that the latter does not exhibit the resonance behavior.

This leads to the conclusion that the significant harmonics of the input digital signal must not correspond to any of the natural frequencies of the package. Regardless to say that this can be accomplished, for example, by modifying the shape or/and the rise time of the input signal, or even changing the dimensions of the enclosure if possible.

The Chapter is organized as follows: in Section 4.2, applying the edge elements for open boundary problems is outlined. Next, the variational formulation is presented in Section 4.3. Further, using the edge elements for bounded problems is discussed in Section 4.4, and discretizing the resulting integral equation is clarified in Section 4.5. Afterwards, the numerical results are analyzed in Section 4.6. Finally, the conclusion can be found in Section 4.7.

4.2 Open Boundary Problems

The edge elements - scattering amplitude combination proposed in in Chap. 3 is used in this Chapter. It is worth to mention that this combination is intended for scattering applications. In this Chapter, the sources are the signals on the PCB (radiation problem). Thus, the main steps needed to apply the combination for radiation problems are illustrated below.

Consider a PCB modelled by an inhomogeneity as in Fig. 4.1. The inhomogeneity is described by permittivity ϵ, conductivity σ, and permeability μ. The artificial

truncating boundary S is introduced to allow the modelling of the infinite space on a computer with limited memory.

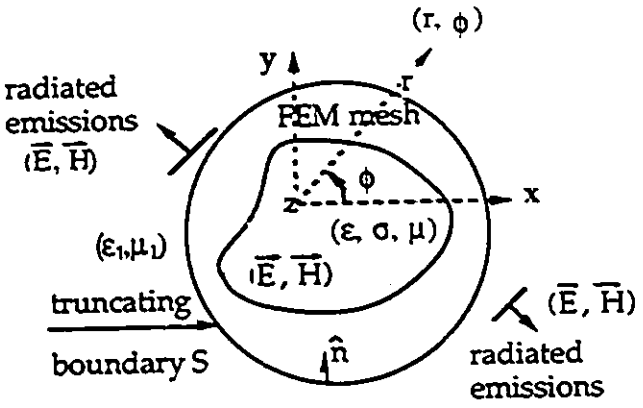

Figure 4.1: General open printed circuit board representation.

The objective is to compute the fields inside the truncating boundary, from which the voltages are obtained by the line integral

$$V_{ij} = -\int_i^j \vec{E} \cdot d\vec{l} \tag{4.1}$$

where l is the path of integration between the points i and j. This integral is easily computed with edge elements since the solution is in terms of the tangential components of the field along the elements edges.

4.3 ANALYSIS

The functional F is given by, refer to Chap. 3:

$$F(\vec{E}^*) = \int_\Omega [\frac{(\nabla \times \vec{E}) \cdot (\nabla \times \vec{E}^*)}{\mu_r} - k_0^2 \epsilon_c \vec{E} \cdot \vec{E}^*] d\Omega$$
$$+ j\omega\mu_0 \int_S \vec{E}^* \times \vec{H} \cdot \hat{n} dS \tag{4.2}$$

in which, $*$ denotes the complex conjugate, k_0 the free space wave number, μ_r the relative permeability, and $\epsilon_c = \epsilon_r - j\frac{\sigma}{\omega\epsilon_0}$, where, ϵ_r is the relative permittivity, and ω is the radian frequency. Also, Ω is the domain enclosed by the truncating boundary S, and $\hat{n}$ is the unit inward normal vector at S, as depicted in Fig. 4.1.

The domain integral of (4.2) is identical to that given by [75], and therefore their edge element is adopted. In addition, the boundary integral of (4.2) involves both electric and magnetic fields. To eliminate the magnetic field, an additional relation is needed between the electric and magnetic field. This relation can be obtained from the solution in the region outside the truncating boundary.

The radiated emissions outside S are described by the asymptotic expansion:

$$\bar{E} = \frac{e^{-jk_1\rho}}{\sqrt{\rho}} \sum_0^\infty \frac{\bar{E}_m(\phi)}{\rho^m} \tag{4.3}$$

where, (ρ, ϕ, z): the cylindrical coordinates, $\hat{\phi}$: unit vector, k_1: the wave number of the unbounded region.

Using (4.3), it can be shown, via Maxwell's curl equation, that the radiated magnetic field is given by the following relation:

$$\bar{H} \cdot \hat{z} = \frac{\bar{E} \cdot \hat{\phi}}{Z_1}, \qquad Z_1 = \frac{2j\eta_1 k_1 \rho}{2jk_1\rho - 1} \tag{4.4}$$

in which, η is the intrinsic impedance, and the subscript 1 refers to the unbounded medium.

Substituting this relation into the boundary integral F^b of (4.2) yields:

$$F^b = j\omega\mu_0 \int_S [\frac{E_t^* E_t}{Z_1}] dS \tag{4.5}$$

where E_t is the tangential component of the radiated field at S.

4.4 Bounded Problems

For bounded problems, the tangential component of the electric field on the boundary is known. Consequently, the boundary integral of (4.2) vanishes as E is no more variational parameter on the boundary.

4.5 Discretization

The discretization of the domain integral is as given by [75], with the axial propagation phase constant β set to zero since only the transverse characteristics are investigated; β vanishes at the cutoff frequencies and furthermore the mode pattern is frequency invariant. Thus, only three side nodes of the edge element described by [75] are needed. For easy reference, a brief description of the edge element used in this Chapter to divide the bounded domain is given:

Consider the triangular element shown in Fig. 4.2. The edges are denoted by the numbers 1, 2, and 3. Also, the tangential components of the electric field vector evaluated at the centers of the edges are denoted by E_{t1}, E_{t2}, and E_{t3}, as depicted in Fig. 4.2.

From simple geometrical considerations, each tangential component can be expressed as follows :

$$E_{ti} = E_{xi}\cos\phi_i + E_{yi}\sin\phi_i, \quad 0 \leq \phi_i < \pi \tag{4.6}$$

where, E_{xi}, and E_{yi} are the $x-$component, and $y-$component of the electric field evaluated at the center of edge i (i=1,2, or 3), and ϕ_i is the azimutnal angle of edge i measured from the positive $x-$axis. Further, the x and y components, within each element, are expressed by a linear interpolating function of y and x, respectively, refer to [75]:

$$E_x = a + cy, \quad E_y = b - cx \tag{4.7}$$

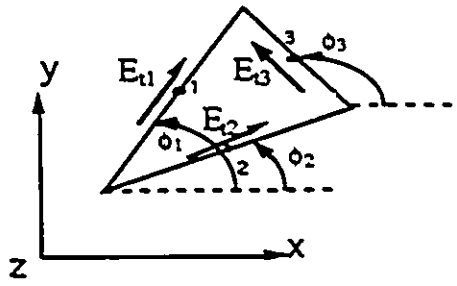

Figure 4.2: Triangular edge element

where a, b, and c are constants.

Combining (4.6) and (4.7), E_x and E_y within each triangular element f are written in terms of the tangential components:

$$E_x = [U]^T [E_t]_f, \quad E_y = [V]^T [E_t]_f \tag{4.8}$$

where, the superscript T denotes matrix transpose,

$$[U] = \begin{bmatrix} a_1 + c_1 y \\ a_2 + c_2 y \\ a_3 + c_3 y \end{bmatrix}, \quad [V] = \begin{bmatrix} b_1 - c_1 x \\ b_2 - c_2 x \\ b_3 - c_3 x \end{bmatrix}, \quad [E_t]_f = [E_{t1}\ E_{t2}\ E_{t3}]^T,$$

and a_i, b_i, and c_i (i = 1,2, or 3) are given by [75]:

$$\begin{aligned} a_i &= [(\, y_k \cos\phi_k - x_k \sin\phi_k) \sin\phi_j - (y_j \cos\phi_j - x_j \sin\phi_j) \sin\phi_k]/\Delta \\ b_i &= [(\, y_j \cos\phi_j - x_j \sin\phi_j) \cos\phi_k - (y_k \cos\phi_k - x_k \sin\phi_k) \cos\phi_j]/\Delta \\ c_i &= (\cos\phi_j \sin\phi_k - \cos\phi_k \sin\phi_j)/\Delta \end{aligned}$$

where

$$\Delta = \sum_{i=1}^{3} (y_i \cos\phi_i - x_i \sin\phi_i)\,(\cos\phi_j \sin\phi_k - \cos\phi_k \sin\phi_j),$$

and the subscripts i, j, k progress modulo 3 around the triangle edges.

The edge elements discretization is used to realize the linear system of equations

$$[A][E_t] = [B] \tag{4.9}$$

in which, $[A]$ is a square matrix that involves the shape functions of the triangular edge elements, $[E_t]$ is the global vector containing the edge variables (the tangential components of the field along the triangles edges), and $[B]$ is the excitation vector.

In consequence of discretizing the bounded domain , the boundary S is represented by straight edges. In addition, the radiated field E is expanded in terms of pulse functions :

$$E_t = \sum_{e=1}^{M} E_e P_e \tag{4.10}$$

where, P_e is a pulse function; unity over the boundary segment e and zero elsewhere, M is the total number of boundary segments, and E_e is the tangential component of the electric field at the center of segment e.

Substituting (4.10) into (4.5), and evaluating the integral, yields:

$$F^b = j\omega\mu_0 \sum_{e=1}^{M} (\frac{E_e^* E_e}{Z_1}) L_e \tag{4.11}$$

where, L_e is the boundary segment length.

To make F stationary, the derivative with respect to E_e^* is performed:

$$\frac{\partial F^b}{\partial E_e^*} = j\omega\mu_0 \frac{E_e}{Z_1} L_e \tag{4.12}$$

Thus, each boundary segment contributes the diagonal term $j\omega\mu_0\frac{L_e}{Z_1}$, through the boundary integral, to the global system of linear equations.

4.6 RESULTS

In order to demonstrate the validity and accuracy of the method, an empty (square 10 by 10 mm) metal enclosure is considered. The metal in all cases is modelled by a

perfect conductor. This approximation is valid since the penetration through the metal is negligible, refer to [S0]. The region enclosed by the shield is divided into a uniform mesh of 1 mm space division. Further, the enclosure is excited by an electric field component imposed as Dirichlet boundary condition (1 V/m) near the shield centre. The computed field level resonates at the cutoff frequencies of the enclosure. These computed cutoff frequencies f_c are compared to the exact values in the following table.

Mode	*Cutoff frequency (GHz)*		%
	exact	computed	error
TE_{10}, TE_{01}	15	14.6625	2.25
TE_{11}	21.2132	21.2165	0.02
TE_{12}, TE_{21}	33.541	33.561	0.06

The reason for that the error being larger at the TE_{10} and TE_{01} modes is that the field pattern has its maximum near the excitation point where the field is forced to have a value of 1 V/m.

Next, an empty (rectangular 20 mm by 2 mm) metal enclosure is considered. The region enclosed by the shield is divided into a uniform mesh of 1 mm space division. Further, the enclosure is excited by an electric field component imposed as Dirichlet boundary condition (1 V/m). The computed field level resonates at the cutoff frequencies of the enclosure. These computed cutoff frequencies f_c are compared to the exact values in the following table.

Mode	*Cutoff frequency (GHz)*		%
	exact	computed	error
$TE_{1,0}$	7.5	7.475	0.3
$TE_{2,0}$	15	14.81	1.3
$TE_{3,0}$	22.5	21.78	3.2

Also, PCB are analyzed, both without metal enclosure as shown in Fig. 4.3, and with metal enclosure as in Fig. 4.4 and Fig. 4.5. It is to be noted that the number

of tracks chosen here is for the matter of convenience. Otherwise, the method can handle arbitrary number of tracks as far as the computer memory requirements are not exceeded.

Presented below are the computed coupling voltages and field patterns of the PCB.

4.6.1 Open PCB Results

The open PCB, see Fig. 4.3, is analyzed. The region defined by the truncating boundary and the ground plane is modelled by a uniform mesh of 2 mm space division; using concentric circles centered at the middle of the ground plane. As a matter of fact, the matrix solved was only 0.53% full. The coupling voltages V_2 and V_3, refer to Fig. 4.6, do not exhibit resonance behavior over the frequency band scanned $(0.1 - 8\ GHz)$. The highest frequency considered in all the computations is determined by the finite discretization; for accurate results the space division must not exceed $\frac{\lambda}{10}$ where λ is the wavelength in the PCB.

Shown in Fig. 4.7 is the radiated electric field in dB at a distance of 19 mm from the coordinates origin. It seems that the radiation is partially blocked by the metal tracks for the angles between $40^o - 90^o$. Also, the plot in Fig. 4.8 shows the radiated field levels in dB, at $f = 5\ GHz$, around the PCB. The highest values are at the source (the right track located at $4 \leq x \leq 6, y = 2\ mm$). The field level declines monotonically with the distance from the source; as expected.

4.6.2 Shielded PCB Results

Nonhomogeneous Dielectric

The shielded PCB with nonhomogeneous dielectric of Fig. 4.4 is excited by a signal of 1 V amplitude on the right track; imposed as Dirichlet boundary condition between

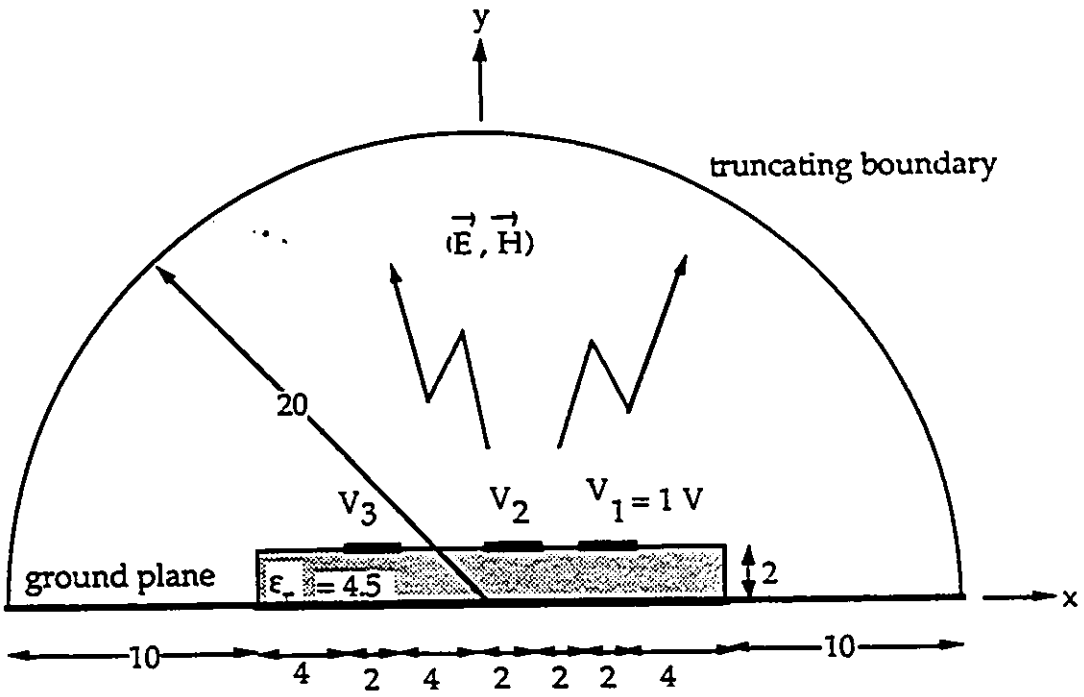

All dimensions are in mm

Figure 4.3: Open printed circuit board.

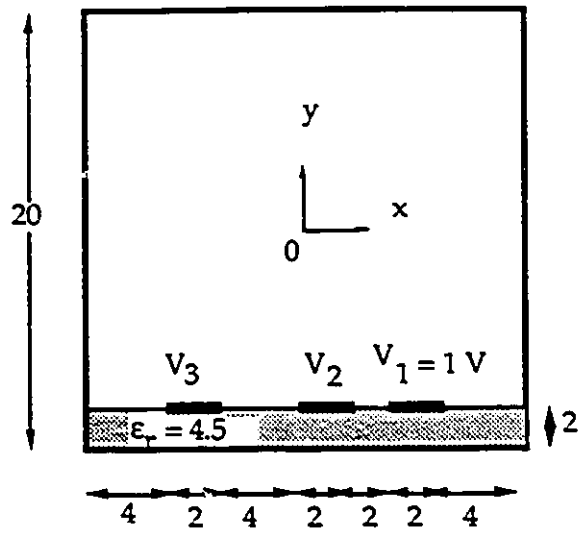

Figure 4.4: Shielded printed circuit board.

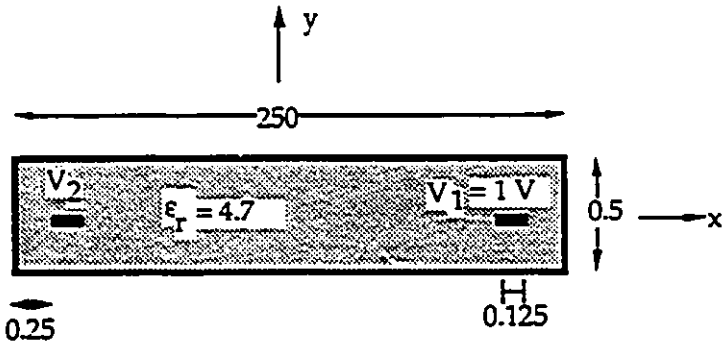

Figure 4.5: Shielded printed circuit board with homogeneous dielectric.

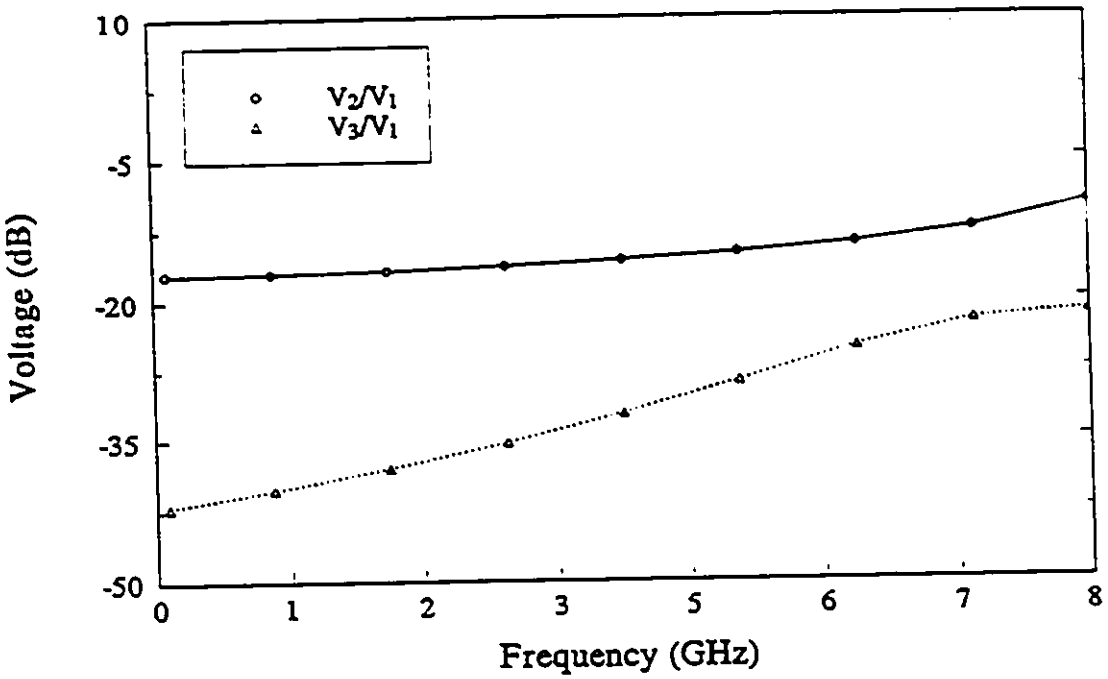

Figure 4.6: Cross talk on the open printed circuit board.

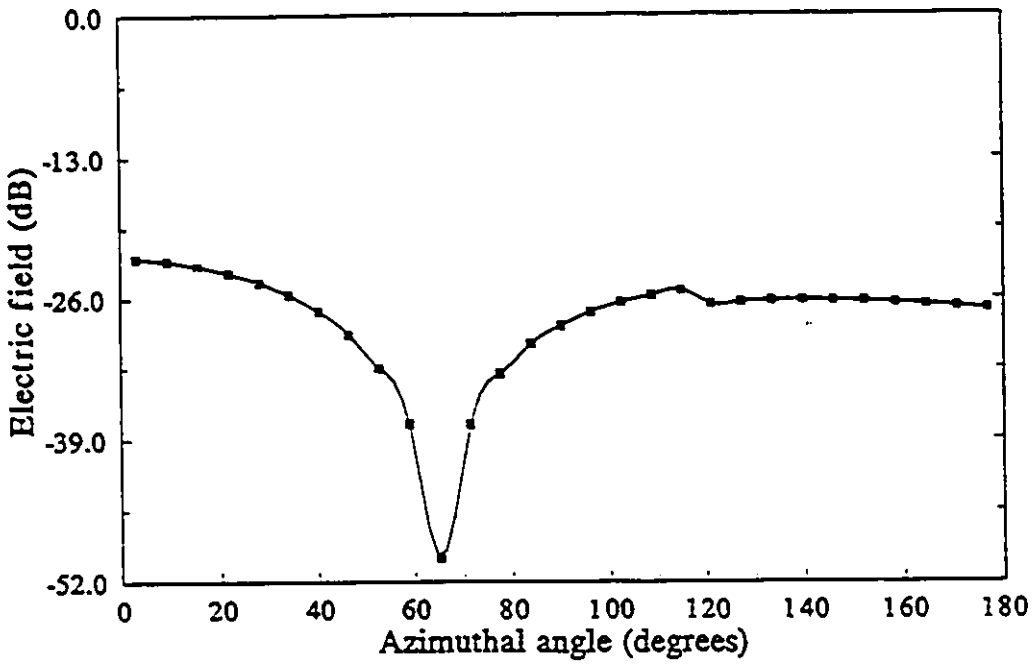

Figure 4.7: Radiated field at 19 mm from the coordinates origin of the open printed circuit board, $f = 5\ GHz$.

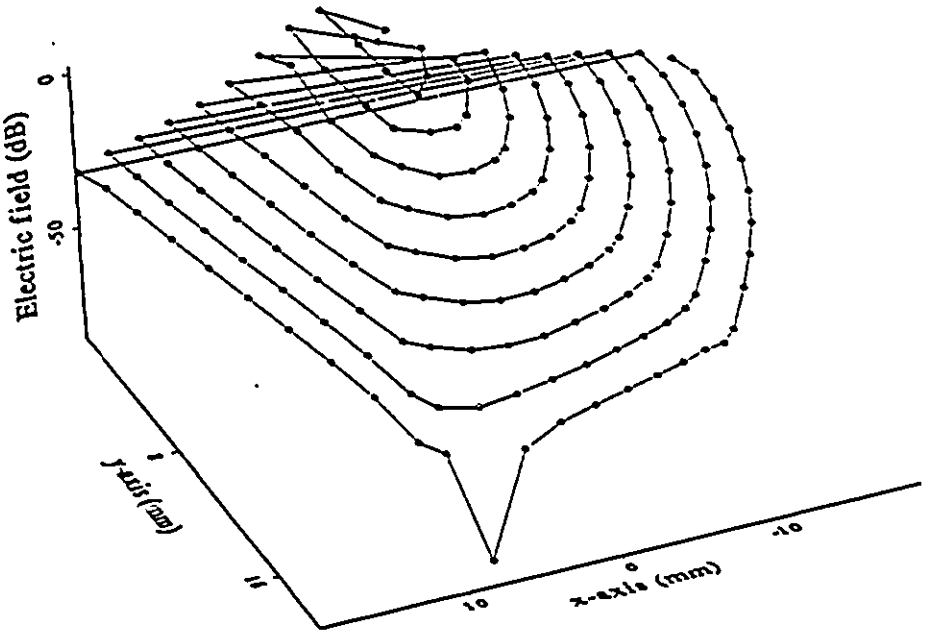

Figure 4.8: Radiated field in dB from the open printed circuit board, $f = 5\ GHz$.

the center of the conductor and the ground plane, namely, $E = 500\ V/m$. The region bounded by the shield is divided into triangles with a uniform space division of 1 mm. The matrix obtained was only 0.21% full. Note that this board is the same as that in Fig. 4.3 but with the shield added.

The induced voltages V_2 and V_3 on the other tracks are monitored, over the frequency band $0.1 - 12\ GHz$, in Fig. 4.9. Two resonances are observed. This confirms that the presence of the enclosure is responsible for the coupling voltages excursions. Shown in the figure also is the computer code execution time. It seems that the matrix obtained is more difficult to solve at the resonance frequencies; more iterations are needed to achieve the same error criterion of 10^{-6}. Also, the field distributions at the resonance frequencies ($f = 6.994,\ 10.7759\ GHz$) are plotted in Fig. 4.10 and 4.11, respectively. The field peaks in the far end of each figure are at the tracks edges (field singularity).

Homogeneous Dielectric

Finally, consider a PCB that consists of two tracks embedded in a homogeneous dielectric slab surrounded by the metal enclosure, as illustrated in Fig. 4.5. The dimensions are chosen to simulate practical PCB configurations. The region inside the enclosure is divided into nonuniform mesh: the horizontal division is $\frac{1}{8}\ mm$ near the tracks (span 1 mm on each side) and 1 mm otherwise, and only two divisions are used in the vertical direction, $\frac{1}{4}\ mm$ each. The right track is excited uniformly by 1 V amplitude; this is justified by the fact that the track width is very small being $\frac{1}{8}\ mm$. In terms of electric field, the excitation is 4000 V/m. The matrix obtained is 0.16% full. Fig. 4.12 reveals the excursions of the left track cross talk voltage V_2. The reason for these excursions is the excitation of the cavity (shield) modes.

The tracks are expected to have only a minor effect on the field distribution inside the enclosure (note that the ratio of track width to enclosure width is 1 : 2000). Thus,

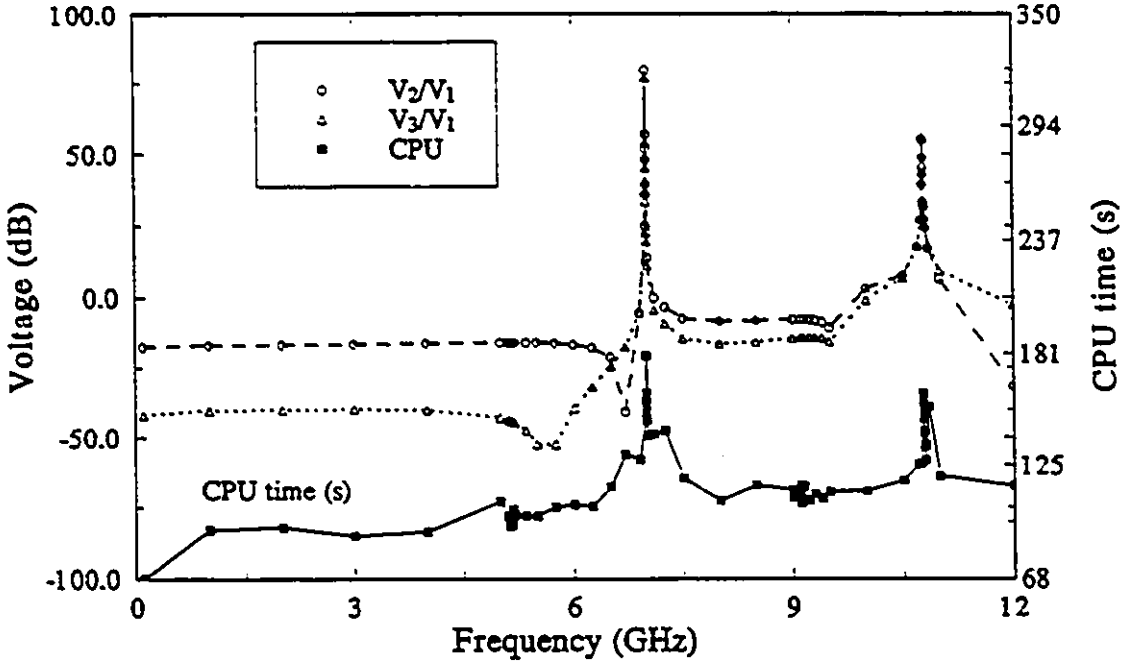

Figure 4.9: Cross talk on the shielded printed circuit board.

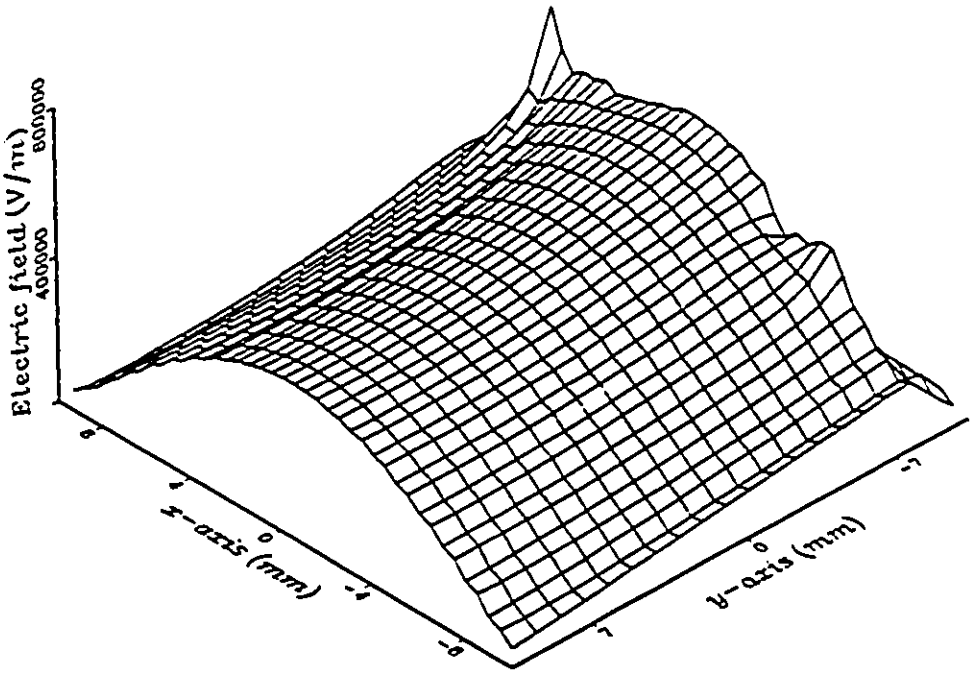

Figure 4.10: Field distribution at the first resonance, $f = 6.994\ GHz$, of the shielded printed circuit board.

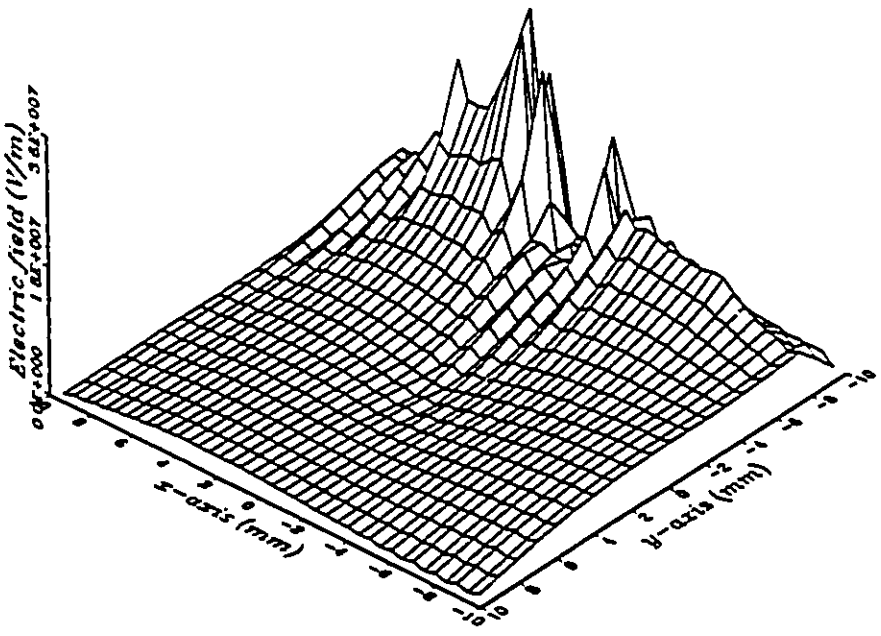

Figure 4.11: Field distribution at the second resonance, $f = 10.7759\ GHz$, of the shielded printed circuit board.

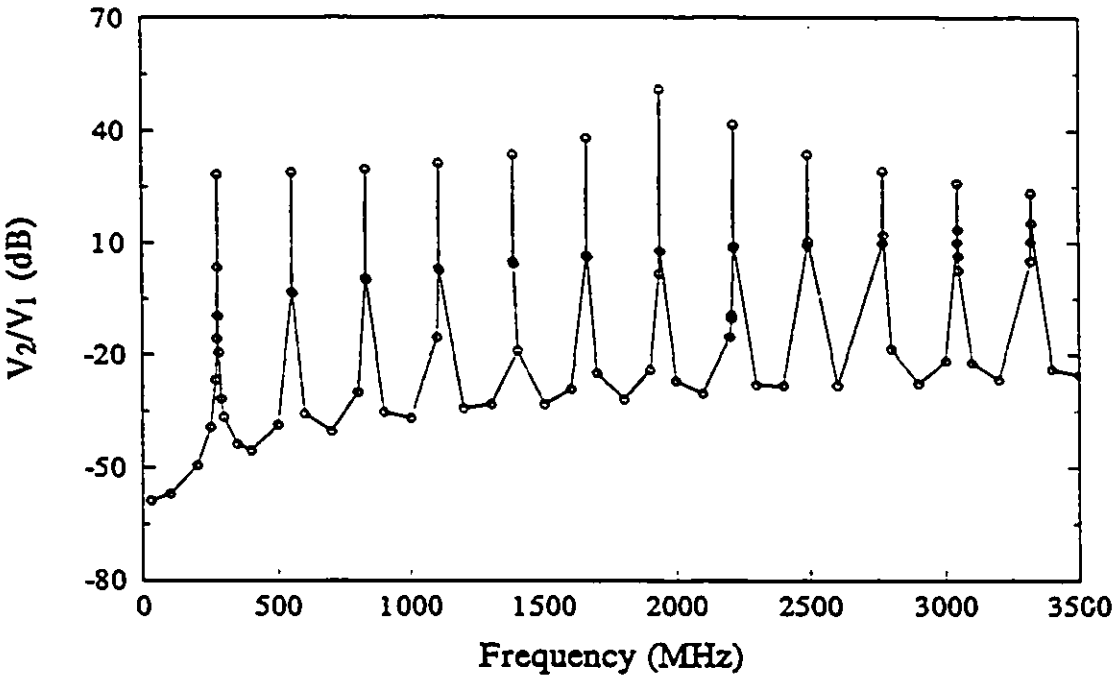

Figure 4.12: Cross talk on the shielded printed circuit board with homogeneous dielectric.

it could be useful to compare the cutoff frequencies f_c with and without tracks. f_c without tracks are expressed as:

$$f_c(TE_{m,o}) = \frac{mc}{2a\sqrt{\epsilon_r}}$$

where c is the speed of light, and a the width of the enclosure. The following table shows that f_c are not effectively disturbed by the presence of the tracks.

Mode	*Cutoff frequency (MHz)*	
	no tracks (exact)	with tracks (computed)
$TE_{1,0}$	277	277
$TE_{2,0}$	554	554
$TE_{3,0}$	830	831
$TE_{4,0}$	1107	1108
$TE_{5,0}$	1384	1385
$TE_{6,0}$	1661	1662
$TE_{7,0}$	1937	1939
$TE_{8,0}$	2214	2216
$TE_{9,0}$	2491	2493
$TE_{10,0}$	2768	2770
$TE_{11,0}$	3045	3047
$TE_{12,0}$	3322	3324

This leads to the conclusion that for PCB configurations where the tracks are not expected to appreciably affect the field distribution, f_c can be obtained to a good accuracy from the resonant frequencies of the same configuration but without the tracks.

4.7 CONCLUSION

Two dimensional edge elements are utilized to characterize the radiation and cross talk phenomenon on open and packed printed circuit boards. It is presented as a single method that can be used at any frequency, being limited only by computer

storage requirements if the device is very large in terms of wavelength. Also, the axial propagation phase constant β is set to zero since only the transverse characteristics are investigated; β vanishes at the cutoff frequencies and furthermore the mode pattern is frequency invariant.

The approach presented here modifies only the diagonal terms of the finite element matrix, and consequently the sparsity of the matrix, which is one of the most desired features of the finite element method, is not affected. This allows the use of efficient algorithms for sparse matrices. In addition, the matrix is banded and symmetric.

Numerical examples are presented to demonstrate the validity and applicability of the approach.

Chapter 5

Finite-Element Method Combined with Analytical Solutions of Rectangular Arbitrary-Large Housing with Aperture

5.1 PREVIEW

Real world is 3D, and 2D analysis is an approximation valid only for specific geometries and under certain circumstances as described in Chapter 3. In particular, longitudinal resonances cannot be accounted for via 2D modeling since the structure is assumed infinite in the axial direction. Hence, 3D solution may be used to check the validity and accuracy of 2D approximation. However, the number of equations needing solution increases dramatically in the 3D case. The cost for that is degradation in the accuracy of the results for large structures in terms of the wavelength, and demanding more computer storage which might exceed the capacity of the available computers. To overcome this limitation, the analytical solutions of a homogeneous rectangular housing with an aperture are coupled to the edge elements solution of the rest inhomogeneous part (inhomogeneity) of the problem, refer to Fig. 5.1. The coupling is accomplished via the continuity conditions at the aperture (the interface between the

inhomogeneity and the housing). Upon discretizing the inhomogeneity into tetrahedral edge elements, and enforcing the continuity conditions on the aperture, a system of linear equations is realized. The system of equations can be solved for the edge variables in the inhomogeneity and the amplitudes of the housing (cavity) modes. From the edge variables, the electric field distribution is obtained by the interpolating functions. Further, both the electric and magnetic fields in the cavity are available in terms of the modal expansions.

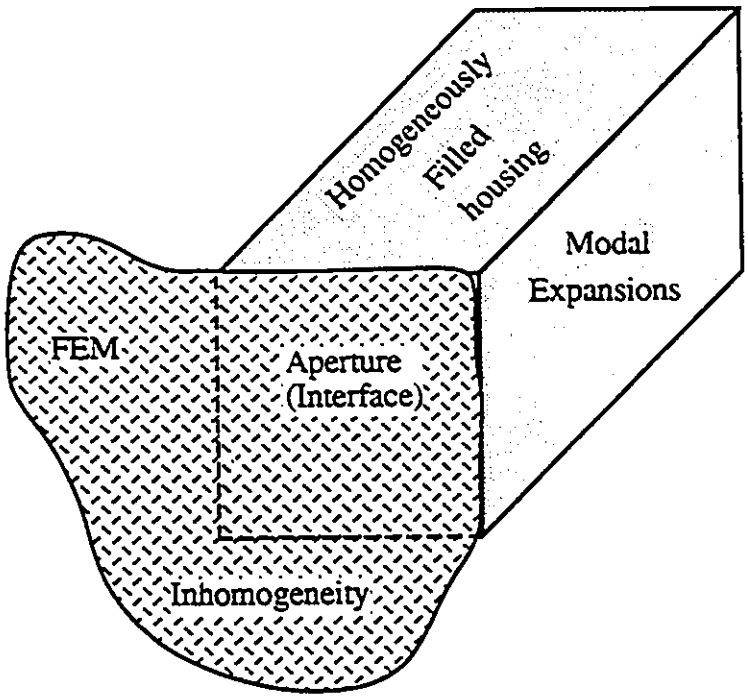

Figure 5.1: Inhomogeneous structure involving homogeneous rectangular housing.

This hybrid (throughout this Chapter, the word hybrid refers to the proposed FEM-Analytical Solutions hybrid method) is especially useful for packed PCB and VLSI. The circuit package is represented by a metal shield most of it is empty except for the substrate which constitutes only a small portion of the whole volume. Using the

hybrid, only the inhomogeneity need to be discretized. The outcomes are substantial reduction in the number of unknowns and CPU processing time and improving the accuracy of the results since the discretization error increases with the electrical size of the mesh [84].

The final matrix obtained is sparse except for the submatrices that correspond to the coupling of the two solutions at the aperture. The dimension of these submatrices is small being the number of terms in the modal expansion. To obtain accurate and reliable results, the propagating modes and only few evanescent modes (usually two) are sufficient. A further advantage of the solution is that it uses the edge-based FEM which is expected not to produce spurious solutions. In addition, the solution can be obtained without the need for matrix inversion.

5.2 Geometry of a Typical Application

Fig. 5.2 illustrates a typical configuration that can be tackled using the hybrid method. The metal enclosure might represent a circuit package whereas the substrate and signal tracks together with the sources are modeled by the inhomogeneity. This configuration is chosen for the sole matter of convenience, otherwise the method can handle any inhomogeneous problem involving arbitrary-large cavity with aperture.

The magnetic and electric fields in the empty volume are expressed in terms of modal expansions with unknown amplitudes. The rest inhomogeneous part is divided into tetrahedral edge elements. These two solutions are combined through the continuity of the fields tangential-components at the interface, see Fig. 5.2. The combination produces a linear system of equations wherein the unknowns are the modal amplitudes on the interface, and the edge variables in the inhomogeneous volume excluding the interface. Solving the linear system of equations determines the electric field distribution in the inhomogeneity, and both the electric and magnetic fields in the empty volume.

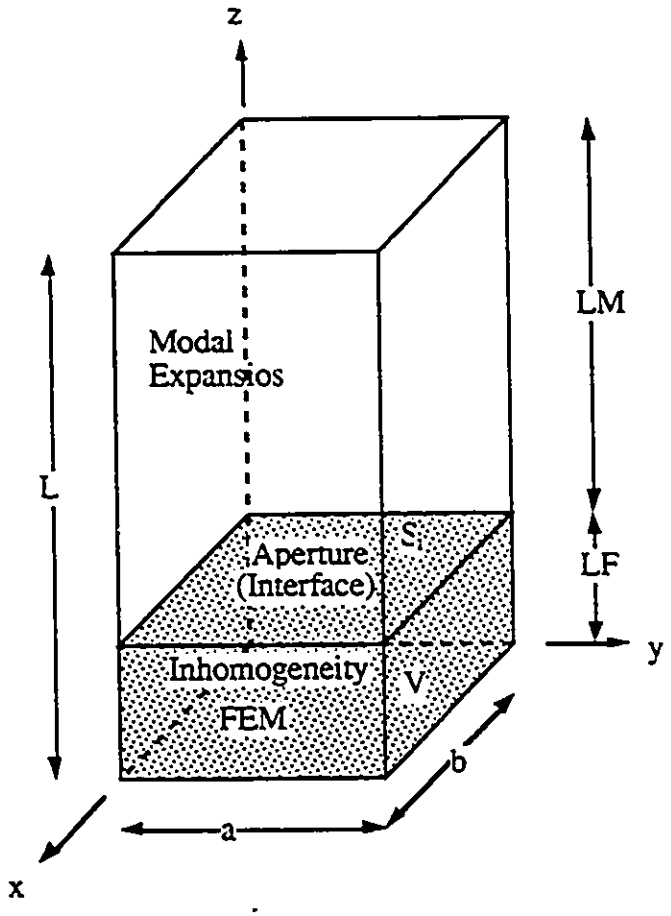

Figure 5.2: Housing partially-filled with inhomogeneity

5.3 VARIATIONAL ANALYSIS

The inhomogeneity is described by its conductivity σ, relative permittivity ϵ_r, and relative permeability μ_r. These quantities may of course represent anisotropic materials in which case ϵ_r and/or μ_r have to be written as tensors.

The fields in this region obey the vectorial wave equation

$$\nabla \times \frac{\nabla \times \vec{E}}{\mu_r} = k_0^2 \epsilon_c \vec{E}, \qquad \epsilon_c = \epsilon_r - j\frac{\sigma}{\omega \epsilon_0} \tag{5.1}$$

Alternatively, the fields are the solution of the variational equation

$$\delta F(\vec{E}^*) = 0 \tag{5.2}$$

where, $*$ denotes the complex conjugate, and $\vec{E}^*$ is chosen as the variational parameter in order that the final system of equations will be in terms of $\vec{E}$. The functional F corresponding to the wave equation (5.1) have been derived in Section 3.3. This functional is expressed as

$$F(\vec{E}^*) = \int_V [\frac{(\nabla \times \vec{E}) \cdot (\nabla \times \vec{E}^*)}{\mu_r} - k_0^2 \epsilon_c \vec{E} \cdot \vec{E}^*] dV - j\omega\mu_0 \int_{S_i} \vec{E}^* \times \vec{H} \cdot \hat{z}\, dS \tag{5.3}$$

in which V is the volume occupied by the inhomogeneity, $\hat{z}$ unit vector in the z direction, and S_i is the interface as depicted in Fig. 5.2.

Since the housing considered is rectangular, it could be helpful to express the interface integral of equation (5.3) in terms of the fields Cartesian components. Let the subscripts x and y refer to the x and y components, respectively, of the field quantity. Rewriting, Eq. (5.3) assumes the form

$$F(\vec{E}^*) = \int_V [\frac{(\nabla \times \vec{E}) \cdot (\nabla \times \vec{E}^*)}{\mu_r} - k_0^2 \epsilon_c \vec{E} \cdot \vec{E}^*] dV - j\omega\mu_0 \int_{S_i} [E_x^* H_y - E_y^* H_x]\, dS \tag{5.4}$$

5.4 FINITE-ELEMENTS DISCRETIZATION

In order to solve the functional F of the previous Section, the inhomogeneity is divided into tetrahedral edge elements. A typical tetrahedron is shown in Fig. 5.3, where the circulations of the tangential components of the electric and magnetic fields along a tetrahedron edge, characterized by nodes i and j, are denoted by the lower case letters e_{ij} and h_{ij}. Note the convention that the tangential field component is directed from node i to node j where $i < j$.

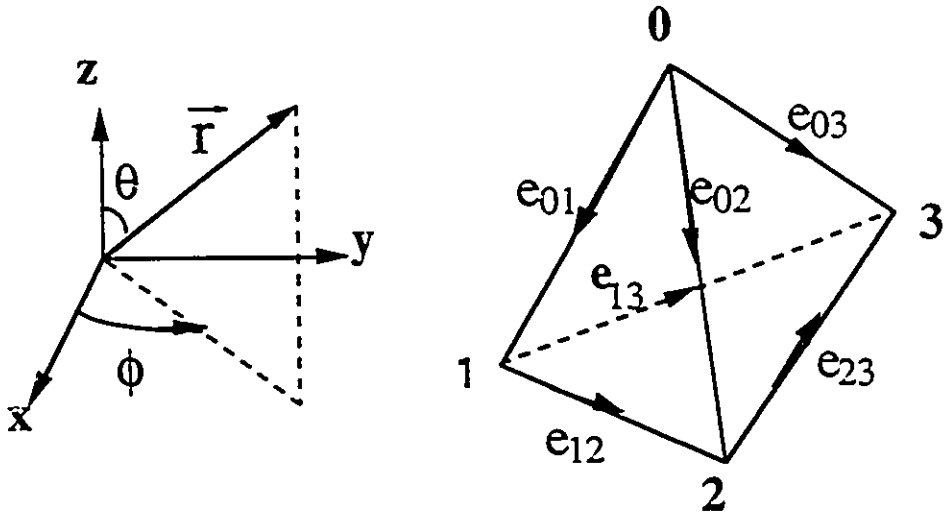

Figure 5.3: Tetrahedral edge element

The electric and magnetic fields within every element are expressed as

$$\vec{E} = \Sigma_{i<j}\ e_{ij}\vec{W}_{ij} \tag{5.5}$$

$$\vec{H} = \Sigma_{i<j}\ h_{ij}\vec{W}_{ij}$$

with the spacial vector $\vec{W}_{ij}$ being the Whitney basis function defined by [73]

$$\vec{W}_{ij} = \lambda_i \nabla\lambda_j - \lambda_j \nabla\lambda_i, \tag{5.6}$$

and λ_i is the barycentric function of node i expressed as

$$\lambda_i(\vec{r}) = \frac{1}{4} + \frac{(\vec{r} - \vec{r}_b)\cdot\vec{A}_i}{3V_e} \tag{5.7}$$

where $\vec{A}_i$ is the inwardly directed vectorial area of the tetrahedron face opposite to node i, V_e the element volume, and $\vec{r}$ the position vector. Also, $\vec{r}_b$ is the position vector of the barycenter of the tetrahedron defined as

$$\vec{r}_b = (\vec{r}_0 + \vec{r}_1 + \vec{r}_2 + \vec{r}_3)/4 \tag{5.8}$$

in which $\vec{r}_i$ is the position vector of node i.

Below, the contribution of a tetrahedral element to the interface integral is derived. So, let a tetrahedron has a triangular facet on the interface S_i. Further let us use a convenient local numbering scheme for the triangles on the interface, as illustrated in Fig. 5.4. The numbering scheme proposed for the triangular facet is consistent with the local numbering of the tetrahedral elements in that tangential component is directed from node i to node j where $i < j$.

Using the interpolating expansions of Eqns. (5.5), the interface integral over a triangular facet Ω_e is transformed to

$$\int_{\Omega_e} [E_x^* H_y - E_y^* H_x]\, dS = \tag{5.9}$$
$$\int_{\Omega_e} [(\sum_{i<j} e_{ij}^* \hat{x}\cdot\vec{W}_{ij})(\sum_{i<j} h_{ij}\hat{y}\cdot\vec{W}_{ij}) - (\sum_{i<j} e_{ij}^*\hat{y}\cdot\vec{W}_{ij})(\sum_{i<j} h_{ij}\hat{x}\cdot\vec{W}_{ij})]\, dS$$

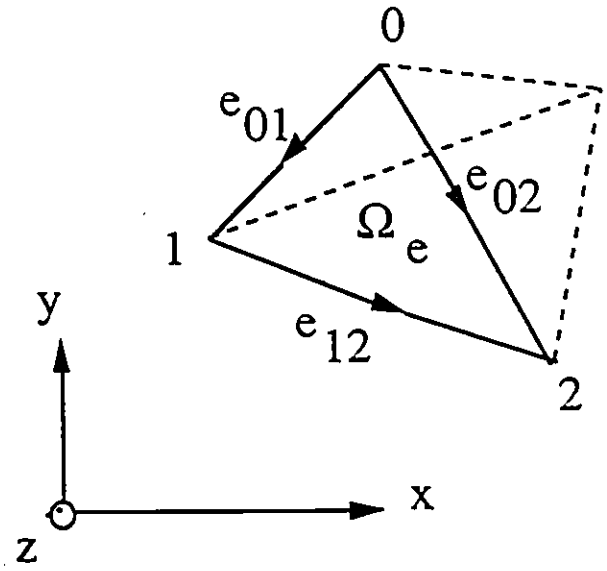

Figure 5.4: Tetrahedron facet on the interface and its local numbering

Rewriting this equation in matrix form

$$\int_{\Omega_e} [E_x^* H_y - E_y^* H_x]\, dS = \tag{5.10}$$

$$\int_{\Omega_e} \left[\begin{array}{ccc} e_{01}^* & e_{02}^* & e_{12}^* \end{array}\right] (\hat{x} \cdot \left[\begin{array}{c} \vec{W}_{01} \\ \vec{W}_{02} \\ \vec{W}_{12} \end{array}\right] \hat{y} \cdot \left[\begin{array}{ccc} \vec{W}_{01} & \vec{W}_{02} & \vec{W}_{12} \end{array}\right]$$

$$- \hat{y} \cdot \left[\begin{array}{c} \vec{W}_{01} \\ \vec{W}_{02} \\ \vec{W}_{12} \end{array}\right] \hat{x} \cdot \left[\begin{array}{ccc} \vec{W}_{01} & \vec{W}_{02} & \vec{W}_{12} \end{array}\right]) \left[\begin{array}{c} h_{01} \\ h_{02} \\ h_{12} \end{array}\right] dS$$

Note that the edge variables e_{ij} and h_{ij} are constants in every element, and the Whitney vector function has a known analytical form given by Eq. (5.6). This makes it possible to evaluate the interface integral analytically. It is easy to show that

$$\int_{\Omega_e} [E_x^* H_y - E_y^* H_x]\, dS = \left[\begin{array}{ccc} e_{01}^* & e_{02}^* & e_{12}^* \end{array}\right] [U]_e \left[\begin{array}{c} h_{01} \\ h_{02} \\ h_{12} \end{array}\right], \tag{5.11}$$

$$[U]_e = \frac{A_e}{108 V_e^2} \left[\begin{array}{ccc} 0 & -u21 & -u31 \\ u21 & 0 & -u32 \\ u31 & u32 & 0 \end{array}\right],$$

$$u21 = \tag{5.12}$$

$$2A_{2x}A_{1y} - A_{0y}A_{2x} - A_{1y}A_{0x} -$$

$$2A_{2y}A_{1x} + A_{2y}A_{0x} + A_{0y}A_{1x}$$

$$u31 = \tag{5.13}$$

$$A_{2x}A_{1y} - 2A_{2x}A_{0y} + A_{1x}A_{0y} -$$

$$A_{2y}A_{1x} + 2A_{2y}A_{0x} - A_{1y}A_{0x}$$

$$u32 = \tag{5.14}$$

$$-A_{2x}A_{0y} - A_{1x}A_{2y} + 2A_{1x}A_{0y} +$$

$$A_{2y}A_{0x} + A_{1y}A_{2x} - 2A_{1y}A_{0x}$$

where A_e is the area of the triangular facet, V_e the volume of the corresponding tetrahedron, A_{ix} the x component of $\vec{A}_i$, and A_{iy} the y component of $\vec{A}_i$.

The element matrices resulting from discretizing the volume integral of Eq. (5.4) can be found in [84]. These matrices, denoted by $[S]_e$ and $[T]_e$, are rewritten here for easy reference.

$$[S]_e = \frac{1}{9\mu_r V_e}\begin{bmatrix} \vec{t}_{2,3}\cdot\vec{t}_{2,3} & & & & & \\ -\vec{t}_{1,3}\cdot\vec{t}_{2,3} & \vec{t}_{1,3}\cdot\vec{t}_{1,3} & & & & \\ \vec{t}_{1,2}\cdot\vec{t}_{2,3} & -\vec{t}_{1,2}\cdot\vec{t}_{1,3} & \vec{t}_{1,2}\cdot\vec{t}_{1,2} & & & \\ \vec{t}_{0,3}\cdot\vec{t}_{2,3} & -\vec{t}_{0,3}\cdot\vec{t}_{1,3} & \vec{t}_{0,3}\cdot\vec{t}_{1,2} & \vec{t}_{0,3}\cdot\vec{t}_{0,3} & & \\ -\vec{t}_{0,2}\cdot\vec{t}_{2,3} & \vec{t}_{0,2}\cdot\vec{t}_{1,3} & -\vec{t}_{0,2}\cdot\vec{t}_{1,2} & -\vec{t}_{0,2}\cdot\vec{t}_{0,3} & \vec{t}_{0,2}\cdot\vec{t}_{0,2} & \\ \vec{t}_{0,1}\cdot\vec{t}_{2,3} & -\vec{t}_{0,1}\cdot\vec{t}_{1,3} & \vec{t}_{0,1}\cdot\vec{t}_{1,2} & \vec{t}_{0,1}\cdot\vec{t}_{0,3} & -\vec{t}_{0,1}\cdot\vec{t}_{0,2} & \vec{t}_{0,1}\cdot\vec{t}_{0,1} \end{bmatrix} \tag{5.15}$$

$$[T]_e = \frac{\epsilon_r}{180V_e}\begin{bmatrix} 2(I_{00}- & & & & & \\ I_{01}+I_{11}) & & & & & \\ I_{00}-I_{01} & 2(I_{00}- & & & & \\ -I_{02}+2I_{12} & I_{02}+I_{22}) & & & & \\ I_{00}-I_{01} & I_{00}-I_{02} & 2(I_{00}- & & & \\ -I_{03}+2I_{12} & -I_{03}+2I_{23} & I_{03}+I_{33}) & & & \\ I_{01}-I_{11} & 2I_{01}-I_{12} & I_{01}-I_{13} & 2(I_{11}- & & \\ -2I_{02}+I_{12} & -I_{02}+I_{22} & -I_{02}+I_{23} & I_{12}+I_{22}) & & \\ I_{01}-I_{11} & I_{01}-I_{12} & 2I_{01}-I_{13} & I_{11}-I_{12} & 2(I_{11}- & \\ -2I_{03}+I_{13} & -I_{03}+I_{23} & -I_{03}+I_{33} & -I_{13}+2I_{23} & I_{13}+I_{33}) & \\ I_{02}-I_{12} & I_{02}-I_{22} & 2I_{02}-I_{23} & I_{12}-I_{22} & 2I_{12}-I_{23} & 2(I_{22}- \\ -I_{03}+I_{13} & -2I_{03}+I_{23} & -I_{03}+I_{33} & -2I_{13}+I_{23} & -I_{13}+I_{33} & I_{23}+I_{33}) \end{bmatrix} \tag{5.16}$$

where $\vec{t}_{k,l}$ is a vector from node k to node l, and $\{k,l\} = \{0,1,2,3\} - \{i,j\}$, with $k < l$, and $I_{ij} = \vec{A}_i \cdot \vec{A}_j$.

The edge elements discretization described converts the functional F into a matrix form expressed as

$$F = [E_t^*]^T([S] - k_0^2[T])[E_t] - j\omega\mu_0[E_{t,i}^*]^T[U][H_{t,i}] - [E_t^*]^T[\Psi] \tag{5.17}$$

where the global matrices $[S]$, $[T]$, and $[U]$ are the assembly of the element matrices $[S]_e$, $[T]_e$, and $[U]_e$, respectively. The matrices $[E_t]$ and $[H_t]$ involve the edge variables related to the electric and magnetic fields, and the vector $[\Psi]$ is the excitation vector. Finally, the subscript i indicates the edge variables on the interface.

5.5 Modal Expansions

Linear combinations of TE and TM modes may be used to provide a complete and general solution for the fields in the cavity part of the problem. Utilizing such practically-important and commonly-used types of modes might help making the hybrid a convenient method to implement and use.

The transverse components of the electric and magnetic fields, in the cavity depicted in Fig. 5.2, are expanded in terms of the modes labeled by integer subscripts m and n. (Note that the boundary conditions at the aperture are not known yet.)

$$
\begin{aligned}
E_x &= \sum_{m,n} C_1^{m,n} E_x^{TE_{m,n}} + C_2^{m,n} E_x^{TM_{m,n}} \\
E_y &= \sum_{m,n} C_1^{m,n} E_y^{TE_{m,n}} + C_2^{m,n} E_y^{TM_{m,n}} \\
H_x &= \sum_{m,n} C_1^{m,n} H_x^{TE_{m,n}} + C_2^{m,n} H_x^{TM_{m,n}} \\
H_y &= \sum_{m,n} C_1^{m,n} H_y^{TE_{m,n}} + C_2^{m,n} H_y^{TM_{m,n}}
\end{aligned}
\tag{5.18}
$$

In these equations, the unknowns are the amplitude coefficients $C_1^{m,n}$ and $C_2^{m,n}$, while the basis functions $E_x^{TE_{m,n}}$, $E_x^{TM_{m,n}}$, $E_y^{TE_{m,n}}$, $E_y^{TM_{m,n}}$, $H_x^{TE_{m,n}}$, $H_x^{TM_{m,n}}$, $H_y^{TE_{m,n}}$, and $H_y^{TM_{m,n}}$ are expressed as

$$
H_x^{TE_{m,n}} = \frac{jn\pi\beta}{bk_c^2} \sin\frac{n\pi x}{b} \cos\frac{m\pi y}{a} \cos\beta(L-z) \tag{5.19}
$$

$$H_y^{TE_{m,n}} = \frac{jm\pi\beta}{ak_c^2}\cos\frac{n\pi x}{b}\sin\frac{m\pi y}{a}\cos\beta(L-z) \quad (5.20)$$

$$E_x^{TE_{m,n}} = jZ_h H_y^{TE_{m,n}}\tan\beta(L-z) \quad (5.21)$$

$$E_y^{TE_{m,n}} = -jZ_h H_x^{TE_{m,n}}\tan\beta(L-z) \quad (5.22)$$

$$E_x^{TM_{m,n}} = \frac{n\pi\beta}{bk_c^2}\cos\frac{n\pi x}{b}\sin\frac{m\pi y}{a}\sin\beta(L-z) \quad (5.23)$$

$$E_y^{TM_{m,n}} = \frac{m\pi\beta}{ak_c^2}\sin\frac{n\pi x}{b}\cos\frac{m\pi y}{a}\sin\beta(L-z) \quad (5.24)$$

$$H_x^{TM_{m,n}} = \frac{j}{Z_e}E_y^{TM_{m,n}}\cot\beta(L-z) \quad (5.25)$$

$$H_y^{TM_{m,n}} = -\frac{j}{Z_e}E_x^{TM_{m,n}}\cot\beta(L-z) \quad (5.26)$$

where the dimensions a, b, and L are as shown in Fig. 5.2. The transverse cutoff wavenumber k_c, the axial propagation phase phase constant β, the H-mode impedance Z_h, and the E-mode impedance Z_e for mode m,n are given by

$$k_c^2 = (\frac{m\pi}{a})^2 + (\frac{n\pi}{b})^2 \quad (5.27)$$

$$\beta^2 = k_0^2 - k_c^2 \quad (5.28)$$

$$Z_h = \frac{k_0 Z_0}{\beta} \quad (5.29)$$

$$Z_e = \frac{\beta Z_0}{k_0} \quad (5.30)$$

$$Z_0 = 120\pi, Ohm \quad (5.31)$$

5.6 The Hybrid Formulation

The functional in its discrete form given by Eq. (5.17) is rewritten here for convenience

$$F = [E_t^*]^T([S] - k_0^2[T])[E_t] - j\omega\mu_0[E_{t,i}^*]^T[U][H_{t,i}] - [E_t^*]^T[\Psi] \quad (5.32)$$

Separating the edge variables on the interface, the vectors $[E_t]$ and $[\Psi]$ assume the form

$$[E_t] = \begin{bmatrix} E_{t,o} \\ E_{t,i} \end{bmatrix} \tag{5.33}$$

$$[\Psi] = \begin{bmatrix} \Psi_o \\ \Psi_i \end{bmatrix}$$

where the subscript i refers to the edge variables on the interface, and the subscript o refers to the remaining edge variables.

To manipulate the functional, let us partition the square symmetric matrix $([S] - k_0^2[T])$

$$([S] - k_0^2[T]) = \begin{bmatrix} A_{11} & A_{12} \\ A_{12}^T & A_{22} \end{bmatrix} \tag{5.34}$$

Observe that the square brackets of the submatrices $[A_{11}]$, $[A_{12}]$, and $[A_{22}]$ have been dropped for convenience.

Substituting (5.33) and (5.34) into (5.32) yields

$$\begin{aligned} F = & \\ & \begin{bmatrix} E_{t,o}^{*T} & E_{t,i}^{*T} \end{bmatrix} \begin{bmatrix} A_{11} & A_{12} \\ A_{12}^T & A_{22} \end{bmatrix} \begin{bmatrix} E_{t,o} \\ E_{t,i} \end{bmatrix} \\ & - j\omega\mu_0 [E_{t,i}^*]^T [U] [H_{t,i}] - \begin{bmatrix} E_{t,o}^{*T} & E_{t,i}^{*T} \end{bmatrix} \begin{bmatrix} \Psi o \\ \Psi i \end{bmatrix} \end{aligned} \tag{5.35}$$

In virtue of the continuity conditions, the edge variables on the interface may be related to the analytical solutions written in Section 5.5. The analytical solutions are expressed in terms of the x and y components of the fields whereas the state variables of the FEM are associated with the tangential components of the fields along the mesh edges. Thus, a geometrical relationship must be used to relate these quantities. Fig. 5.5 shows an arbitrary edge, labeled by the integers i and j, of length L_e residing on the interface. Let the angle of the edge vector measured from the x-axis be denoted by ϕ. The edge variables are related to the x and y components of the fields through the following geometrical relationships

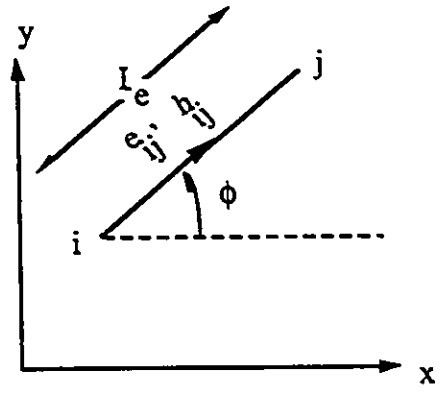

Figure 5.5: Arbitrary edge on the interface

$$e_{ij} = (E_x \cos\phi + E_y \sin\phi) L_e \tag{5.36}$$

$$h_{ij} = (H_x \cos\phi + H_y \sin\phi) L_e \tag{5.37}$$

Using this geometrical formula, the edge variables can be easily expressed in terms of the modal amplitude coefficients. This relationship in matrix form is written as

$$[E_{t,i}] = [P][C] \tag{5.38}$$

$$[H_{t,i}] = [Q][C]$$

where $[P]$ and $[Q]$ are matrices with known entries, and $[C]$ is the vector containing the modal amplitude coefficients.

Combining Equations (5.36) - (5.38), and performing the variational derivative give the system of equations

$$\begin{bmatrix} A_{11} & D_{12} \\ D_{12}{}^T & D_{22} \end{bmatrix} \begin{bmatrix} E_{t,o} \\ C \end{bmatrix} = \begin{bmatrix} \Psi_o \\ \Upsilon_i \end{bmatrix}, \tag{5.39}$$

$$[D_{12}] = [A_{12}][P], \quad [\Upsilon_i] = [P]^T[\Psi_i],$$
$$[D_{22}] = [P]^T([A_{22}][P] - j\omega\mu_0[U][Q])$$

This system of equations is readily solved for the edge variables $[E_{t,o}]$ and the modal amplitudes $[C]$.

5.7 APPLICATIONS

Several examples are considered to show the validity, accuracy, and usefulness of the hybrid solution. Dielectric fillings, sharp metal edges, and finite-conductivity regions are features of these examples. It is to be stressed here that no special singular trial functions are used to model the sharp metal edges, yet accurate results are obtained as expected. Another point worth mentioning is that excitations are modeled by Dirichlet boundary conditions; the edge variable at the location of excitation is normalized to unity.

The hybrid method solutions are compared to analytical solutions, other published data, the pure edge-based finite element method, and experimental results. structures having dimensions comparable to the wavelength were not possible to solve using the edge elements method alone on the available computer resources (3100 DecStation, 16 Mbyte RAM) due to storage limitations. Using the hybrid method, problems with arbitrary-large housing are possible to solve, however the size of the inhomogeneous part in the problem is again limited by the computer storage. Incidentally, not only the available computer resources are responsible for these limitations. Two other factors contribute to this problem, viz., the solver of the linear system of equations and the unavailability of an adaptive mesh generator. Eventhough the solver used, called sparse, was designed for sparse matrices, the LU decomposition process on which the solver is based produces fill-ins (non-zero entries) in the matrix and thus reduces the sparsity of the matrix. There are some parameters that can be adjusted to control the growth of the elements and reduce the fill-ins, but this is a matter of tradeoff between accuracy

and computer storage demands. Furthermore, if the matrix is not well-conditioned, adjusting these parameters has a minor effect.

In order to solve problems comparable to the wave-length, a more efficient solver is needed, e.g., the biconjugate gradient solver. Needed also is an adaptive mesh generator which generates a refined mesh near field discontinuities and small objects, and coarse mesh where the field variation is expected to be slow. With an adaptive mesh generator, less number of unknowns are required to obtain the same accuracy as compared to a uniform mesh.

The applications investigated are

Metal Enclosures

- Large empty cavity
- Half-filled cavity
- Cavity with ridge

Packed Lands (conductors) on Dielectric Boards (VLSI)

- Loops
    1. Loop and patch
    2. Cross-talk between two loops
- Planar Transmission Lines (Microstrips)
    1. Single TL

2. Cross-talk between two terminated TL's embedded in dielectric substrate

3. Cross-talk between two unloaded TL's.

- Experimental Results

Following is description of these examples.

5.7.1 Metal Enclosures

- Large Empty Cavity

  The objective of this example is to illustrate the application of the hybrid method. The dimensions of the cavity are 5 mm × 50 mm × 501.6 mm as shown in Fig. 5.6. In order to apply the hybrid, an artificial interface is introduced at $z = 6.6$ mm and the volume below the interface is divided into three layers of tetrahedrons, refer to Fig. 5.6. The resulting number of unknown edges is 546. Only one mode below cutoff in addition to the propagating modes are used to represent the solution in the volume above the interface, $z > 6.6$ mm. Obviously, the edge-based FEM alone cannot solve this example on the available 3100 DecStation (16 Mbyte RAM) since using the same discretization scheme for the whole structure produces over 65000 total number of edges.

  The excitation V_1 is located at the point $(2.5, 1.25, 1.6)$ mm and the output V_2 is monitored at the point $(22.5, 1.25, 1.6)$ mm. Fig. 5.7 shows the frequency response of the empty cavity. The excursions of the output voltage in this plot are attributed to the excitation of the cavity modes. These resonant frequencies are compared to the exact values in the table below where the maximum relative

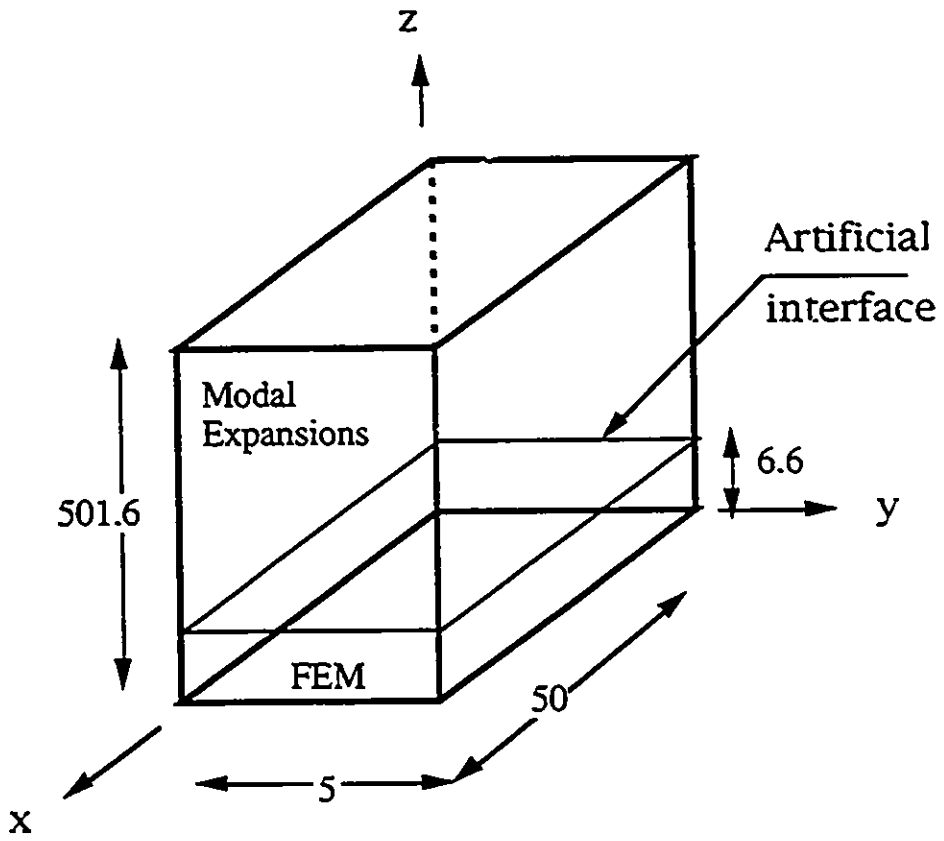

Figure 5.6: Empty cavity modeled by the hybrid method.

error is less than 0.3%.

Mode number	*Cutoff frequency (GHz)*		% error
	computed	exact	
1,0,1	3.015	3.015	0
1,0,2	3.060	3.059	0.03
1,0,3	3.132	3.131	0.03
1,0,4	3.232	3.230	0.06
1,0,5	3.355	3.352	0.09
1,0,6	3.500	3.496	0.11
1,0,7	3.663	3.658	0.14
1,0,8	3.844	3.837	0.18
1,0,9	4.038	4.030	0.20
1,0,10	4.245	4.236	0.21
1,0,11	4.462	4.452	0.22
1,0,12	4.688	4.677	0.24
1,0,13	4.923	4.911	0.24
1,0,14	5.163	5.150	0.25
1,0,15	5.41	5.396	0.26
1,0,16	5.663	5.647	0.28
1,0,17	5.918	5.903	0.25
2,0,1	6.008	6.007	0.02
2,0,2	6.03	6.03	0
2,0,3	6.067	6.067	0
2,0,4	6.119	6.118	0.02
1,0,18	6.178	6.162	0.26
2,0,5	6.185	6.183	0.03
2,0,6	6.265	6.263	0.03
2,0,7	6.358	6.355	0.05
1,0,19	6.443	6.425	0.28
2,0,8	6.463	6.459	0.06
2,0,9	6.581	6.576	0.08
1,0,20	6.708	6.691	0.25
2,0,10	6.710	6.704	0.09
2,0,11	6.849	6.843	0.09
1,0,21	6.978	6.960	0.26
2,0,12	6.999	6.991	0.11

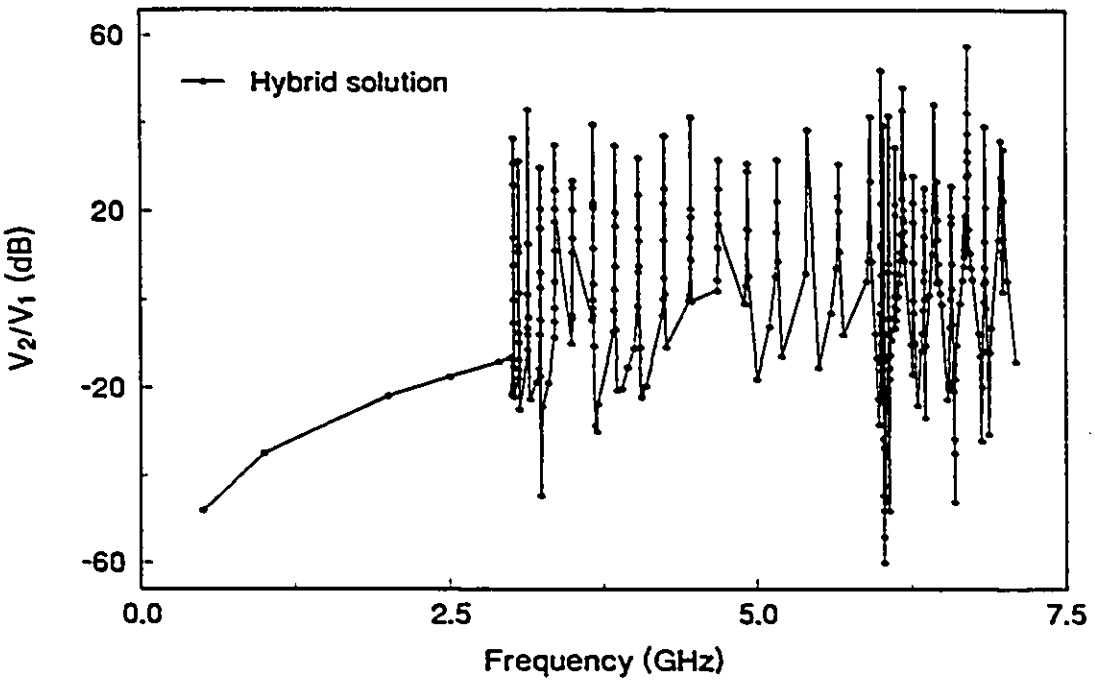

Figure 5.7: Frequency response of the empty cavity

- Half-Filled Cavity

  This example is aimed at testing the validity of the hybrid method for inhomogeneous problems. For that reason, the cavity is half filled with $\epsilon_r = 2$ dielectric material as depicted in Fiq. 5.8.

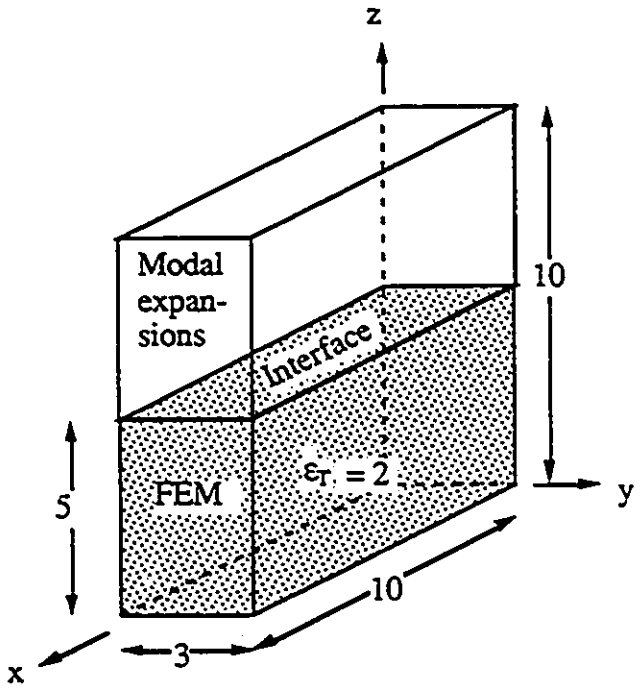

Figure 5.8: Half-Filled cavity.

The interface, needed by the hybrid solution, is chosen to be the surface of the dielectric as illustrated in Fig. 5.8, and only the dielectric is discretized. Further, one evanescent mode and the propagating modes are used in the modal expansions. The computed resonant frequencies of this structure compares well to the

analytical solutions in the following table.

Mode number	*Cutoff frequency (GHz)*		% error
	computed	exact	
1, 0, 1	16.615	16.893	1.6
2, 0, 1	25.62	25.998	1.5
1, 0, 2	28.95	28.338	2.2
3, 0, 1	35.32	35.824	1.4
2, 0, 2	36.33	36.445	0.3
1, 0, 3	38.16	38.656	1.3

- Cavity with Ridge

  The ridge with its sharp metal edges is modeled without the need for special singular trial functions. The geometry of the problem is drawn in Fig. 5.9 where an artificial interface is introduced in order to reduce the number of unknowns needing solution. The modal expansions used in the hybrid solution involve the propagating and ten modes below cutoff. As a matter of fact, five evanescent and the propagating modes are sufficient. In order to solve the problem numerically, a uniform mesh is generated to represent the FEM region of the problem in Fig. 5.9. The space division of the mesh is 1 mm in y and z directions while 0.938 mm space division (8 divisions) is used in the x direction. Accordingly, 661 unknown edges are produced. The computed resonant frequencies of this structure are compared with an eigen-value solution using the pure edge-based FEM [85] in

the table below. The two solutions are in good agreement.

	Computed resonance frequency (GHz)		%
	Hybrid solution	Edge-Elements solution [85]	relative difference
1	24.198	23.868	1.4
2	35.57	35.113	1.3
3	36.9	37.395	1.3
4	37.87	37.92	0.1
5	38.28	38.001	0.7
6	41.93	41.301	1.5
7	43.03	42.571	1.1
8	43.748	43.464	0.6
9	46.5	46.586	0.2
10	48.02	47.398	1.3

Remark that an adaptive mesh refined near the field discontinuities and coarse elsewhere would better represent the geometry at hand with less number of unknowns. For the simple reason that no commercial mesh generator is available for our research group, now, a uniform mesh in most cases is used. This remark holds for all the examples presented in this thesis.

5.7.2 Packed Lands on Dielectric Boards (VLSI)

- Loops

  Two examples are included in this Section. The field distributions of the first example obtained by the pure edge-elements method are compared to those obtained by the hybrid method. In the second example, the cross-talk between two loops in close proximity is computed by both the edge elements and the hybrid methods. The two solutions are in excellent agreement.

  1. Loop and Patch

     Loop and a rectangular land (patch) on dielectric board surrounded by metal package is shown in Fig. 5.10. Since circuits are nothing other than loops,

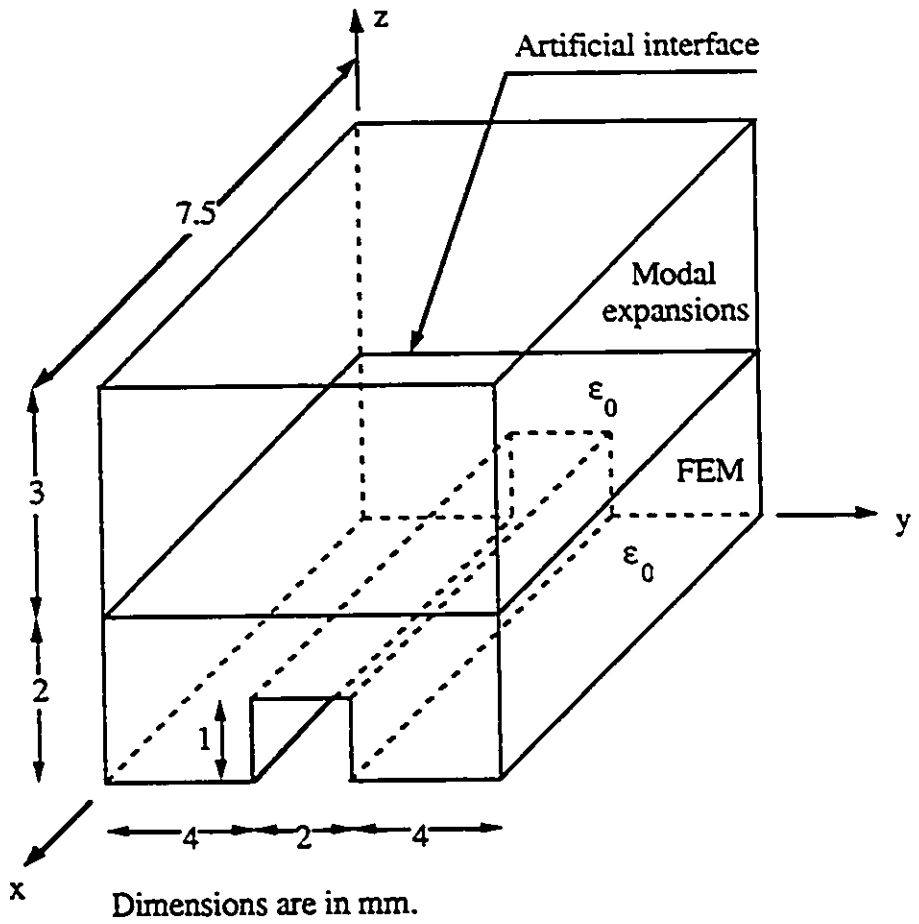

Figure 5.9: Cavity with ridge modeled by the hybrid method.

this loop might represent a circuit. For the edge elements solution, the whole structure is divided into tetrahedral elements. The space division is 1.6 mm in z direction, and 2.5 mm otherwise. On the other hand, an artificial interface is placed at $z = 3.2$ mm for the hybrid method application. The region under the interface is discretized into two layers of tetrahedrons, and the modal expansions used involve five evanescent modes.

The total electric field distributions inside the substrate at $z = 0.8$ mm for six arbitrarily-chosen frequencies ($f = 0.5, 2, 4, 5, 6$, and 7 GHz) are shown in Fig. 5.11. Again, it is clear from these distributions that the hybrid and the edge elements solutions are almost identical. The advantage of the hybrid method in reducing the number of unknowns will be more significant for larger height structures. These long structures are not possible to solve by the pure edge elements method on the available resources (3100 DecStation, 16 Mbyte) since the disc storage limit will be exceeded.

The first resonance of the enclosure (if the substrate is removed) occurs at 11.39 GHz for the $TE_{1,1,0}$ mode. Incidentally, from the numerical results, a resonance behavior of the packed circuit is observed at $f = 6$ GHz, i.e., below the first resonance of the enclosure. This resonance is attributed to the circuit itself and is explained as follows. The loop may be viewed as a short-circuited transmission line. It is well known that a short-circuited transmission line resonates at frequencies for which its length is multiple of a quarter wavelength. Therefore, let us approximately compute the resonant wavelength at $f = 6$ GHz using the empirical formula

$$\lambda_{resonance} = \frac{\lambda_0}{\sqrt{\epsilon_r}} = 33.71\, mm \tag{5.40}$$

The average length of the loop is 33.75 mm, and consequently this resonance is the fourth resonance. In fact, the effective dielectric constant has to be used in the formula (5.40) rather than the dielectric constant of the substrate. The fringing of the fields also has to be taken into account by

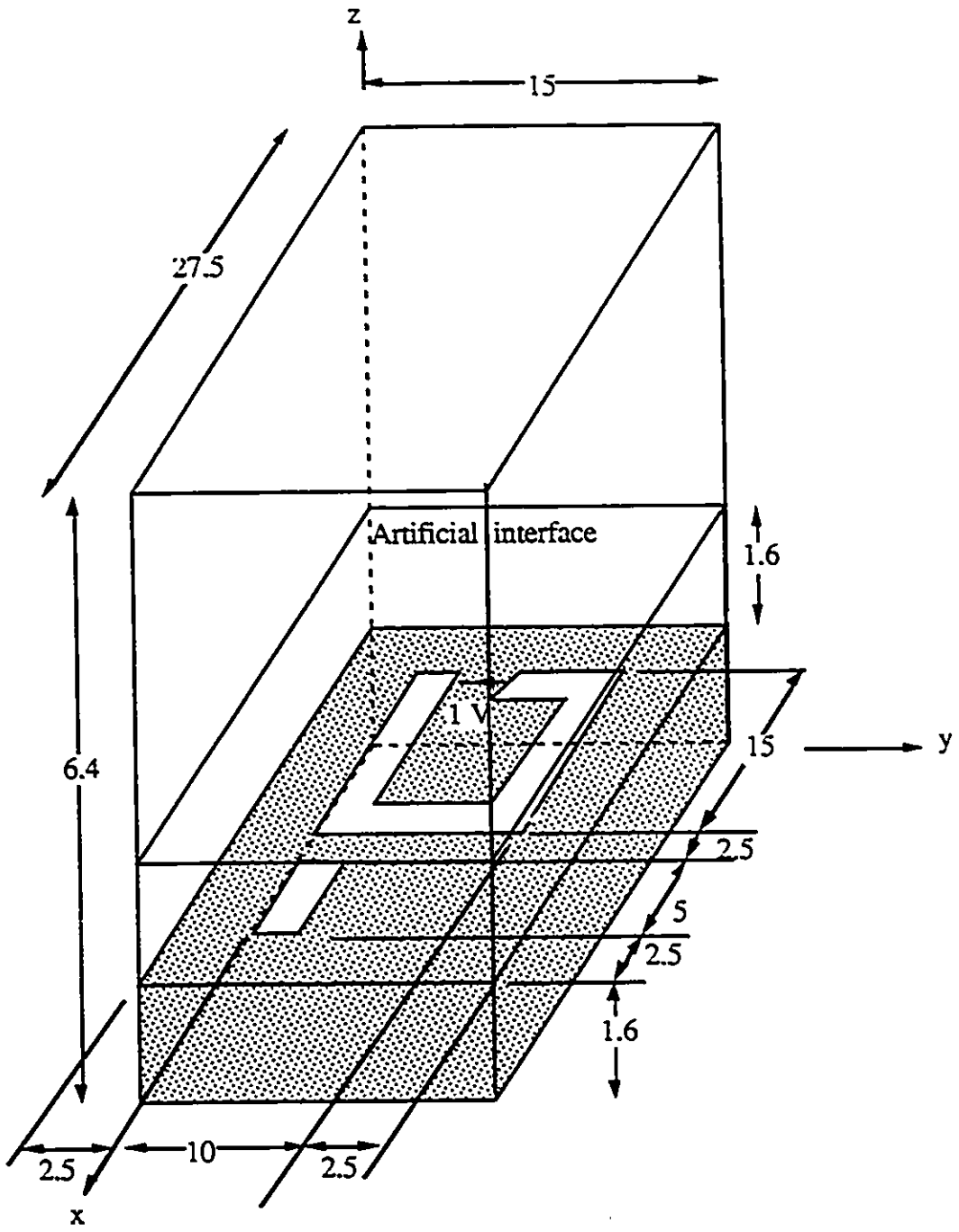

Dimensions are in mm. Conductor width is 2.5 mm.

Figure 5.10: Loop and patch on dielectric board in metal housing.

Figure 5.11: The total electric field distributions ((a),(b),(c),(d),(e), and (f)) inside the substrate at $z = 0.8$ mm of the "Loop and patch" example.

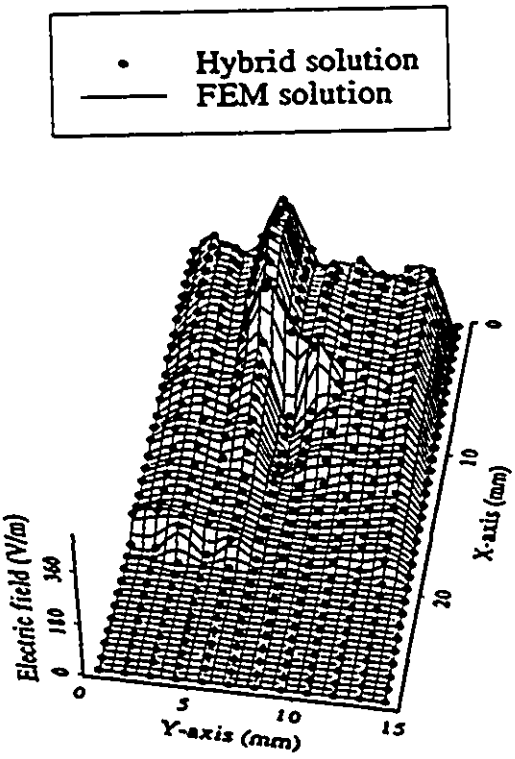

Figure 5.11: (a) $f = 500$ MHz

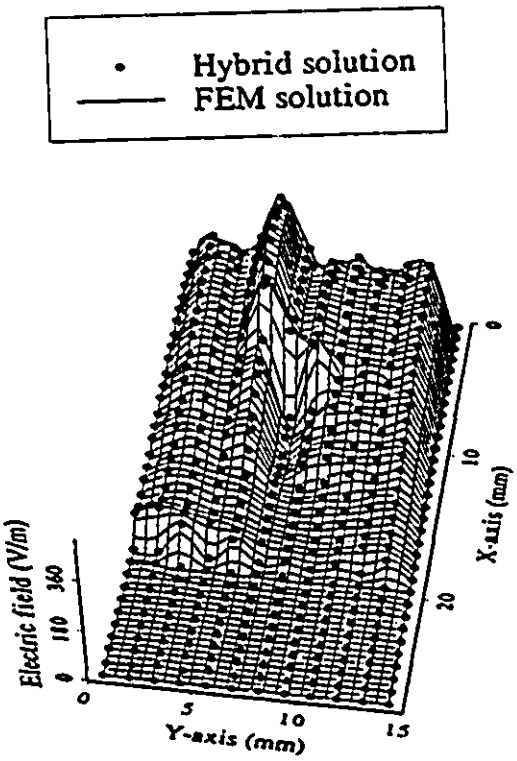

Figure 5.11: (b) $f = 2$ GHz

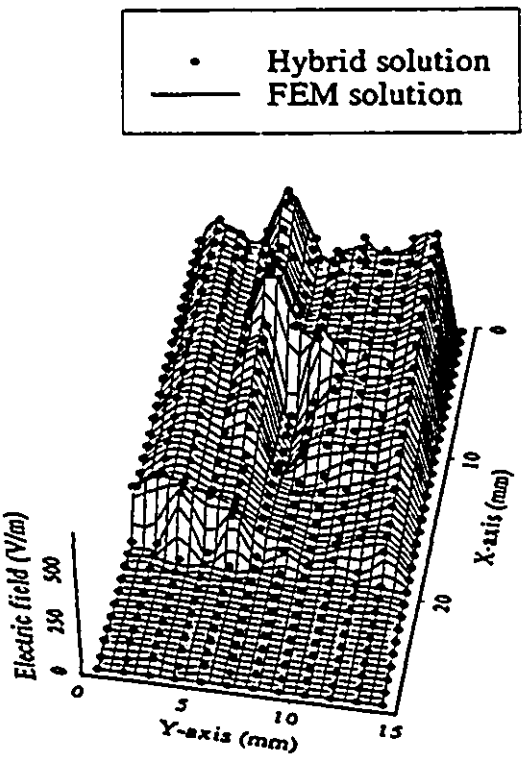

Figure 5.11: (c) $f = 4$ GHz

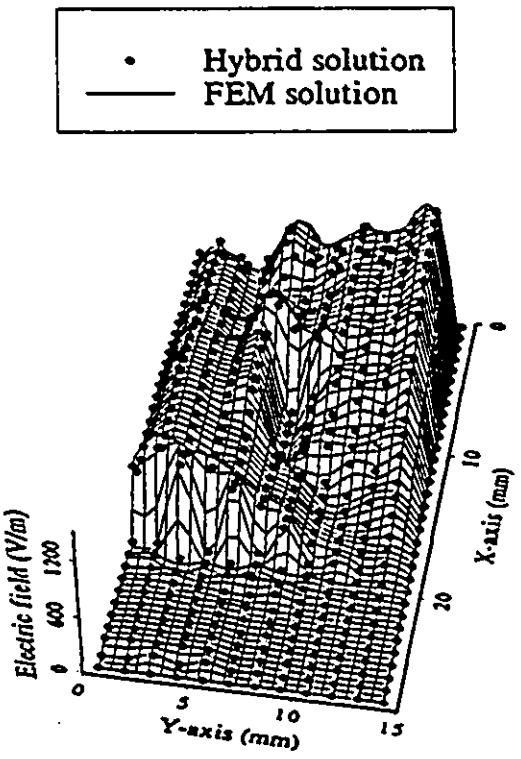

Figure 5.11: (d) $f = 5$ GHz

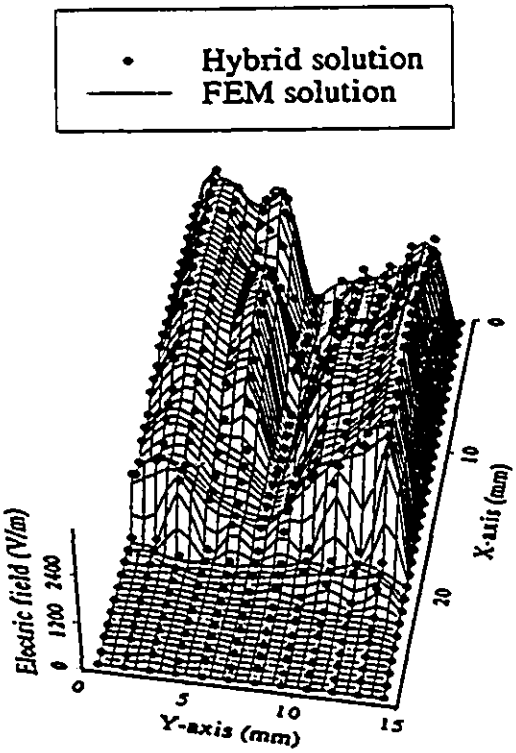

Figure 5.11: (e) $f = 6$ GHz

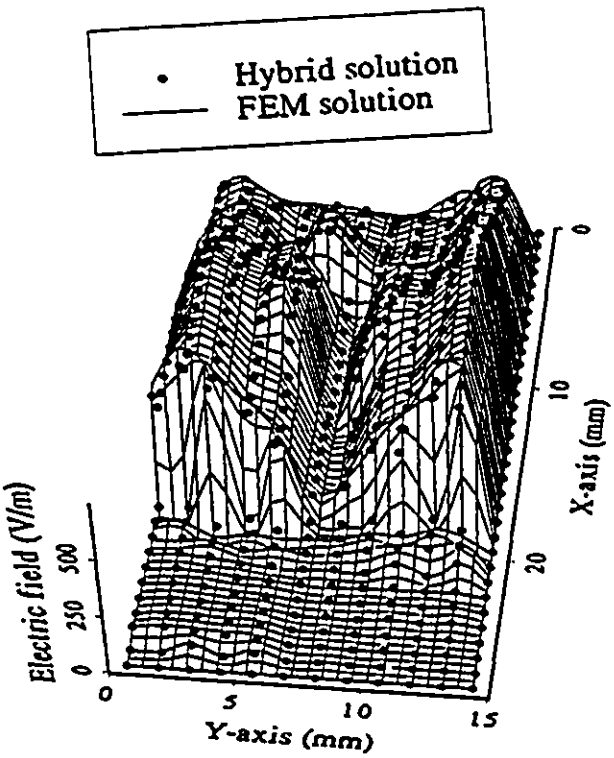

Figure 5.11: (f) $f = 7$ GHz

adjusting the equivalent TL length. Seemingly, these two factors tend to offset each other, and the simple prediction is in excellent agreement with the numerical result.

2. Cross-Talk between Two Loops

One of the problems that concern the EMC society is the cross-talk which is classified as an intra-system interference. In other words, the electronic system interferes with itself. This happens when conductors inside the system are placed close together such that the electromagnetic fields couple from one conductor to the other causing degradation of the system performance. Furthermore, the system shield may enhance the cross-talk for frequencies nearby the resonance of the shield itself. In order to analyze the cross-talk phenomenon, consider the two arbitrary-shaped loops on top of a dielectric board enclosed by a metal enclosure as illustrated in Fig. 5.12. In this figure, the excitation is V_1 and the cross-talk voltage is V_2. The height of the package L is set to $L = 0.91$ cm, and the frequency response of the cross-talk represented by the transfer function ratio V_2/V_1 is computed by both the edge elements and hybrid methods. The two solutions are indistinguishable as plotted in Fig. 5.13. Resonances at the frequencies 2 GHz and 5 GHz are observed in the figure. These resonances are not due to the shield since the first resonant frequency of the shield is 7.8 GHz. Rather, the cause of these voltage excursions is the resonances of the short-circuited TL (loop) as discussed in the "Loop and Patch" example. Note that the second resonant frequency is not twice the first resonant frequency as expected by the simple TL model. The structure is sophisticated, and thus the simple TL model gives only a general idea in such cases.

After that, L is increased to $L = 2.5$ cm, and the problem is solved only using the hybrid method because the application of edge elements method alone is not possible for this case as discussed earlier in this Chapter. Since

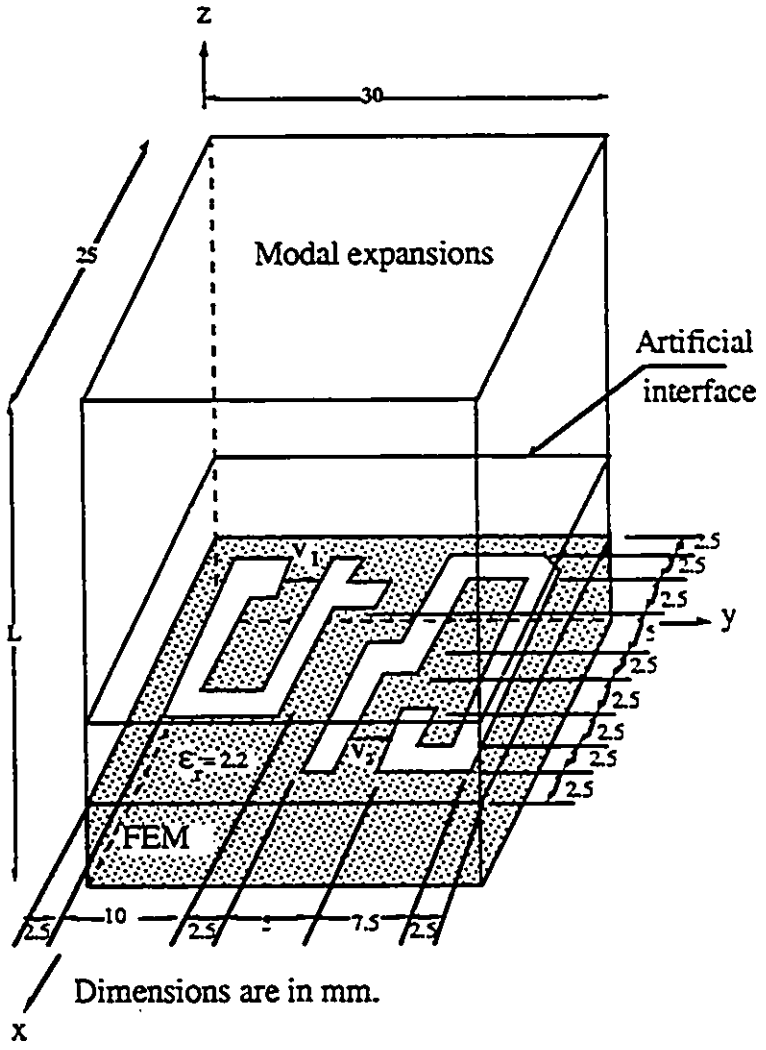

Figure 5.12: Two loops on dielectric board in metal housing.

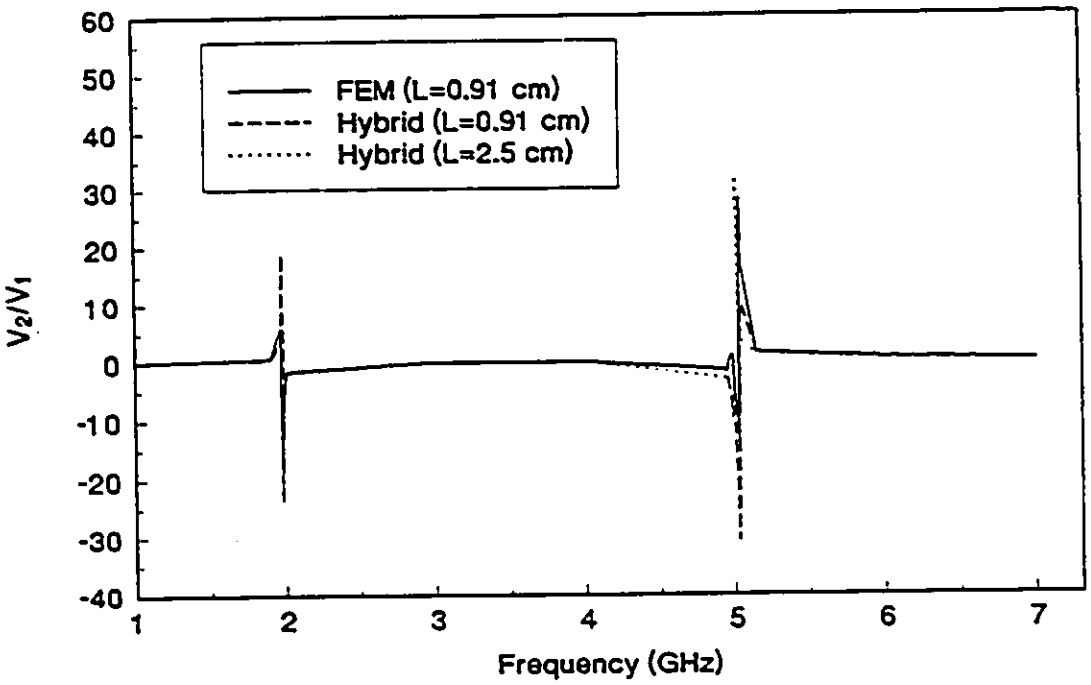

Figure 5.13: Cross-talk in the "Two Loops" example.

the resonances below 7 GHz are not related to the shield, increasing shield height to $L = 2.5$ cm has a minor effect on the results. The effect is slightly reducing the second resonant frequency as Fig. 5.13 shows.

It could be helpful to describe the discretization used for this example. The volume below the artificial interface, see Fig. 5.12, is divided into two layers of tetrahedrons; one layer representing the substrate and the other layer representing the rest of this volume. The space division is 2.5 mm in the x and y directions. Same discretization scheme is used for the edge elements method.

- Planar Transmission Lines (Microstrips)

Presented in this article are three examples. The field distribution of the first example, and the cross-talk of the second example are computed by both the edge elements and the hybrid methods. Comparing the results reveals good agreement between the two solutions. The cross-talk in the third example is solved by the hybrid method. The three examples are

1. Single Transmission Line

   Fig. 5.14 illustrates a planar TL on dielectric substrate placed in a metal enclosure. An artificial interface, for the hybrid method, is introduced at $z = 7$ mm, see Fig. 5.14, and the region under which is discretized into tetrahedral edge elements. The mesh used is uniform and has a space division of 3.5 mm. The field distribution is computed using the hybrid method. On the other hand, the application of the edge elements method requires the discretization of the whole structure. Using a uniform mesh of 3.5 mm space division, the total number of edge variables is 2065 compared to 644 total number of edges required by the hybrid method. The field distributions obtained by the two methods at $z = 1.75$ mm and $f = 5$ GHz are plotted in Fig. 5.15.

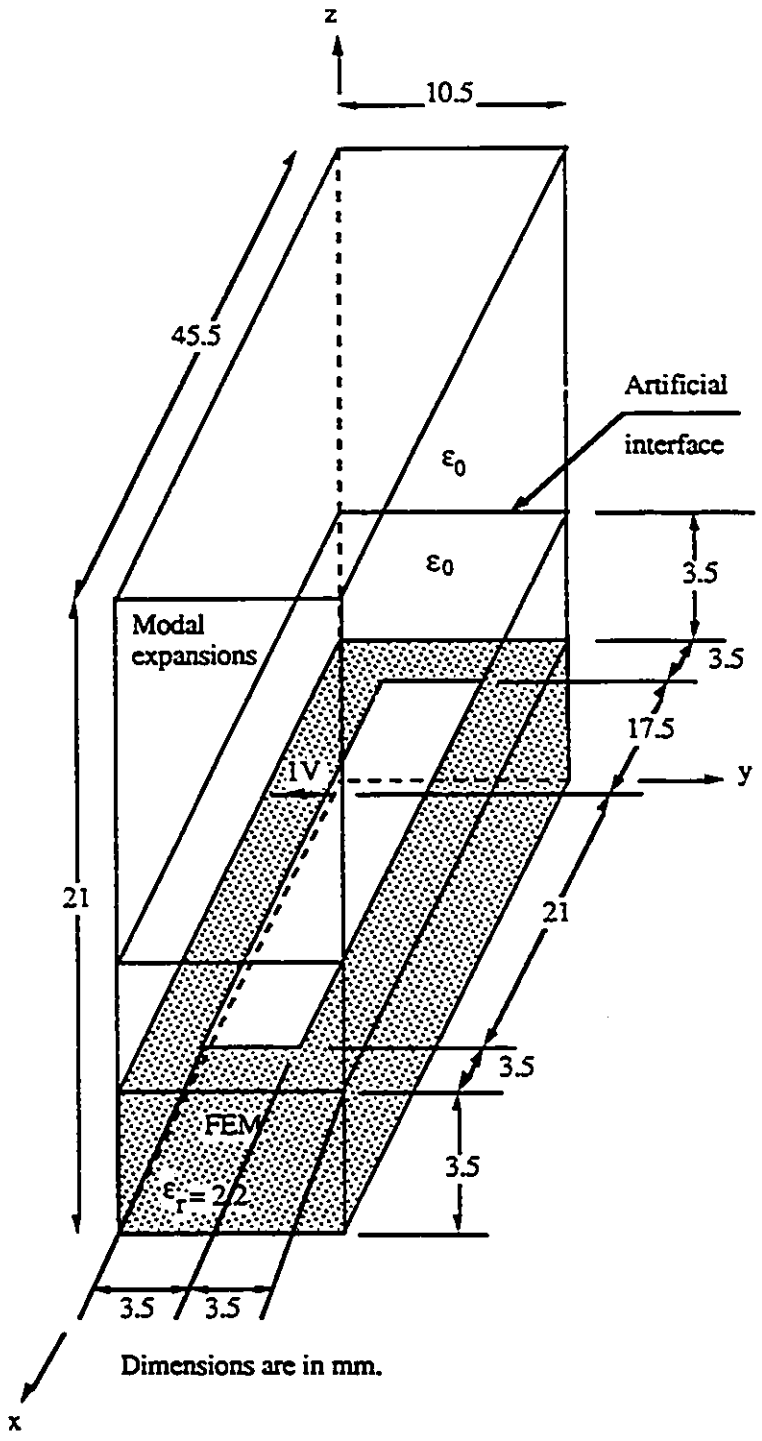

Figure 5.14: Planar transmission line inside enclosure modeled by the hybrid method.

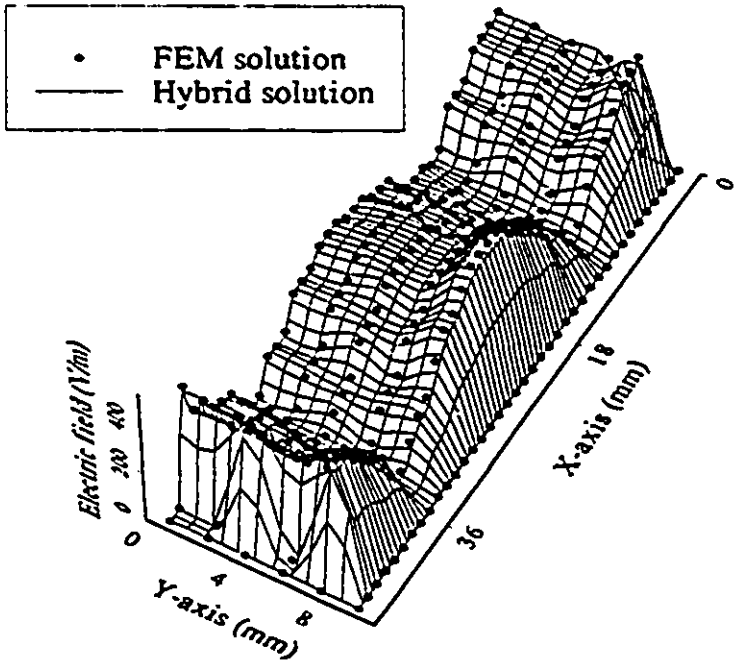

Figure 5.15: Total electric field distributions of the "Single Transmission Line" example.

2. Cross-Talk between Two Terminated TL's Embedded in Dielectric Substrate

   This problem consists of two planar TL's embedded in dielectric substrate, and terminated in 50 Ω resistive loads as in Fig. 5.16. The region below the artificial interface is represented by a tetrahedral mesh. The space division is 2.5 mm except in the substrate where the space division is 1.6 mm in the z direction. Each resistor is modeled by one brick at the input terminals of the TL. This brick has conductivity σ that gives the value of the resistor 50 Ω.

   According to the EMC terminology, the TL containing the source (excitation) is called the "generator circuit", the other victim TL is termed the "receptor circuit", and the shield is the "reference conductor". Also, the voltage induced in the receptor circuit at the input terminals near the source is denoted by the "near-end cross-talk", whereas the voltage induced in the receptor circuit at the input terminals away from the source is termed the "far-end cross-talk".

   Frequency responses of the near-end and far-end cross-talk are computed by both the edge elements and hybrid methods. The maximum relative difference between the two solutions is less than 1.5 % , refer to Fig. 5.17.

3. Cross-Talk between Two Un-Loaded TL's

   Fig. 5.18 illustrates two parallel tracks (planar TL's) on Duroid substrate, $\epsilon_r = 2.2$, in a metal enclosure representing the circuit package. The problem domain (the volume below the artificial interface) is modeled by a uniform mesh of 2.5 mm space division except in the substrate where the space division in the z direction is 1.5748 mm. The near-end and far-end cross-talk are computed for two values of track width, in Fig. 5.18 $TW = 5$ mm and $TW = 2.5$ mm, by the hybrid method. The results are shown in Fig. 5.19 (a) and (b).

   The first resonance of the enclosure, without the circuit, is at $f = 7.8$ GHz.

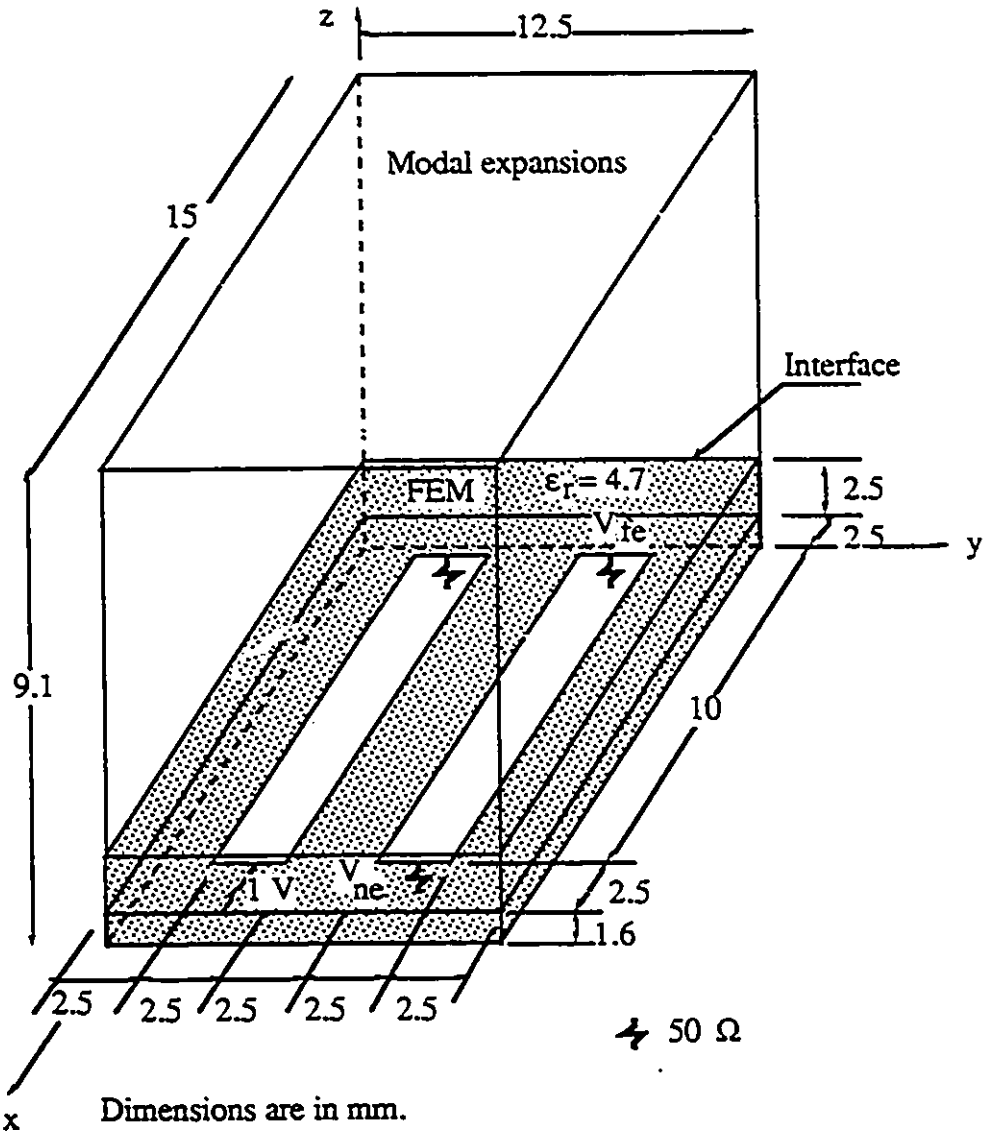

Figure 5.16: Two loaded planar TL's embedded in dielectric substrate.

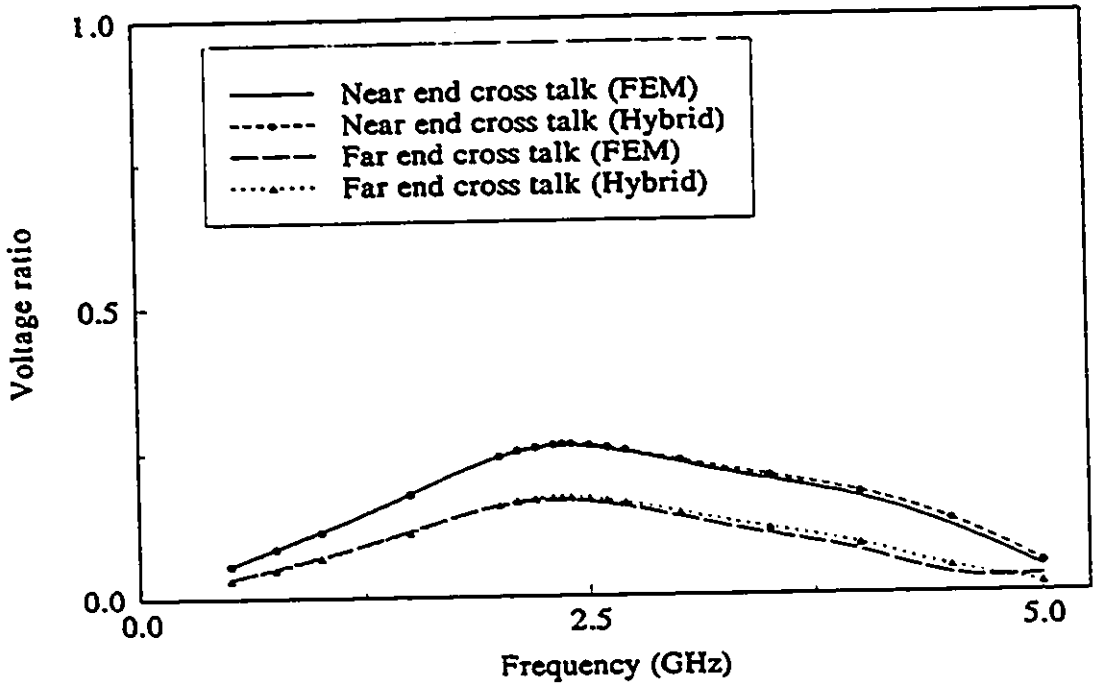

Figure 5.17: Frequency response of the cross-talk in the circuit of example "Two Terminated TL's Embedded in Dielectric Substrate".

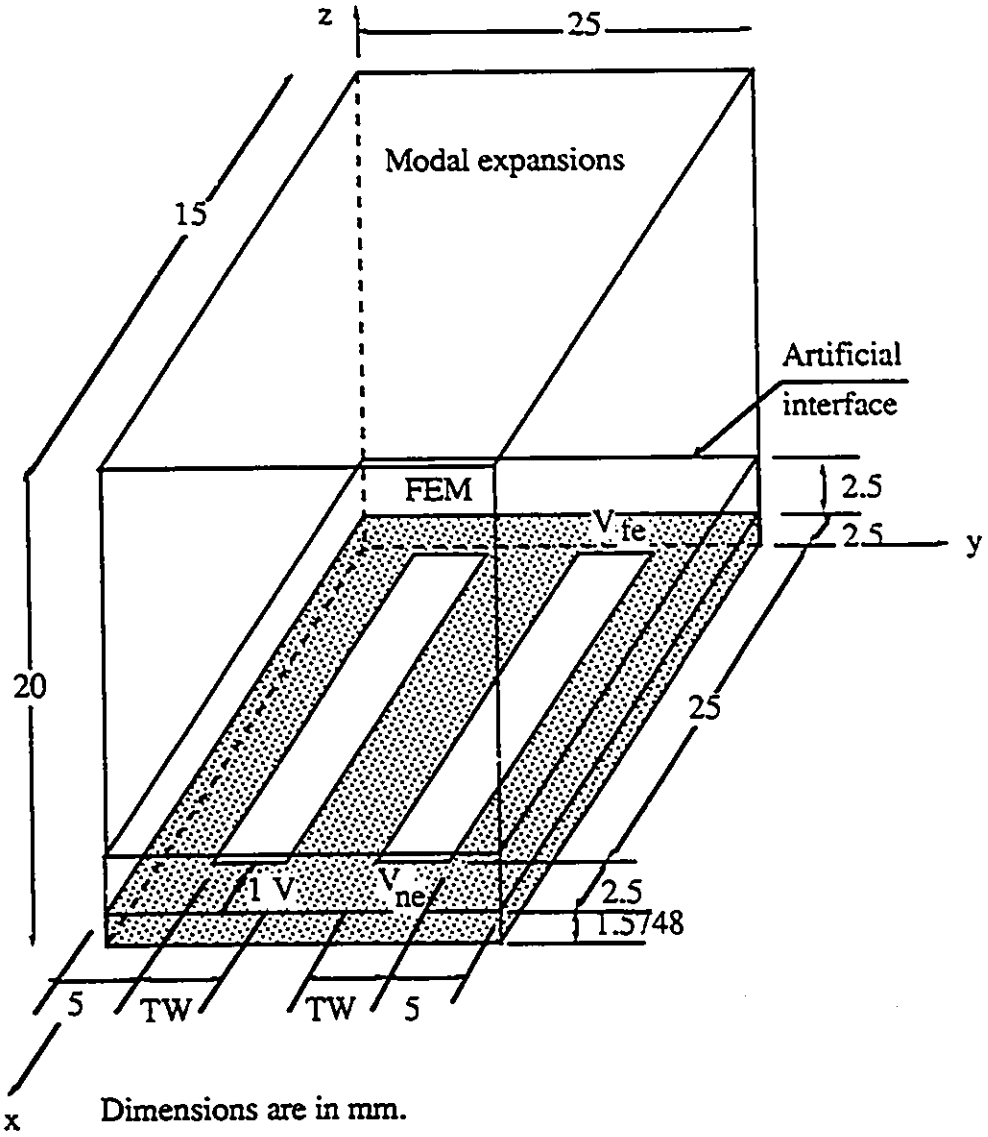

Figure 5.18: Two unloaded TL's on Duroid substrate, $\epsilon_r = 2.2$.

Figure 5.19: Cross-talk levels - (a) and (b) - in the circuit of the "Two Un-Loaded TL's" example.

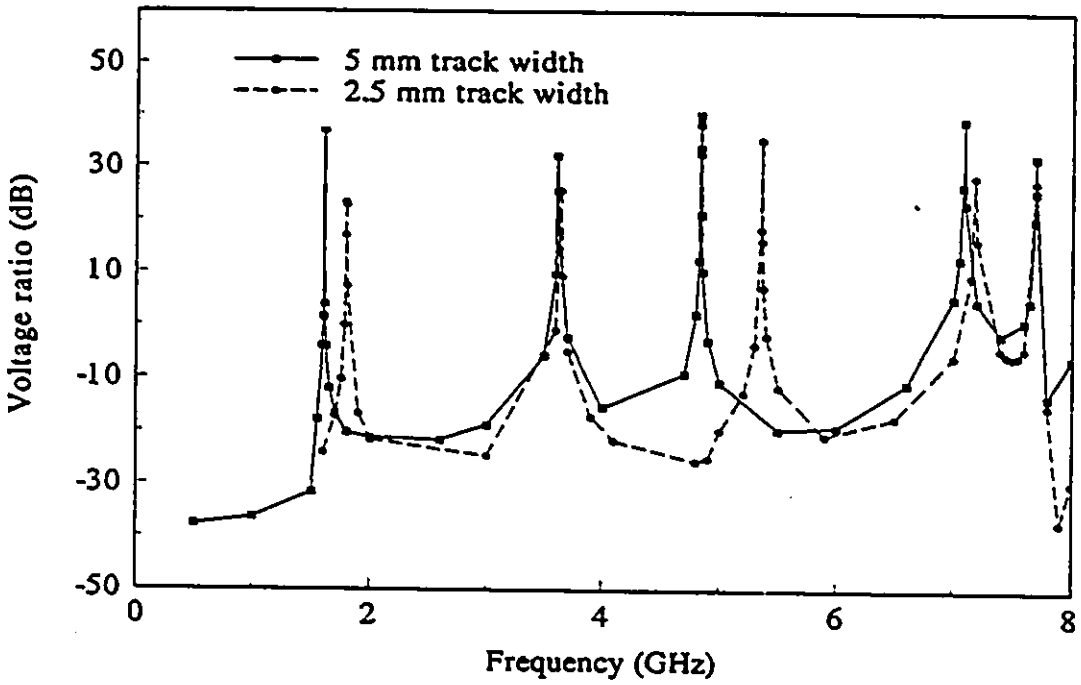

Figure 5.19: (a) Near-end cross-talk

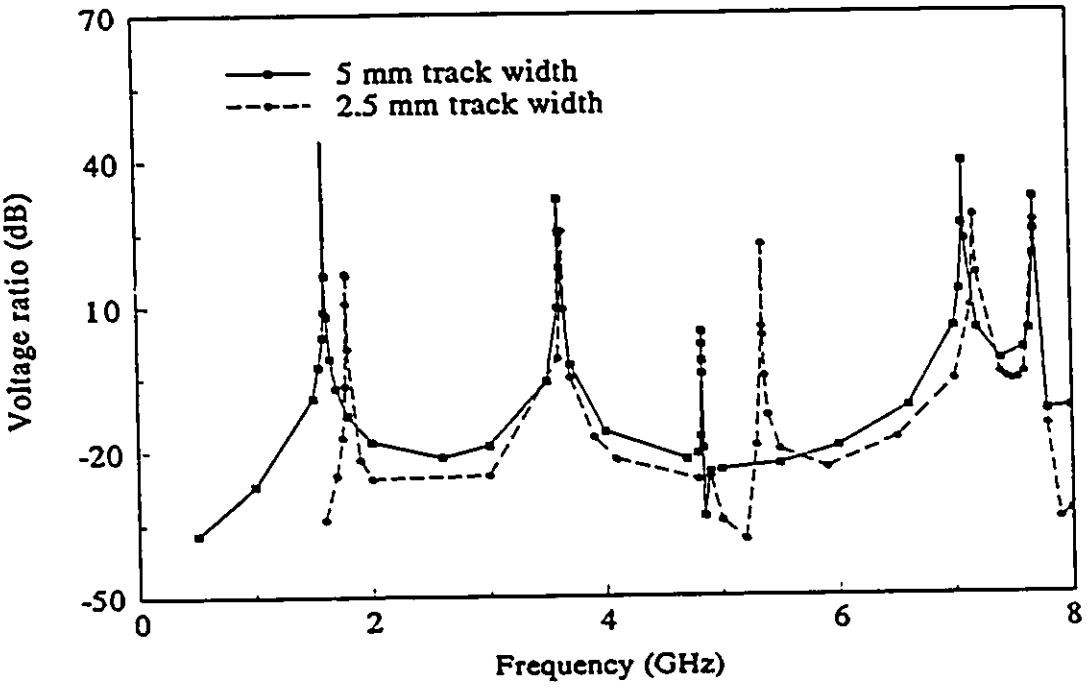

Figure 5.19: (b) Far-end cross-talk

The numerical value is 7.7 GHz, see Fig. 5.19. The shift in the resonant frequency of 0.1 GHz is due to the existence of the inhomogeneity (the circuit) inside the enclosure. The other four resonances shown in the figure are due to the open-circuited TL (unloaded track) . To get a general idea, let us compute these four resonances using the empirical formula

$$f_{resonance}(GHz) = \frac{0.3}{4\sqrt{\epsilon_r}\mathcal{L}}p,\ p = 1, 2, \ldots \tag{5.41}$$

where $\mathcal{L}$ is the length of the open-circuited TL, 30 cm, and $\epsilon_r = 2.2$. From this formula, the first four resonances are: 1.7, 3.4, 5.1, and 6.7 GHz. A good correlation is seen between these values and the numerical results shown in Fig. 5.19 (a) and (b). Also, note that values of the resonant frequencies are higher for the smaller track width $TW = 2.5$ mm; this is reasonable since the effective dielectric constant decreases as the track width is reduced. Observe in addition that the enclosure resonant frequency $f = 7.7$ GHz did not change when the track width was adjusted; this makes sense because this resonance is mainly related to the enclosure.

- Experimental Results

In order to verify the hybrid solutions where the edge element method is not applicable, an experiment was made. The experiment is illustrated in Fig. 5.20. It is composed of two parallel tracks terminated in 50 Ω loads. The tracks are on top of RT/duroid 5880 substrate with $\epsilon_r = 2.2$ and thickness 0.062" = 1.5748 mm. The entire circuit is placed in a metal enclosure as shown in Fig. 5.20 (a). The enclosure was made of brass, and the tracks were cut from a copper foil and pasted on top of the substrate. The lid is removed to visualize the circuit as shown in Fig. 5.20 (b). Twenty four screws were used around the lid to maintain electrical continuity across the joint and prevent forming a slot antenna. Alternatively, a conductive gasket could have been used. To preserve the effectiveness of the shield, square coaxial connectors of type-code $23SMA-$

$50 - 0 - 53$ were peripherally bonded to the enclosure as shown in Fig. 5.20 (b). A photograph of a coaxial connector is shown in Fig. 5.21. The lumped resistors used were micro-wave chip resistors with part number P/N: Sc0014M, 50 Ω 1%. Fig. 5.22 shows a photograph of the resistor. Due to technical difficulties, it was not possible to solder the resistors to the shield. These resistors were soldered to the tracks ends on one side and connected to the shield via a small copper foil on the other side.

Vector voltmeter, to measure the cross-talk voltage in the circuit shown in Fig. 5.20, was not available. Instead, the *hp* 8510B network analyzer was used, see Fig. 5.20 (c), to measure the transmission coefficient. The transmission coefficient is equal to the far-end cross-talk, with normalized excitation to unity, provided that the tracks are matched to their loads. For that reason, the track width was chosen so that the characteristic impedance of the line is approximately equal to the load value 50 Ω. This choice was based on design curves for microstrip TL's. These design curves do not take into account the coupling between adjacent microstrips and the effect of the enclosure. The dimensions of the enclosure were chosen such that the computer storage requirement is not exceeded over the frequency range up to 5 GHz. In fact, later on the measurements were carried on to 8 GHz to see the first resonance of the enclosure.

To model accurately the problem illustrated in Fig. 5.20, an adaptive mesh generator is needed which generates a refined mesh near field discontinuities and small objects, and coarse mesh where the field variation is expected to be slow. Unfortunately, such mesh generator is not available to our research group. In consequence to that, some aspects of the problem are not represented properly by the mesh used. For example each of the lumped resistors is modeled by two adjacent bricks with size $5 \times 2.5 \times 1.5748\ mm^3$. This approximation reduces the track length. Thus the actual track is modeled by a slightly shorter track. Also the metal box is assumed completely sealed, i.e., the cable penetrations are not taken into account. The excitation is modeled by Dirichlet boundary condition.

Figure 5.20: An experiment consisting of two terminated signal tracks on Duroid substrate, $\epsilon_r = 2.2$, in metal housing.

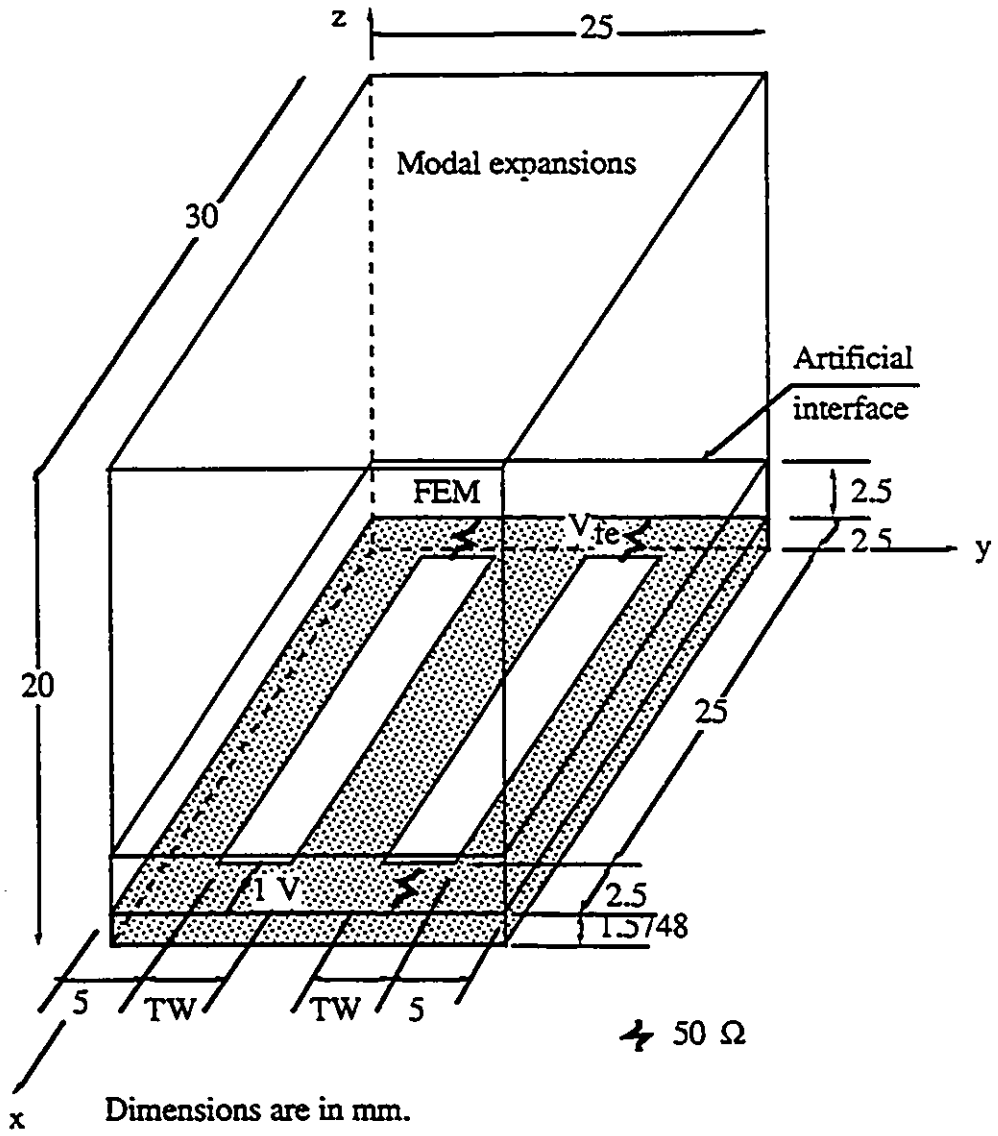

Figure 5.20: (a) Schematic of the device to be tested

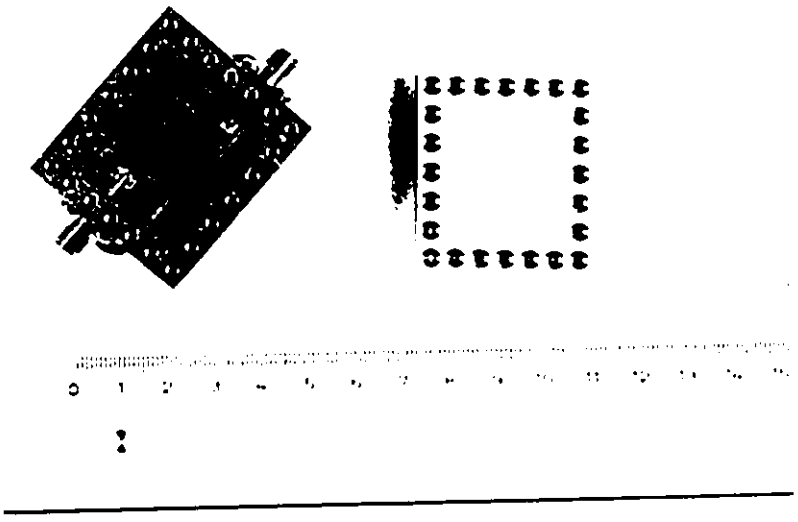

Figure 5.20: (b) Photograph of the device tested

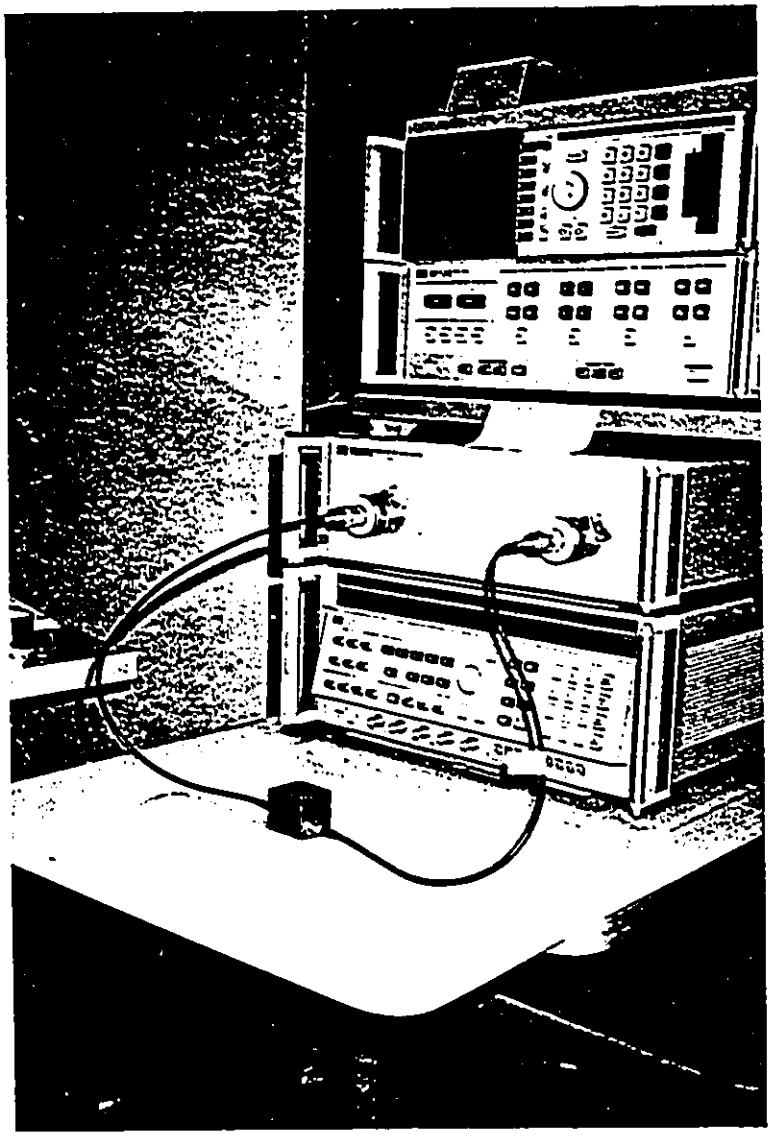

Figure 5.20: (c) Photograph of the experimental setup

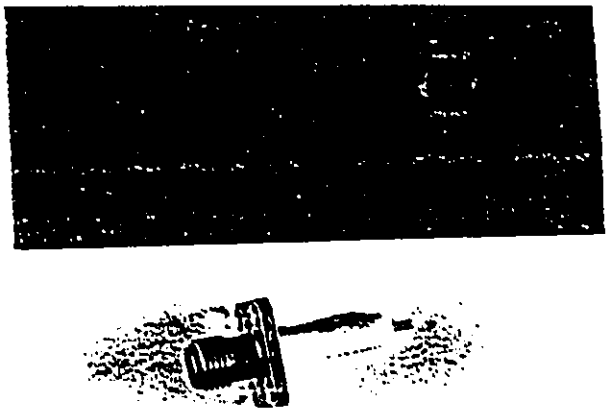

Figure 5.21: Photograph of the square coaxial connector.

Figure 5.22: Photograph of the microwave chip resistor.

These differences between the actual device tested and its finite elements model are expected to affect the agreement between the computed and measured results especially at the higher frequencies.

The predicted and experimental results are within 2 dB up to 3.8 GHz as plotted in Fig. 5.23. Between 3.8 GHz and 6 GHz, the numerical solution is a bit shifted to the right. This is explained by the fact that the actual TL is modeled by a shorter TL; the longer TL at frequency f is equivalent to the shorter TL at frequency $f + \Delta f$. To see why this shift starts to appear after 3.8 GHz, let us compute approximately the difference in terms of the wavelength between the actual and model TL's. The space division of the mesh used is 2.5 mm in the x and y directions. Thus the length difference for the generator circuit is 2.5 mm, and 5 mm for the receptor circuit. Note that the generator circuit has one resistor while the receptor circuit has two resistors. These difference in terms of the wave-length at $f = 3.8$ GHz are

$$2.5mm \longrightarrow \frac{2.5}{\lambda_0\sqrt{\epsilon_r}} = 0.05\lambda$$

$$5\ mm \longrightarrow \frac{5}{\lambda_0\sqrt{\epsilon_r}} = 0.1\lambda$$

Therefore, these differences start to affect the results when it become comparable to 0.1 λ. This simple result is consistent with one of the most fundamental principles of the FEM: a space division will be "seen" by the electromagnetic wave if it is greater than 0.1 λ.

Lastly, the resonant frequency 7.7 GHz is accurately predicted since this frequency is mainly related to the shield dimensions. However, the predicted levels of the cross-talk are higher than the measured levels. This is due to that the cable penetrations into the shield, which cause energy leakage, were not taken into account. The diameter of each cable penetration was 4.3 mm. Note that

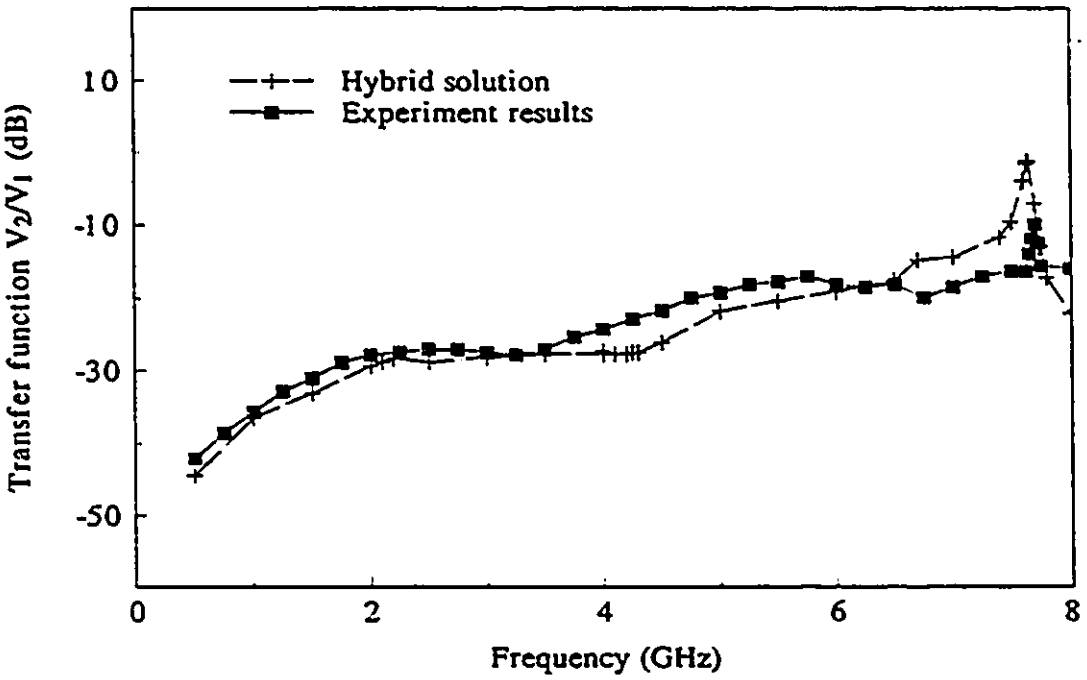

Figure 5.23: Experimental and computed far-end cross-talk transfer function of the experiment described in this Article.

4.3 mm at 7.7 GHz is 0.16 λ. In addition, the conductors in the model are assumed perfect, and the track thickness is assumed zero, the resistor size in the model is much larger than the actual size in the experiment. Furthermore, the TL's might not be matched at all frequencies in addition to the reflections at the cable entries into the enclosure. Another factor that contributes to the error in this band is that the maximum edge length of the finite element mesh in the substrate is larger than 0.1 λ (0.15 λ at 8 GHz). Overall, the agreement between the numerical and experimental results is reasonable.

5.8 CONCLUSIONS

Three dimensional hybrid numerical method has been proposed in this Chapter. The method couples the edge-based FEM solution to the analytical solutions of a homogeneous arbitrary large housing with aperture. The coupling has been effected via the continuity conditions at the aperture. The validity and accuracy of the formulation have been shown by comparing the hybrid solutions to other published data, the pure edge-based FEM solutions, and analytical solutions. In addition, an experiment was made. There are unavoidable differences between the finite elements model and the actual device due to the unavailability of adaptive mesh generator. Also, a vector voltmeter to measure the cross talk voltage was not available. Instead, the network analyzer was used to measure the transmission coefficient which is equivalent to the frequency response of the cross-talk only if the transmission lines are matched to their loads. Keeping these considerations in mind, the experimental results have demonstrated the validity and usefulness of the proposed method.

An advantage of the hybrid method is that it employs the edge-based FEM which is not expected to produce spurious modes. Further, the hybrid significantly reduces the number of equations needing solution compared to the edge-based FEM.

Chapter 6

Conclusions

The use of the finite element method has rapidly increased during the past several years due to its capability of tackling strongly complex problems with arbitrary boundaries. Further, the solution for inhomogeneous problems can be obtained without essentially changing the solution algorithm. In addition, different types of finite elements are available, e.g., linear, curvilinear, and higher order elements on tetrahedron, brick, triangle, or rectangle. Also, nonlinear problems related to the saturation phenomenon in magnetic materials can be handled by the FEM. Thus the constituent properties of the material are described by either a scalar quantity (isotropic), or tensor (anisotropic), or nonlinear plot between the electric field and polarization vector or between the magnetic field and flux density. The final matrix produced is sparse which is one of the most desired properties of the finite element method where efficient algorithms for reducing the computer storage demand can be employed.

On the other hand, the node-based (the degrees of freedom are associated with the nodes of the mesh) finite element method suffers from a serious drawback, namely, the occurrence of spurious modes or the nonphysical eigenvalue solutions. Even if the device is excited by known, non-zero boundary conditions, the quality of the solution will be determined in part by the eigensolutions of the governing equation [87].

The problem of spurious modes seems to have been overcome by the construction

of new brand of the finite element method referred to as the edge-based finite element method. The degrees of freedom of the edge-based finite element method (briefly, edge elements method) are associated with the tangential components of the field variable along the mesh edges. Additional advantages of the edge elements method are allowing for the discontinuity of the normal component of the field across material interfaces, and being better at handling field singularities [88]. The edge element method produces larger number of equations than the node-based finite element method. However, the edge elements method matrix is more sparse such that less computer storage is needed compared to the node-based FEM matrix [73]. It is to be noted here that not only edge elements are available, also facet elements (the unknowns are related to the normal components of the flux across the element facets) and volume elements (the unknowns are related to the volume of the element) are available [73].

In order to use these edge elements for open boundary problems (e.g., radar scattering computations, radiation from electronic devices, and penetration into complex shielded enclosures), the finite element mesh must be terminated by a proper boundary condition. This boundary condition is either global (hybrid methods) or local (ABC: Absorbing Boundary Condition). The hybrid numerical methods are more accurate than ABC methods since the former use exact boundary conditions while the latter use approximate boundary conditions. The price of this accuracy is affecting the sparsity of the FEM matrix and requiring matrix inversion in general which limits the application of the hybrid methods to small size problems in terms of the wavelength. The ABC methods produce sparse matrices and thus require less computer storage. However, since the ABC is approximate, the mesh must extend a significant distance away from the geometry of interest in order to obtain an accurate solution. As the discretization error increases with the mesh size, this has serious implications on the ABC methods [84]. These limitations of both ABC and hybrid methods are resolved in this thesis by using the edge elements method which is free from the adverse effects of spurious modes, and proposing formulation for a new hybrid method that preserves

the sparsity of the matrix.

In this thesis, the 2D edge elements solution [75] is combined with an asymptotic expansion of the field scattered from an inhomogeneous object (representing an electronic device for example). The combination produces local boundary condition and thus the solution is approximate. The solution preserves the sparsity and symmetry of the matrix. Comparisons with other numerical and analytical solutions show the validity and usefulness of the formulation presented. Unexpectedly, very good results are obtained when the truncating boundary is placed fraction of wavelength from the the scatterer. This of course reduces the number of unknowns and improves the accuracy of the results since the discretization error increases with the electrical size of the mesh [84]. Obtaining good results with the truncating boundary placed fraction of wavelength from the surface of the scatterer might be explained as follows. The edge elements solution does not produce spurious modes, and therefore less error propagation is expected between the truncating boundary and the body.

It has been noticed that calculations performed for frequencies near the resonant frequencies of a closed structure required more CPU time to achieve the same error criterion, refer to Chapter 4. This indicates that the system matrix becomes ill-conditioned for frequencies closer to the resonant values.

A 3D hybrid numerical method is presented in this thesis. This hybrid method, unlike most of the other hybrid methods, produces sparse matrix and does not need any matrix inversion. It combines the analytical solution of part of the problem with the edge elements solution of the inhomogeneous part. This method is mainly useful for the analysis and design of packed printed circuit boards. The circuit package is represented by metal enclosure most of it is empty except for the substrate which comprises only a small portion of the whole volume. Consequently, the number of unknowns needing solution is significantly reduced. Also, the accuracy of the solution is enhanced since only the inhomogeneous part of the problem is discretized. The hybrid solutions are compared to analytical solutions, other numerical published data, and the pure edge-

based finite element method solution. The comparisons demonstrate the validity and accuracy of the proposed method. Also, an experiment was performed and the results compare favorably with the hybrid solution.

Bibliography

[1] P. A. Raviart and J. M. Thomas, *Primal hybrid finite element methods for 2nd order elliptic equations*, Math. Comp., Vol. 31, No. 138, pp. 391-413, April 1977.

[2] J. C. Nedelec, *Mixed finite elements in R3*, Numer. Math., Vol. 35, p. 315, 1980.

[3] A. Bossavit and J. C. Verite, *A mixed FEM-BIEM method to solve 3-D eddy-current problems*, IEEE Trans. Magn., Vol. 18, No. 2, pp. 431-435, 1982.

[4] A. Bossavit and J. C. Verite, *The 'TRIFOU' code: solving the 3-D eddy-currents problem by using H as state variable*, IEEE Trans. Magn., Vol. 19, No. 6, pp. 2465-2470, 1983.

[5] M. Hano, *Finite-element analysis of dielectic-loaded waveguides*, IEEE Trans. MTT., Vol. 32, No. 10, pp. 1275-1279, Oct. 1984.

[6] J. S. van Welij, *Calculation of eddy currents in terms of H on hexahedra*, IEEE Trans. Magn., Vol. 21, No. 6, pp. 2239-2241, Nov. 1985.

[7] Gerrit Mur and Adrianus T. de Hoop, *A finite-element method for computing three-dimensional electromagnetic fields in inhomogencous media*, IEEE Trans. Magnetics, Vol. 21, no. 6, pp. 2188-2191, Nov. 1985.

[8] M. L. Barton and Z. J. Cendes, *New vector finite elements for three-dimensional magnetic field computation*, J. Appl. Phys., Vol. 61, No. 8, pp. 3919-3921, April 1987.

[9] A. Bossavit, *Whitney forms: a class of finite elements for three-dimensional computations in electromagnetism*, IEE Proc., Vol. 135, Pt. A, No. 8, pp. 493-500, Nov. 1988.

[10] C. W. Crowley, P. P. Silvester, and H. Hurwitz, *Covariant projection elements for 3D vector field problems* , IEEE Trans. Magnetics, Vol. 24, no. 1, pp. 397-400, Jan. 1988.

[11] J. F. Lee, *Analysis of passive microwave devices by using three-dimensional tangential vector finite elements*, International Journal of Numerical Modelling: Electronic Networks, Devices and Fields, Vol. 3, No. 4, pp. 235-246, Dec. 1990.

[12] J. P. Webb and B. Forghani, *Hierarchal scalar and vector tetrahedra*, IEEE Trans. Magnetics, Vol. 29, no. 2, pp. 1495-1498, March 1993.

[13] J. S. Wang and N. Ida, *Curvilinear and higher order edge finite elements in electromagnetic field computation*, IEEE Trans. Magnetics, Vol. 29, no. 2, pp. 1491-1494, March 1993.

[I] **Hybrid methods combining an asymptotic expansion with a numerical method**

[] *MoM/GTD*

[] *Electric field approach*

[14] G. A. Thiele and T. H. Newhouse, *A hybrid technique for combining moment methods with the geometrical theory of diffraction*, IEEE Trans. Antennas Propag., Vol. 23, no. 1, pp. 62-69, Jan. 1975

[15] W. D. Burnside and T. Chu, *Airborne antenna pattern code user's manual*, Report 711679-2, The Ohio State University ElectroScience Lab.; prepared under contract F30602-C-0068, Mar. 1980

[16] G. A. Thiele and G. K. Chan, *Application of the hybrid technique to time domain problems*, IEEE Trans. Antennas Propag.,Vol. 26, no. 1, Jan. 1978

[17] E. P. Ekelman,Jr., *A hybrid technique for combining the moment method treatment of wire antennas with the GTD for curved surfaces*, Ph.D. Dissertation, The Ohio State University, 1978

[18] L. W. Henderson and G. A. Thiele, *A hybrid MOM-GTD technique for the treatment of wire antennas mounted on or near a curved surface*, presented at the XX General Assembly of URSI; Munich, Germany, Aug.1980

[19] A. Davidson and G. A. Thiele, *A hybrid method of moments-GTD technique for computing electromagnetic coupling between two monopole antennas on a large cylindrical surface*, presented at the XX General Assembly of URSI; Munich, Germany, Aug.1980

[] *Current approach*

[20] P. H. Pathak, *An asymptotic analysis of the scattering of plane waves by a smooth convex cylinder*, Radio Sci., Vol. 14, pp.419-435, 1979

[21] R. Mittra and S. Safavi-Naini, *Source radiation in presence of scattering of smooth convex bodies*, Radio Sci., Vol. 14, pp.217-237, 1979.

[22] W. D. Burnside, C. L. Yu and R. J. Marhefka, *A technique to combine the geometrical theory of diffraction and the moment method*, IEEE Trans. Antennas Propag., Vol. 23, no. 4, pp. 551-557, July 1975

[23] E. K. Miller, L. Medgyesi-Mitschang and E. H. Newman, *Computational Electromagnetics: Frequency-Domain Method of Moments*,IEEE press, Part 6, New York, 1992

[24] J. Sahalos and G. A. Thiele, *An improved formulation for extending the geometrical theory of diffraction by the moment method* , Report 4372-2, The Ohio State

University ElectroScience Lab.; prepared under contract N00014-76-C-0573, May 1977

[25] S. Lee, *Control of electromagnetic scattering by antenna impedance Loading*, Report 3424-2, The Ohio State University ElectroScience Lab.; Dept. of Electrical Engineering; prepared under contract F19628-72-C-0202, (AFCRL-TR-74-0426), July 1974

[26] J. A. Aas, *Control of electromagnetic scattering from wing profiles by impedance loading*,Report 3424-4, The Ohio State University ElectroScience Lab.; Dept. of Electrical Engineering; prepared under contract F19628-72-C-0202 , (AFCRL-TR-75-0463), Aug. 1975

[27] C. W. Chuang and W. D. Burnside, *A diffraction coefficient for a cylindrically truncated planar structure*, IEEE Trans. Antennas Propag., Vol. 28, no. 2, Mar. 1980

[] *MoM combined with quasi-static techniques*

[28] R. G. Olsen, G. L. Hower and P. D. Mannikko, *A hybrid method for combining quasi-static and full-wave techniques for electromagnetic scattering problems*,IEEE Trans. Antennas Propag., Vol. 36, pp. 1180-1184, Aug. 1988

[29] R. G. Olsen and P. D. Mannikko, *Validation of the hybrid quasi-static/full-wave method for capacitively loaded thin-wire antennas* ,IEEE Trans. Antennas Propag., Vol. 38, no. 4, pp. 516-522, Apr. 1990

[30] P. D. Mannikko, *Implementation of a full-wave/quasi-static hybrid method for analysis of axially symmetric thin-wire antennas with capacitive loads*, M. S. thesis, Washington State University, Pullman, 1988

[*II*] **Hybrid methods incorporating an analytical solution into a numerical method**

[] *MoM/Green's function*

[31] F. M. Tesche and A. R. Neureuther, *Radiation patterns for two monopoles on a perfectly conducting sphere*, IEEE Trans. Antennas Propag., Vol. 18, pp. 692-94, Sept. 1970

[32] J. R. Mosig and F. E. Gardiol, *General integral equation formulation for microstrip antennas and scatterers*, IEE Proc., Vol. 132, Pt. H, no. 7, pp.424-432, Dec. 1985

[33] R. F. Harrington, *Field Computation by Moment Methods*, Krieger Publishing Co., Malabar, Florida, 1982

[34] G. J. Burke and E. K. Miller, *Modelling antennas near to and penetrating a lossy interface*, IEEE Trans. Antennas Ppopagat., Vol. 32, no. 10, pp.1040-1049, Oct. 1984

[35] D. R. Jackson and N. G. Alexópoulos, *Analysis of planar strip geometries in a substrate-superstrate configuration*, IEEE Trans. Antennas Propagat., Vol. 34, no. 12, pp.1430-1438, Dec. 1986

[*III*] **Hybrid methods combining different numerical techniques**

[] *MoM combined with finite methods*

[Case *I*] *Plane Wave Excitation*

[36] J. Jin, and V. Liepa, *A note on hybrid finite element method for solving scattering problems*, IEEE Trans. Antennas Prpoagat., Vol. 36, no. 10, pp.1486-1490, Oct. 1988

[37] J. Jin, and J. L. Volakis, *A hybrid finite element method for scattering and radiation by microstrip patch antennas and arrays residing in a cavity*, IEEE Trans. Antennas Prpoagat., Vol. 39, no. 11, pp.1598-1604, Nov. 1991

[38] P. Silvester, and M. S. Hsieh, *Finite-element solution of 2-dimensional exterior field problems*, Proc. Inst. Elec. Eng., Vol. 118, pp.1743-1747, Dec. 1971

[39] B. H. McDonald and A. Wexler, *Finite-element solution of unbounded field problems*, IEEE Trans. Microwave Theory Tech., Vol. MTT-20, pp.841-847, Dec. 1972

[40] S. P. Marin, *Computing scattering amplitudes for arbitrary cylinders under incident plane waves*, IEEE Trans. Antennas Prpoagat., Vol. 30, pp.1045-1049, Nov. 1982

[41] S. K. Jing and C. H. Chen, *On variational electromagnetics: Theory and application*, IEEE Trans. Antennas Prpoagat., Vol. 32, pp.902-907, Sept. 1984

[42] S. Washisu, I. Fukai and M. Suzuki, *Extension of finite-element method to unbounded field problems*, Electron. Lett., Vol. 15, pp.772-774, 1979

[43] B. H. McDonald and A. Wexler, *Finite Element in Electrical and Magnetic Field Problem*, M. V. K. Chari and P. P. Silvester, Eds. London and New York , Wiley, 1980, Chap. 9

[44] T. Orikasa, S. Washisu, T. Honma and I. Fukai, *Finite element method for unbounded field problems and application to two-dimensional taper*, Int. J. Num. Meth. Eng., Vol. 19, pp.157-168, 1983

[45] Y. N. Guo, *Finite-element solution of electromagnetic scattering from inhomogeneous dielectric cylinder with arbitrary cross section*, M. S. thesis, Nanjing Univ., 1985

[46] J. M. Jin and V. V. Liepa, *Application of hybrid finite element method to electromagnetic scattering from coated cylinders*, IEEE Trans. Antennas Prpoagat., Vol. 36, pp.55-70, Jan. 1988

[47] R. F. Harrington, *Time-Harmonic Electromagnetic Fields*, New York, McGraw-Hill, 1961

[48] X. Yuan, *Three-dimensional electromagnetic scattering from inhomogeneous objects by the hybrid moment and finite element method*, IEEE Trans. MTT, Vol. 38, no. 8, pp.1053-1058, Aug. 1990

[49] X. Yuan, D. R. Lynch, and J. W. Strohbehn, *Coupling of finite element and moment methods for electromagnetic scattering from inhomogeneous objects*, IEEE Trans. Antennas Prpoagat., Vol. 38, no. 3, pp.386-393, Mar. 1990

[50] S. D. Gedney, J. F. Lee and R. Mittra, *A combined FEM/MoM approach to analyze the plane wave diffraction by arbitrary gratings*, IEEE Trans. MTT, Vol. 40, no. 2, pp.363-370, Feb. 1992

[51] S. D. Gedney, *Solution of open region electromagnetic scattering problems on hypercube multiprocessors*, Ph.D. dissertation, University of Illinois, Urbana, IL, 1991

[52] M. A. Morgan and B. E. Welch, *The field feedback formulation for electromagnetic scattering computations*, IEEE Trans. Antennas Prpoagat., Vol. 34, No. 12, pp.1377-1382, Dec. 1986

[53] Jian-Ming Jin and J. L. Volakis, *A finite element-boundary integral formulation for scattering by three-dimensional cavity backed apertures*, IEEE Trans. Antennas Prpoagat., Vol. 39, no. 1, pp.97-104, Jan. 1991

[54] Jian-Ming Jin and J. L. Volakis, *Electromagnetic scattering by and transmission through a three-dimensional slot in a thick conducting plane*, IEEE Trans. Antennas Prpoagat., Vol. 39, no. 4, pp.543-550, Apr. 1991

[55] J.-M. Jin and J. L. Volakis, *New techniques for characterizing diffraction by inhomogeneously filled slots of arbitrary cross-section in thick conducting plates*, Inst. Elec. Eng. Electron Lett., Vol. 25, no. 17, pp.1121-1123, Aug. 1989

[56] J.-M. Jin and J. L. Volakis, *TM scattering by an inhomogeneously filled aperture in a thick conducting plane*, Inst. Elec. Eng. Proc., Vol. 137, pt. H, pp.153-159, June 1990

[57] S. K. Jeng, *Scattering from a cavity-backed slit in a ground plane-TE case*, IEEE Trans. Antennas Prpoagat., Vol. 38, pp.1523-1529, Oct. 1990

[58] A. Taflove and K. Umashankar, *A hybrid moment method/finite-difference time domain approach to electromagnetic coupling and aperture penetration into complex geometries*, IEEE Trans. Antennas Prpoagat., Vol. 30, no. 4, pp.617-627,1982

[59] H. K. Schumann and D. E. Warren, *Aperture coupling in bodies of revolution*, IEEE Trans. Antennas Prpoagat., Vol. 26, no. 6, pp.778-783, Nov. 1978

[Case *II*] *The Source is Close to the Scatterer*

[60] D. R. Lynch, K. D. Paulsen and J. W. Strohbehn, *Finite element solution of Maxwell's equations for hyperthermia treatment planning*, J. Comput. Phys., 58, (2), pp. 246-269,1985

[61] D. R. Lynch, K. D. Paulsen and J. W. Strohbehn, *Hybrid element method for unbounded electromagnetic problems in hyperthermia*, Int. J. Num. Meth. Eng., Vol. 23, pp. 1915-1937,1986

[62] K. D. Paulsen, D. R. Lynch and J. W. Strohbehn, *Three-dimensional finite, boundary, and hybrid element solutions of the Maxwell equations for lossy dielectric media*, IEEE Trans. MTT, Vol. 36, no. 4, pp. 682-693, Apr. 1988

[] *Finite element-boundary integral method*

[63] M. A. Morgan, C. H. Chen, S. C. Hill and P. W. Barber, *Finite element-boundary integral formulation for electromagnetic scattering* , Wave Motion, Vol. 6, no. 1, pp.91-103, Jan. 1984

[64] J. A. Stratton, *Electromagnetic Theory*, New York, McGraw-Hill, 1941, Chap. 7

[65] K. K. Mei, *Unimoment method of solving antenna and scattering problems* , IEEE Trans. Antennas Prpoagat., Vol. 22, pp.760-766, 1974

[66] S. K. Chang and K. K. Mei, *Application of the unimoment method to electromagnetic scattering of dielectric cylinders*, IEEE Trans. Antennas Prpoagat., Vol. 24, pp.35-42, Jan. 1976

[67] M. A. Morgan and K. K. Mei, *Finite-element computation of scattering by inhomogeneous penetrable bodies of revolution*, IEEE Trans. Antennas Prpoagat., Vol. 27, pp.202-214, 1979

[] *The FEM combined with the generalized multipole technique*

[68] C. Hafner, *The Generalized Multipole Technique for Computational Electromagnetics*, Artech House, Inc., 685 Canton Street, Norwood, MA 02062, 1990

[69] J. Sroka, H. Baggenstos and R. Ballisti, *On the coupling of the generalized multipole technique with the finite element method*, IEEE Trans. Magnetics , Vol. 26, no. 2, pp. 658-661, Mar. 1990

[*IV*] Hybrid methods combining different formulations into a numerical method

[] *MoM/EFIE-MFIE*

[70] N. C. Albertsen, J. E. Hansen, and N. E. Jensen, *Computation of radiation from wire antennas on conducting bodies*, IEEE Trans. Antennas Prpoagat., Vol. 22, no. 2, pp.200-206, Mar. 1974

[] *MoM/Volume polarization currents*

[71] V. H. Rumsey, *Reaction concept in electromagnetic theory*, Phys. Rev., Vol. 94, pp.1483-1491, June 1954

[72] E. N. Newman and P. Tulyathan, *Wire antennas in the presence of a dielctric/ferrite inhomogeneity*, IEEE Trans. Antennas Propagat., Vol. 26,no. 4, pp.587-592,July 1978

[!] END OF REFERENCES FOR HYBRID METHODS

[73] A. Bossavit, *Simplicial finite elements for scattering problems in electromagnetism*, Computer Methods in Applied Mechanics and Eng., Vol. 76, pp. 299-316, North-Holland, 1989.

[74] J. P. Webb, *Edge elements and what they can do for you*, IEEE Conference on Electromagnetic Field Computation, Harvey Mudd College, Claremont, CA 91711, Aug., 3-5 1992.

[75] M. Koshiba and K. Inoue, *Simple and efficient finite-element analysis of microwave and optical waveguides*, IEEE Trans. MTT, Vol. 40, no. 2, Feb. 1992.

[76] K. S. H. Lee, *EMP Interaction: Principles, Techniques, and Reference Data*, Hemisphere Publishing Corp., 1986.

[77] P. P. Silvester and R. L. Ferrari, *Finite Elements for Electrical Engineers*, Cambridge, U.K.: Cambridge University Press, 1990.

[78] K. D. Paulsen and D. R. Lynch, *Elimination of vector parasities in finite element Maxwell equations*, IEEE Trans. MTT, Vol. 39, no. 3, pp. 395-404, Mar. 1991.

[79] S. D. Gedney and Jin Fa Lee, *A mixed element formulation for the efficient solution of electromagnetic scattering problems*, IEEE Conference on Electromagnetic Field Computation, Harvey Mudd College, Claremont, CA 91711, Aug., 3-5 1992

[80] Henry W. Ott, *Noise Reduction Techniques in Electronic Systems*, 2nd edition, John Wiley and Sons, Inc., 1988.

[81] B.-Q. Gao, and O. P. Gandhi, *An expanding-grid algorithm for the finite-difference time-domain method*, IEEE Trans. EMC, Vol. 34, no. 3, Aug. 1992.

[82] J. H. Yee, et al., *Modeling the interaction of intense electromagnetic pulses with gaseous media*, IEEE Trans. EMC, Vol. 34, no. 3, Aug. 1992.

[S3] J. H. Richmond, *Scattering by a dielectric cylinder of arbitrary cross section shape*, IEEE Trans. Antennas Propagat., Vol. 13, No. 3, pp.334-341, May 1965.

[S4] Robert Lee and A. C. Cangellaris, *A study of discretization error in the finite element approximation of wave solutions* , IEEE Trans. Antennas Propagat., Vol. 40, no. 5, pp. 542-549, May 1992.

[S5] Jin-Fa Lee and Raj Mittra, *A note on the application of edge-elements for modeling three-dimensional inhomogeneously-filled cavities*, IEEE Trans. MTT, Vol. 40, no. 9, pp. 1767-1773, Sept. 1992.

[S6] A. Chatterjee, J. M. Jin, and J. L. Volakis, *Computation of cavity resonances using edge-based finite elements* , IEEE Trans. MTT, Vol. 40, no. 11, pp. 2106-2108, Nov. 1992.

[S7] A. R. Pinchuk, C. W. Crowley, and P. P. Silvester, *Spurious solutions to vector diffusion and wave field problems* , IEEE Trans. Magnetics, Vol. 24, no. 1, pp. 158-161, Jan. 1988.

[S8] I. Bardi, O. Biro, K. Preis, G. Vrisk, and K. R. Richter, *Nodal and edge element analysis of inhomogeneously loaded waveguides* , IEEE Trans. Magnetics, Vol. 29, no. 2, pp. 1466-1469, March 1993.